

AD-A211 426

4

The Pennsylvania State University  
APPLIED RESEARCH LABORATORY  
P. O. Box 30  
State College, PA 16804

AN INVESTIGATION OF END-WALL VORTEX  
CAVITATION IN A HIGH  
REYNOLDS NUMBER AXIAL-FLOW PUMP

by

Kevin J. Farrell

DTIC  
S D  
AUG 07 1989  
D

Technical Report No. TR 89-004  
August 1989

Supported by:  
Naval Sea Systems Command

L. R. Hettche, Director  
Applied Research Laboratory

Approved for public release; distribution unlimited

89 8 07 055

**REPORT DOCUMENTATION PAGE**

1a REPORT SECURITY CLASSIFICATION UNCLASSIFIED		1b. RESTRICTIVE MARKINGS		
2a SECURITY CLASSIFICATION AUTHORITY		3 DISTRIBUTION / AVAILABILITY OF REPORT		
2b DECLASSIFICATION / DOWNGRADING SCHEDULE				
4 PERFORMING ORGANIZATION REPORT NUMBER(S) TR-89-004		5. MONITORING ORGANIZATION REPORT NUMBER(S)		
6a NAME OF PERFORMING ORGANIZATION Applied Research Laboratory	6b OFFICE SYMBOL (if applicable)	7a. NAME OF MONITORING ORGANIZATION		
6c ADDRESS (City, State, and ZIP Code) Post Office Box 30 State College, PA 16804		7b. ADDRESS (City, State, and ZIP Code)		
8a. NAME OF FUNDING / SPONSORING ORGANIZATION Naval Sea Systems Command	8b. OFFICE SYMBOL (if applicable)	9. PROCUREMENT INSTRUMENT IDENTIFICATION NUMBER		
8c ADDRESS (City, State, and ZIP Code) Department of the Navy Washington, DC 20362		10. SOURCE OF FUNDING NUMBERS		
		PROGRAM ELEMENT NO.	PROJECT NO.	TASK NO.
11 TITLE (Include Security Classification) An Investigation of End-Wall Vortex Cavitation in a High Reynolds Number Axial-Flow Pump				
12 PERSONAL AUTHOP(S) Kevin J. Farrell				
13a TYPE OF REPORT	13b TIME COVERED FROM _____ TO _____	14. DATE OF REPORT (Year, Month, Day)	15. PAGE COUNT 165	
16 SUPPLEMENTARY NOTATION				
17 COSATI CODES		18. SUBJECT TERMS (Continue on reverse if necessary and identify by block number)		
FIELD	GROUP			SUB-GROUP
19 ABSTRACT (Continue on reverse if necessary and identify by block number)				
<p>The relative motion of a turbomachinery blade row and the casing requires finite clearance between the rotor tips and the end-wall to avoid rubbing. The presence of this gap, the relative motion of the blade tip and the end-wall, and the pressure difference across the blade give rise to the tip clearance flow. The clearance flow causes many adverse effects, one of which is end-wall vortex cavitation. The vortex is formed by the interaction of the clearance flow with the through-flow on the suction side of the blade. In a liquid medium, the pressure may drop sufficiently to produce cavitation. The end-wall vortex flow field is complex and not well understood.</p>				
20 DISTRIBUTION / AVAILABILITY OF ABSTRACT <input type="checkbox"/> UNCLASSIFIED/UNLIMITED <input type="checkbox"/> SAME AS RPT. <input type="checkbox"/> DTIC USERS		21. ABSTRACT SECURITY CLASSIFICATION		
22a NAME OF RESPONSIBLE INDIVIDUAL		22b. TELEPHONE (Include Area Code)	22c. OFFICE SYMBOL	

In this report a correlation of the appropriate variables which predict the inception of end-wall vortex cavitation is formulated. The approach followed is fourfold: 1) identification of necessary parameters and relationships, 2) experimental measurements of the parameters in the High Reynolds Number Pump facility, a 42-inch diameter pump specifically designed for this purpose, 3) formulation of the correlation model from relationships among the measured variables, and 4) verification of the model with existing databases. The resulting model provides guidance to turbomachinery designers.

The model of end-wall vortex cavitation successfully correlates the subject data and existing databases. An optimum tip clearance has been theoretically identified as experiments have shown. The correlation model contains the boundary layer, lift coefficient, tip clearance, vortex core size, and tip geometry as input variables. Sub-models have been developed for the core radius and tip lift coefficient as a function of tip clearance. Laser velocimeter measurements have shown that additional circulation is shed into the tip vortex from the suction side trailing edge. Recommendations are made to experimentally determine the vortex core size as a function of flow coefficient and tip geometry.

Accession For	
NTIS CRA&I	<input checked="" type="checkbox"/>
DTIC TAB	<input type="checkbox"/>
Unannounced	<input type="checkbox"/>
Justification	
By	
Distribution/	
Availability Codes	
Dist. Statement and/or	
Special	
A-1	



## ABSTRACT

The relative motion of a turbomachinery blade row and the casing requires finite clearance between the rotor tips and the end-wall to avoid rubbing. The presence of this gap, the relative motion of the blade tip and the end-wall, and the pressure difference across the blade give rise to the tip clearance flow. The clearance flow causes many adverse effects, one of which is end-wall vortex cavitation. The vortex is formed by the interaction of the clearance flow with the through-flow on the suction side of the blade. In a liquid medium, the pressure may drop sufficiently to produce cavitation. The end-wall vortex flow field is complex and not well understood.

In this thesis a correlation of the appropriate variables which predict the inception of end-wall vortex cavitation is formulated. The approach followed is fourfold: 1) identification of necessary parameters and relationships, 2) experimental measurements of the parameters in the High Reynolds Number Pump facility, a 42-inch diameter pump specifically designed for this purpose, 3) formulation of the correlation model from relationships among the measured variables, and 4) verification of the model with existing databases. The resulting model provides guidance to turbomachinery designers.

The model of end-wall vortex cavitation successfully correlates the subject data and existing databases. An optimum tip clearance has been theoretically identified as experiments have shown. The correlation model contains the boundary layer, lift coefficient, tip clearance, vortex core size, and tip geometry as input variables.

Sub-models have been developed for the core radius and tip lift coefficient as a function of tip clearance. Laser velocimeter measurements have shown that additional circulation is shed into the tip vortex from the suction side trailing edge. Recommendations are made to experimentally determine the vortex core size as a function of flow coefficient and tip geometry.

## TABLE OF CONTENTS

	<u>Page</u>
LIST OF TABLES .....	vii
LIST OF FIGURES .....	viii
NOMENCLATURE .....	xiii
ACKNOWLEDGMENTS .....	xvi
CHAPTER 1. INTRODUCTION .....	1
1.1 Preliminaries .....	1
1.2 Background .....	2
1.2.1 Rotor Tip Flow Field .....	2
1.2.2 Tip Clearance Cavitation Types .....	8
1.3 Objectives .....	10
CHAPTER 2. PRIOR RESEARCH .....	12
2.1 Overview .....	12
2.2 Tip Clearance Flows in Axial-flow Compressors .....	12
2.3 Tip Clearance Flow Improvements .....	14
2.4 Investigations of Tip Clearance Flows in Compressors ..	16
2.5 Investigations of Tip Clearance and End-wall Vortex Flows in Pumps .....	17
2.6 Current Correlation Model of End-wall Vortex Cavitation .....	33
CHAPTER 3. EXPERIMENTAL FACILITIES AND PROCEDURES .....	35
3.1 Hydrodynamic and Mechanical Design .....	35
3.2 Instrumentation System .....	40
3.2.1 Laser Velocimetry .....	43
3.2.2 Conventional Velocity and Pressure Measurement .....	48
3.2.3 Force and Torque Measurements .....	49
3.2.3.1 Tip Force Measurement .....	49
3.2.3.2 Rotor Blade Force Measurement .....	51
3.2.3.3 Torque Measurement .....	52
3.2.3.4 Calibration of Force and Torque Transducers .....	54
3.2.4 Blade Static Pressure Measurement .....	55

	<u>Page</u>
3.2.5 Dynamic Tip Clearance Measurement .....	58
3.2.6 Cavitation Viewing .....	59
3.2.7 Angular Speed and Position .....	61
3.3 Operating Characteristics .....	61
3.4 Experimental Procedures .....	62
CHAPTER 4. EXPERIMENTAL RESULTS .....	67
4.1 Cavitation Results .....	67
4.1.1 Cavitation Index versus Tip Clearance .....	69
4.1.2 Cavitation Index versus Flow Coefficient and Angular Speed .....	74
4.2 Force Measurements .....	79
4.2.1 Tip Lift Measurements .....	79
4.2.2 Blade Force Measurements .....	83
4.3 Blade Static Pressure Measurements .....	83
4.4 Dynamic Tip Clearance Measurements .....	91
4.5 Velocity Surveys .....	91
4.5.1 Five-hole Boundary Layer Survey .....	91
4.5.2 Laser Velocimeter Surveys .....	95
4.6 Flow Visualization Results .....	113
CHAPTER 5. MODEL DEVELOPMENT .....	124
5.1 Analysis .....	124
5.1.1 Shed Lift Sub-model .....	125
5.1.2 Vortex Core Radius Sub-model .....	128
5.1.3 End-wall Vortex Correlation Model .....	133
5.2 Application of the Model .....	134
5.2.1 Present Data from the High Reynolds Number Pump .....	134
5.2.2 Data from Other Investigations .....	136
CHAPTER 6. CONCLUSIONS .....	150
6.1 Conclusions from the Experimental Program .....	150
6.2 Conclusions from the Correlation Model .....	151
6.3 Recommendations for Further Research .....	152
REFERENCES .....	155
APPENDIX. CAVITATION TEST DATA .....	160

## LIST OF TABLES

<u>Table</u>		<u>Page</u>
4.1.	Five-hole Probe Boundary Layer Survey at $V_X = 31 \text{ ft/s}$ , $Re_c = 1.9 \times 10^6$ .....	93
4.2.	Boundary Layer Integral Properties for Various Laser and Five-hole Probe Surveys .....	101
4.3.	End-wall Vortex Parameters from LV Measurements .....	116

## LIST OF FIGURES

<u>Figure</u>	<u>Page</u>
1.1. Photograph of End-wall Vortex Cavitation in the High Reynolds Number Pump .....	2
1.2. Rotor Tip Flow Field in an Axial-flow Pump .....	4
1.3. Velocity Diagram for a Single Stage Axial-flow Pump a) without Considerations of Tip Clearance or End-wall Effects and b) with Considerations of Tip Clearance and End-wall Effects Included .....	5
1.4. Types of Cavitation in the Tip Region of an Axial-flow Pump Rotor Blade .....	9
2.1. Modified Tip Clearance Model of Lakshminarayana [34] in the Tangential Plane of a Cascade .....	19
2.2. Comparison of Measured Results with the Tip Clearance Model of Lakshminarayana [34], Inoue et al. [41] .....	24
2.3. Comparison of Measured Retained Circulation as a Function of Tip Clearance with the Predictions of Lakshminarayana [34], Inoue et al. [41] .....	25
3.1. Mechanical Drawing of the High Reynolds Number Pump ....	36
3.2. Relationship of the High Reynolds Number Pump to the Garfield Thomas Water Tunnel .....	37
2.3. Photograph of the One-sixth Scale Model of the High Reynolds Number Pump .....	41
3.4. Photograph of the High Reynolds Number Pump in the 48-inch Fixture .....	42
3.5. Instrumentation Block Diagram for the High Reynolds Pump .....	44
3.6. Downstream Cross-sectional View of the Rotor Hub .....	45
3.7. Schematic of Laser Velocimeter System .....	47
3.8. Tip Force Transducer Assembly .....	50
3.9. Blade Force Transducer Assembly .....	53

<u>Figure</u>	<u>Page</u>
3.10. Pressure Transducer Mounting Arrangement in the Rotor Tip .....	57
3.11. Block Diagram of the Dynamic Tip Clearance Measurement System .....	60
4.1. Cavitation Index versus Dimensionless Clearance at Axial Velocities of 26, 31, and 36 ft/s Representing $Re_c$ of $1.6 \times 10^6$ , $1.9 \times 10^6$ , and $2.2 \times 10^6$ for a) Blade Number 2, b) Blade Number 5, and c) Blade Number 6 .....	70
4.2. Cavitation Index versus Flow Coefficient for Dimensionless Tip Clearances of a) 0.08, b) 0.17, c) 0.35, and d) 0.55 .....	75
4.3. Cavitation Index versus Dimensionless Clearance for Flow Coefficient Ranges of 1.26 - 1.28, 1.33 - 1.35, and 1.37 - 1.39 for a) Blade Number 2, b) Blade Number 5, and c) Blade Number 6 .....	77
4.4. Tip Lift Coefficient versus Flow Coefficient for Four Values of Dimensionless Tip Clearance .....	80
4.5. Tip Lift Coefficient versus Dimensionless Tip Clearance for a Flow Coefficient of 1.33 .....	81
4.6. Retained Lift Ratio versus Tip Clearance for Lewis and Yeung [35], Lakshminarayana [34], and the Subject Data ..	82
4.7. Percentage of Tangential Force at Rotor Tip versus Flow Coefficient for Four Values of Dimensionless Tip Clearance .....	84
4.8. Lift Coefficient versus Flow Coefficient .....	85
4.9. Pressure Coefficient, $C_p$ , versus Flow Coefficient for Three Values of Dimensionless Tip Clearance .....	87
4.10. Retained Lift Fraction versus Dimensionless Tip Clearance for both Pressure and Force Measurements .....	89
4.11. Pressure Coefficient, $C_{p_g}$ , versus Flow Coefficient for Four Values of Dimensionless Tip Clearance .....	90
4.12. Tip Clearance versus Axial Velocity as Measured by the Variable Impedance Displacement Transducer and Compared with the Static Micrometer .....	92

<u>Figure</u>	<u>Page</u>
4.13. Incidence Angle versus Tip Clearance for Several Ranges of Flow Coefficient .....	94
4.14. Unwrapped Cylindrical Cross-section of the Rotor Tip ...	96
4.15. Minimum Pressure Coefficient versus Angle of Attack from Douglas Neumann Program .....	97
4.16. Rotor Inlet Boundary Layer Profile at $V_X=26$ ft/s and $Re_C=1.6 \times 10^6$ , Measured with Laser Velocimeter .....	99
4.17. Rotor Inlet Boundary Layer Profile at $V_X=31$ ft/s and $Re_C=1.9 \times 10^6$ , Measured with Laser Velocimeter and Five-hole Probe .....	99
4.18. Rotor Exit Boundary Layer Profile at $V_X=26$ ft/s and $Re_C=1.6 \times 10^6$ , Measured with Laser Velocimeter .....	100
4.19. Rotor Exit Boundary Layer Profile at $V_X=31$ ft/s and $Re_C=1.9 \times 10^6$ , Measured with Laser Velocimeter .....	100
4.20. Velocity Profile for Dimensionless Clearance of 0.54 ...	102
4.21. Energy Profile for Dimensionless Clearance of 0.54 .....	104
4.22. Velocity Profile for Dimensionless Clearance of 0.33 ...	105
4.23. Energy Profile for Dimensionless Clearance of 0.33 .....	106
4.24. Sample Laser Velocimetry Survey of End-wall Vortex .....	108
4.25. Relationship of Global and Vortex Coordinate System ....	112
4.26. Sample Axial and Tangential Velocity Distribution for Tip-wall Vortex .....	114
4.27. Correlation of End-wall Vortex Velocity Distributions ..	115
4.28. Flow Visualization Photograph of Rotor Blade with Dimensionless Clearance of 0.124 .....	118
4.29. Flow Visualization Photograph of Rotor Blade with Dimensionless Clearance of 0.329 .....	119
4.30. Flow Visualization Photograph of Rotor Blade with Dimensionless Clearance of 0.547 .....	120
4.31. Comparison of Rains' [27] Theoretical Tip Lift Coefficient with the Subject Data .....	123

<u>Figure</u>	<u>Page</u>
5.1. Shed Circulation versus Dimensionless Clearance for Subject Data with Sub-model Predictions .....	127
5.2. Leakage Vorticity versus Tip Clearance to Chord Ratio for Inoue et al. [41], Lakshminarayana [34], and Subject Data, ref. Inoue et al. [41] .....	129
5.3. Vortex Core Radius versus Dimensionless Clearance for Subject Data .....	130
5.4. Theoretical Vortex Core Radius versus Dimensionless Clearance for Axial Velocities of 26, 31, and 36 ft/s for Subject Data .....	135
5.5. Theoretical and Measured Cavitation Indices for Three Flow Coefficients at 36 ft/s for the Subject Data .....	137
5.6. Theoretical and Measured Cavitation Indices for Velocities of 26, 31, and 36 ft/s Representing $Re_c$ of $1.6 \times 10^6$ , $1.9 \times 10^6$ , and $2.2 \times 10^6$ Respectively, at a Flow Coefficient of 1.33 for the Subject Data .....	138
5.7. Sub-model Prediction of Vortex Core Radius versus Dimensionless Clearance for Shuba's [1] Data .....	140
5.8. Sub-model Prediction of Shed Circulation versus Dimensionless Clearance for Shuba's [1] Data .....	141
5.9. Theoretical and Measured Cavitation Indices for $V_x/U = 0.877$ , 836 RPM, and $Re_c = 1.1 \times 10^6$ for Shuba's [1] Data .....	142
5.10. Sub-model Prediction of Vortex Core Radius versus Dimensionless Clearance for Rains' [27] Data .....	143
5.11. Sub-model Prediction of Shed Circulation versus Dimensionless Clearance for Rains' [27] Data .....	144
5.12. Theoretical and Measured Cavitation Indices for $V_x/U = 0.45$ , 600 RPM, and $Re_c = 5.8 \times 10^6$ for Rains' [27] Data .....	146
5.13. Sub-model Prediction of Vortex Core Radius versus Dimensionless Clearance for Mitchell's [43] Data .....	147
5.14. Sub-model Prediction of Shed Circulation versus Dimensionless Clearance for Mitchell's [43] Data .....	148

<u>Figure</u>	<u>Page</u>
5.15. Theoretical and Measured Cavitation Indices for $V_x/U = 0.8$ , 750 RPM, and $Re_c = 9.2 \times 10^5$ for Mitchell's [43] Data .....	149
6.1. Cavitation of Interacting Vortices near the Tip Trailing Edge on the Suction Side .....	154

## NOMENCLATURE

A	flow annulus area
b	distance of discontinuity surface from rotor suction side
B	empirical constant
c	blade chord
$C_p$	blade pressure coefficient, $\frac{P_{p50} - P_{s40}}{\frac{1}{2} \rho U^2}$
$C_{p_{min}}$	minimum pressure coefficient, $\frac{P_{min} - P_{ref}}{\frac{1}{2} \rho U^2}$
$C_{p_g}$	tip clearance pressure coefficient, $\frac{P_{tip} - P_{liner}}{\frac{1}{2} \rho U^2}$
$C_{L_o}$	tip lift coefficient at zero clearance condition
$C_{L_{tip}}$	tip lift coefficient, $\frac{L_{tip}}{\frac{1}{2} \rho U^2 A_{tip}}$
D	pump rotor diameter
h	tip clearance
H	shape factor, blade span
k	empirical constant in Equation 4.3
K	retained lift fraction
n	rotational speed (rev/s)
$P_G$	gas pressure
$P_{liner}$	liner surface pressure located axially at the tip mid-chord position
$P_{p50}$	blade surface pressure measured on the tip pressure side at 50% chord position

$P_{s40}$	blade surface pressure measured on the tip suction side at 40% chord position
$P_{tip}$	blade surface pressure measured on the tip surface at 50% chord position
$P_v$	vapor pressure
$P_\infty$	static pressure of desinent cavitation
$r$	radius
$r_c$	vortex core radius
$r_s$	inner radius of pump casing
$Re_c$	Reynolds number based on chord
$S$	blade spacing
$t_m$	maximum tip thickness
$t^*$	time-like parameter
$U$	tip speed
$V_T$	tangential velocity
$V_{REF}$	reference axial velocity
$V_X$	axial velocity
$W_1$	inlet relative velocity at tip
$W_\infty$	mean relative velocity
$x$	passage coordinate
$y$	spanwise coordinate
$\alpha$	air content (ppm)
$\beta$	Henry's law constant
$\Gamma_{sec}$	circulation in end-wall vortex from suction side trailing edge flow and other secondary sources
$\Gamma_{tv}$	total circulation in end-wall vortex

$\Gamma^*$	dimensionless circulation, $\Gamma^* = \lambda \epsilon \left( \frac{4 + C_{L_{tip}}}{C_{L_{tip}}} \right)^{\frac{1}{2}} t^{*0.72}$
$\delta$	boundary layer thickness
$\delta^*$	displacement thickness
$\epsilon$	maximum thickness over chord at tip, $\frac{t_m}{c}$
$\theta$	momentum thickness
$\lambda$	tip clearance over maximum tip thickness, $\frac{h}{t_m}$
$\xi$	coordinate along vortex sheet
$\rho$	fluid density
$\sigma$	desinent cavitation index, $\frac{P_\infty - P_v}{\frac{1}{2} \rho U^2}$
$\sigma_{V_x}$	desinent cavitation index, $\frac{P_\infty - P_v}{\frac{1}{2} \rho V_x^2}$
$\sigma_{W_\infty}$	cavitation index at inception, $\frac{P_i - P_v}{\frac{1}{2} \rho W_\infty^2}$
$\phi$	flow coefficient, $\frac{V_x A}{nD^3}$
$\omega$	angular speed of vortex core

## ACKNOWLEDGMENTS

I wish to express my appreciation to Dr. Michael L. Billet, Senior Scientist at the Garfield Thomas Water Tunnel of the Applied Research Laboratory, for his assistance throughout this investigation. Also, I would like to thank Mark W. McBride, Research Associate and David R. Stinebring, Research Assistant at the Water Tunnel, for their assistance during this investigation. Finally, the entire staff of the Garfield Thomas Water Tunnel is worthy of many thanks for their assistance in a project of this magnitude.

This investigation was conducted in the Garfield Thomas Water Tunnel of the Applied Research Laboratory at The Pennsylvania State University under the sponsorship of the United States Navy Department.

## Chapter 1

### INTRODUCTION

#### 1.1 Preliminaries

The relative motion of a turbomachinery rotor and the stationary casing requires a finite clearance between the rotor tips and the end-wall to avoid rubbing. The presence of this gap, the relative motion of the rotor tip and the end-wall, and the pressure difference across the rotor blade give rise to the tip clearance flow. Flow energy losses occur because the clearance flow does not receive a momentum increase from the rotor. Thus the efficiency of the rotor is reduced. In addition, as much as 20 percent of the blade span may have a three-dimensional flow field due to this clearance flow.

The presence of tip clearance flow in liquid handling machinery is a source of cavitation. In a liquid medium, the pressure may drop sufficiently low to produce localized boiling, called cavitation. Cavitation in the clearance region can result in material damage to the casing and rotor. Small streams of vapor bubbles appear within the liquid at these low pressure locations. When the bubbles enter regions of higher pressure, they collapse and create a localized pressure wave of the order of 400 MPa. The repeated action of collapsing bubbles leads to cavitation erosion. Therefore, it is imperative that this phenomenon be studied and minimized.

Several types of cavitation occur in or near the clearance region. The emphasis of this study is end-wall vortex cavitation. The vortex is formed by the interaction of the clearance flow with the through-flow. A photograph of a cavitating end-wall vortex from the High Reynolds Number Pump is given in Figure 1.1. The cavitation is



Figure 1.1. Photograph of End-wall Vortex Cavitation in the High Reynolds Number Pump

influenced by the presence of the pump casing since the rotor tips rotate through the boundary layer which is formed on the casing. In addition, the end-wall retains a portion of the circulation on the blade tip which would normally be shed into the trailing vortex.

## 1.2 Background

### 1.2.1 Rotor Tip Flow Field

Turbomachinery rotors have very complex flow fields due to the interaction of many phenomena. The flow field is illustrated in Figure 1.2. Both flow and geometrical parameters influence the flow field: variable airfoil cross-section, blade stagger angle and lean, inlet swirl, blade rotation, and boundary layers on the end-wall, hub-wall, and blade both in the axial and radial direction. It is obvious that no complete analytical solution of the velocity or pressure field exists. The presence of a finite clearance in the tip region increases the complexity of the situation.

The effects of the tip clearance flow and the end-wall boundary layer on the rotor-tip flow field are readily seen by examining the velocity diagram for a single stage axial-flow pump. The specific stage shown in Figure 1.3a is designed without considering the effect of the end-wall boundary layer and the tip clearance flow. It is also designed so that the flow leaving the rotor has no tangential component of velocity. However, in considering the tip region, the clearance from the pressure to the suction surface adds a component to the relative velocity which is normal to the chord. Thus the fluid is

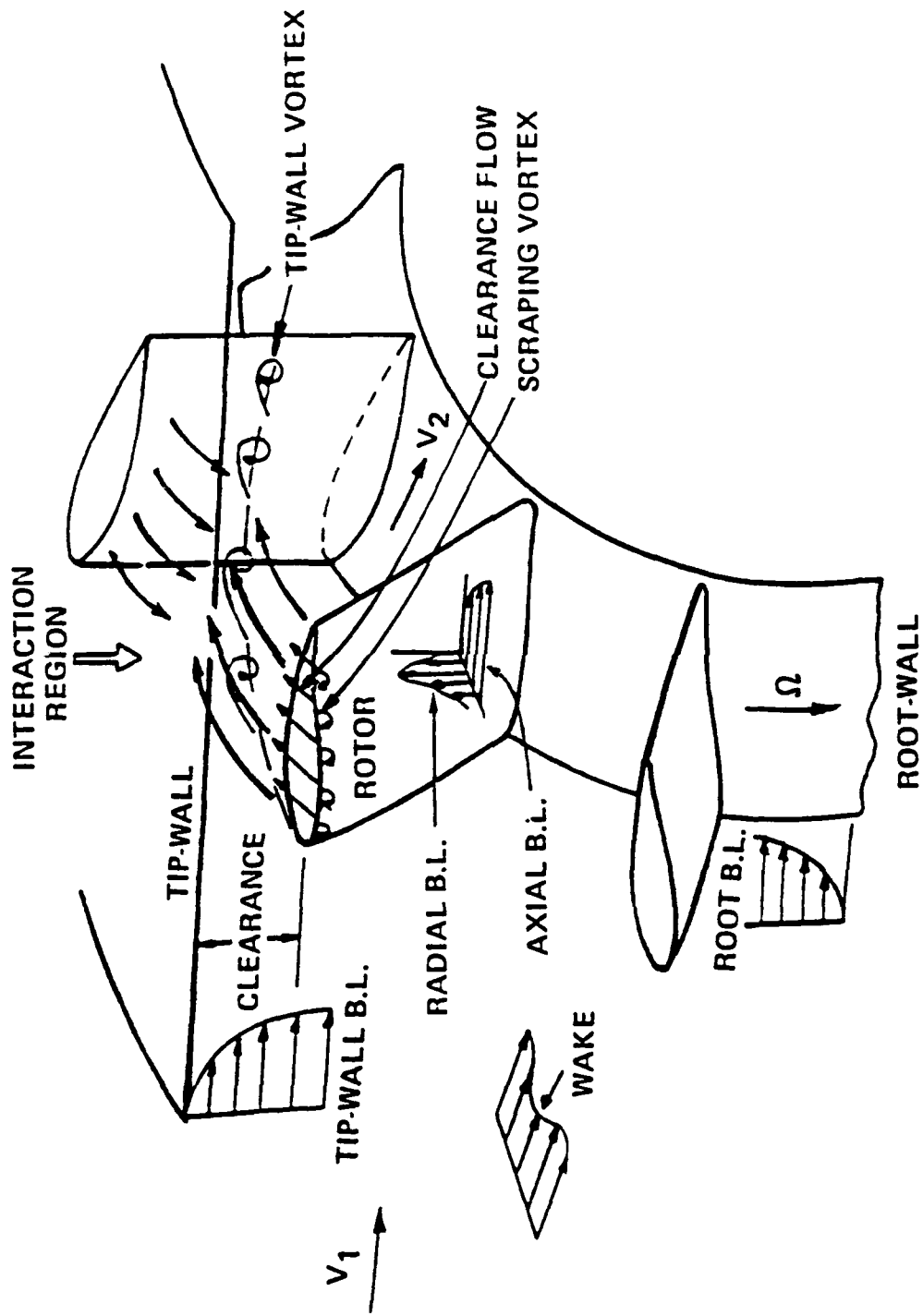


Figure 1.2. Rotor Tip Flow Field in an Axial-flow Pump

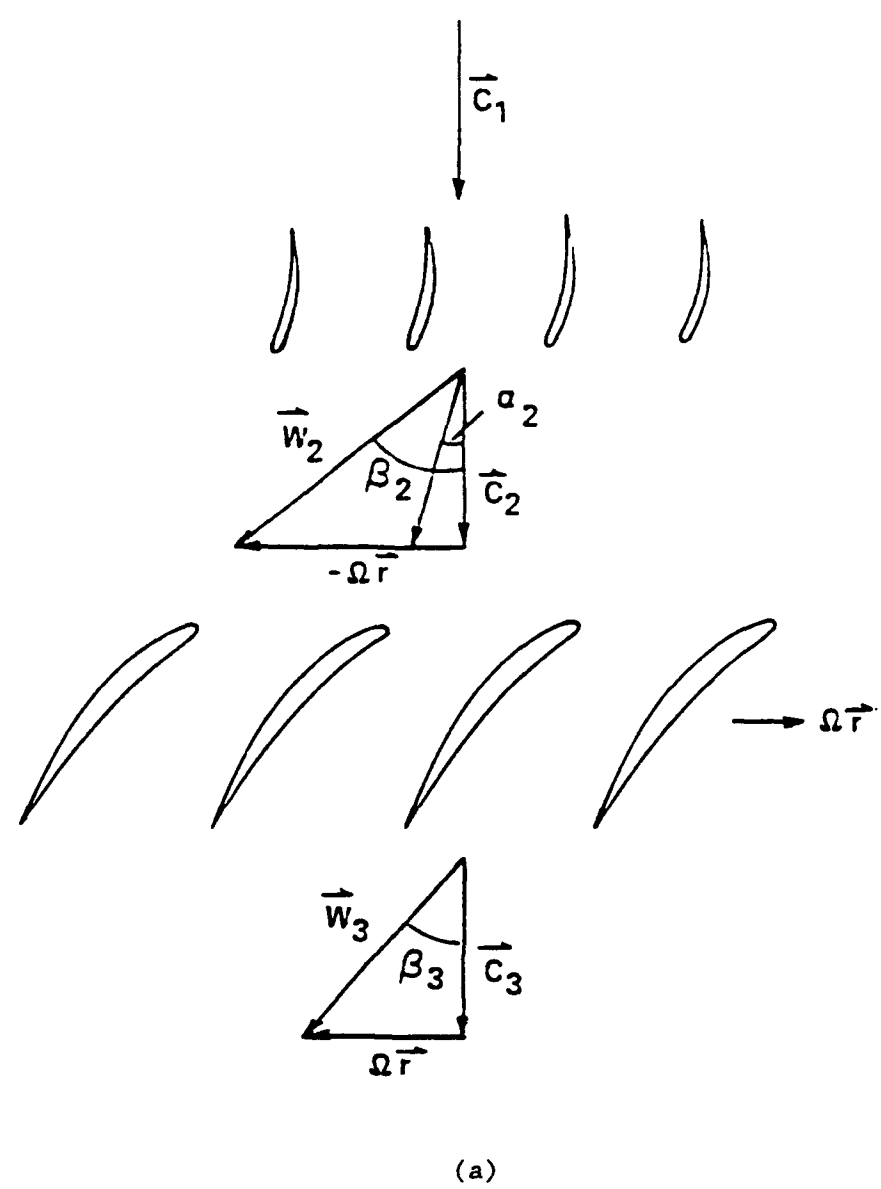
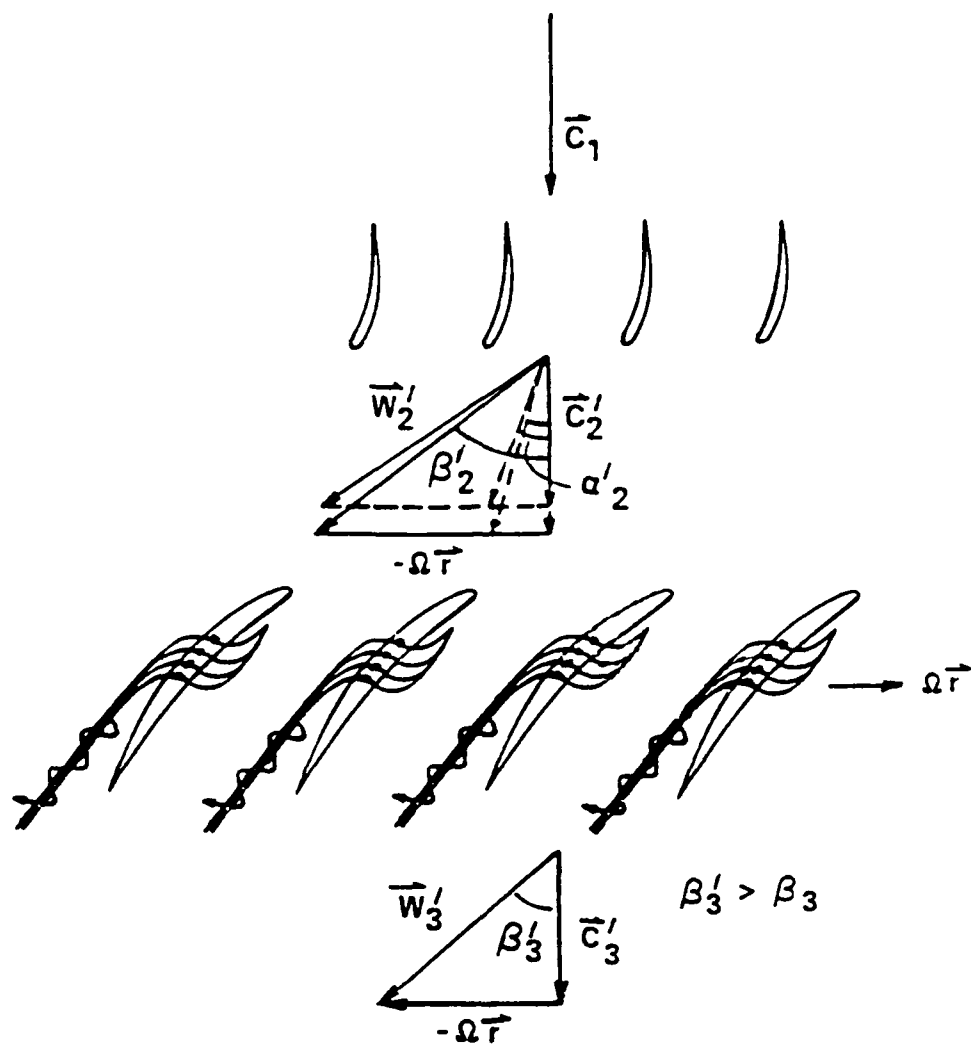


Figure 1.3. Velocity Diagram for a Single Stage Axial-flow Pump  
a) without Considerations of Tip Clearance or End-wall Effects and b) with Considerations of Tip Clearance and End-wall Effects Included

(cont. on next page)



(b)

Figure 1.3 (cont.)

underturned in this region, and the axial velocity decreases in the tip region as shown in Figure 1.3b. For normal tip clearances in axial-flow turbomachines, the rotor tip operates in the boundary layer of the end-wall. The effect of the boundary layer is a reduction in the localized axial velocity and an increase in the incidence angle. The incidence angle also increases because of the clearance flow through the gap which would ordinarily pass on the pressure side of the rotor blade. Furthermore, the pressure difference across the blade increases as a result of the larger incidence angle. Hence the clearance flow velocity is increased.

The clearance flow intersects the flow over the suction side of the blade which has a different magnitude and direction. The two flows form a liquid jet having vorticity which eventually rolls up to form a vortex. Recalling Helmholtz' vorticity theorems, the leakage vortex can be seen to equal the sum of the vortices generated by the rotor and shed at the tip, the secondary vorticity generated by the flow turning through the clearance, and the "scraping" vorticity from the scraping of the end-wall boundary layer on the pressure side of the rotor. Usually the clearance is large enough and the turning small enough so as not to generate strong secondary vorticity. In fact, the secondary vorticity was found to be an order of magnitude less than the shed vorticity in the pump used by Shuba [1]. It follows that the leakage vorticity and the shed vorticity are of the same order of magnitude.

The vorticity shed at the tip is affected by flow parameters and geometrical properties of the blade cross-section. The Reynolds

number associated with the flow through the rotor is based on the relative velocity. Traditionally vortex cavitation has been scaled with Reynolds number, but actually cavitation is correlated with both bubble dynamic effects and viscous effects; consequently, the traditional Reynolds number correlation alone is inadequate. From the velocity triangle in Figure 1.3b, one can conclude that the vorticity shed in to the tip region is a function of rotational speed, axial velocity, and inlet swirl. The size of the clearance obviously limits the mass flow through the gap and thus influences the strength of the end-wall vortex. The end-wall affects the loading at the tip of the rotor because the boundary layer formed on this surface is usually thicker than the clearance. A shear flow exists in the clearance because of the boundary layers on both the end-wall and the rotor tip. The thickness of the airfoil at the tip is a length scale for the development of the Couette flow in the clearance. The geometry of the airfoil directly affects the pressure distribution across the blade and hence the lift. The pressure distribution determines the location of the minimum pressure and influences where cavitation will occur.

### 1.2.2 Tip Clearance Cavitation Types

Cavitation occurring in the tip clearance flow region, has been classified into three types: gap, blade-end, and end-wall vortex cavitation. The three types of cavitation are illustrated in Figure 1.4 on an axial-flow pump rotor blade. Gap cavitation occurs in the clearance itself usually near the blade section minimum pressure. It is usually prevented by rounding the intersection of the

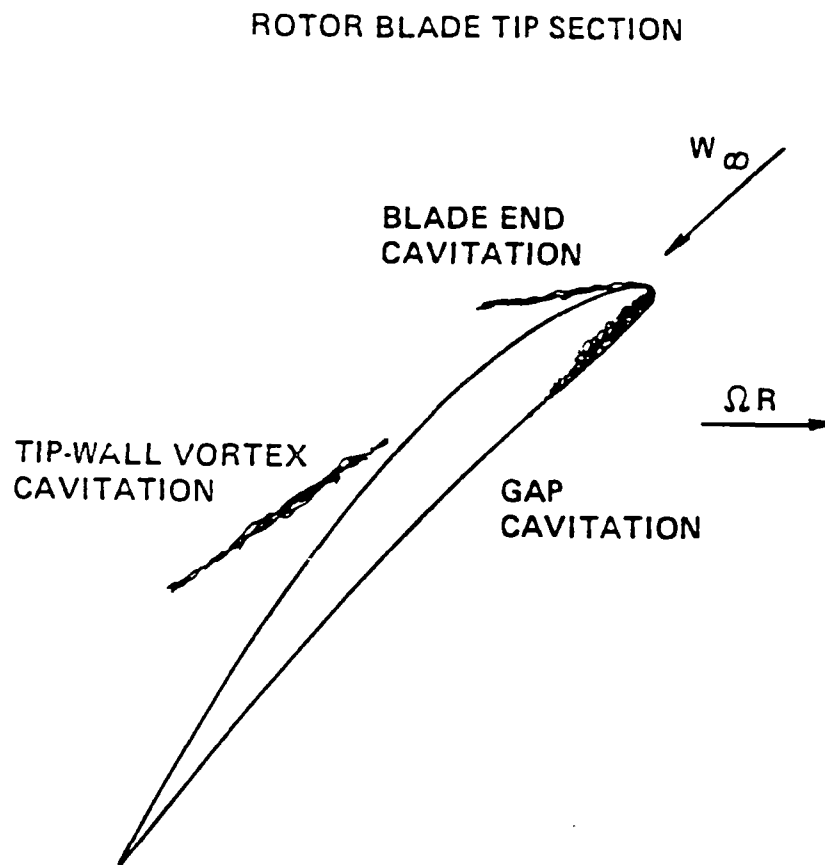


Figure 1.4. Types of Cavitation in the Tip Region of an Axial-flow Pump Rotor Blade

leading edge and pressure surface with the tip surface [2]. Blade-end cavitation occurs at the leading edge when clearances are small and results from a vortex formed by the stretching of boundary layer vorticity. The geometrical modifications which prevent gap cavitation usually prevent blade-end cavitation also. The idea is to simply provide a smooth path for the fluid around the blade tip. End-wall vortex cavitation, as mentioned above, results from the vortex formed by the interaction of the leakage flow with the through-flow. The position of the vortex along the chord varies depending upon the blade incidence angle. Of the three types, the end-wall vortex is the most complex and the least understood.

### 1.3 Objectives

Since methods to reduce end-wall vortex cavitation are desirable, it is essential that one understand the physics of this turbomachinery flow field. The objective of this research work is to construct and evaluate a correlation of the appropriate variables which predict the inception of end-wall vortex cavitation. The approach was as follows: 1) first, research prior investigations and identify necessary parameters and relationships, 2) second, experimentally measure the important parameters in a high Reynolds number axial-flow pump facility, 3) determine the relationship among the variables and formulate a correlation model, and 4) verify the model with existing databases.

Many of the flow and geometrical parameters were identified from past investigations documented in the literature. Several incomplete

models and sub-models served as building blocks for the present work. A limited database exists for low Reynolds numbers ( $6 \times 10^5$ ) for verification purposes. The experimental work of the present investigation has provided high Reynolds number ( $3 \times 10^6$ ) data.

Based on the literature survey, an extensive experimental program was developed. In view of the measurement requirements, a large axial-flow pump was designed, constructed, and tested in the Garfield Thomas Water Tunnel to accommodate these measurements in the rotor tip flow field. The tests consisted of cavitation observations, laser velocimetry, force measurements, five-hole probe velocity surveys, rotor blade and liner surface pressure measurements, and dynamic tip clearance measurements. Measured data were compared to existing data and theories. The resulting model of end-wall vortex cavitation is intended to be used for design guidance.

## Chapter 2

### PRIOR RESEARCH

#### 2.1 Overview

Most of the research regarding end-wall/clearance flow phenomena has been concerned with their influence on turbomachinery efficiency and stall margin. In this regard, the resulting research was aimed at obtaining various performance derivatives with respect to tip clearance. The physics of the end-wall vortex were not addressed directly. However, most of the research in this area is useful to understand the detrimental effects of tip clearance loss and to identify important variables. The literature reviewed herein was examined in search of correlation models and sub-models for these variables. Several other reviews of tip clearance literature in general have been published; see for example Reeder [3] and Peacock [4]. The focus of this chapter is to document the present knowledge on the end-wall vortex phenomenon and its subsequent cavitation.

#### 2.2 Tip Clearance Flows in Axial-flow Compressors

The tip clearance flow across the airfoil tip with its interaction with the end-wall boundary layer and secondary flows produces substantial losses in efficiency and stall margin. Recent compressor designs have higher pressure rise per stage, higher aerodynamic loadings, higher speeds, and lower aspect ratios than previous designs. Leakage flows occur not only in the tip clearance but also around the rotor dovetail and around the stator/hub interface. Tip clearance effects are influenced by the magnitude of the tip clearance, airfoil

loading, aspect ratio, solidity, stagger, vector diagrams, wall relative speed, boundary layer size, and presence of secondary flows.

In an experiment by Wisler [5], the peak efficiency dropped 1.5 points, the stalling flow coefficient increased 11 percent, and the peak pressure declined 9.7 percent when the tip clearance was increased from 1.4 to 2.8 percent of the blade span. Wisler also showed that increasing the tip clearance increased loss as evidenced in circumferential total pressure profiles and increased the size of the tip clearance vortex. The punitive effects of tip clearance flow are further discussed at length in AGARD Conference Proceedings No. 237 [6] and by Koch [7]. Turbomachinery designers often refer to the clearance derivative which is the ratio of the change in efficiency divided by the change in normalized clearance. Efficiency derivatives usually range from 1.2 to 2.0 depending on the particular design.

Increases in tip clearance can produce significant changes in the end-wall boundary layer. The end-wall loss is measured by two properties: the boundary layer displacement thickness and the tangential force thickness. The tangential force thickness represents the amount that the tangential component of blade force is reduced from its freestream value by the presence of the end-wall boundary layer. Koch and Smith [8] showed that the stage efficiency of a high-radius-ratio, multi-stage compressor can be expressed in terms of the momentum and tangential force thicknesses, which in turn are functions of the tip clearance as well as other variables. Hunter and Cumpsty [9] found in their large scale, low speed axial compressor that the downstream

boundary layer was found to thicken as the rotor loading and tip clearance were increased. This effect reduced compressor performance.

### 2.3 Tip Clearance Flow Improvements

The compressor industry has responded to the tip clearance problem with several engineering solutions. One popular method used to improve compressor stall margin is casing or hub treatment. A trenching process is also performed on the casing to improve efficiency. Moreover, various tip treatments are used to reduce tip clearance leakage. As an alternative to the above geometrical modifications, active and passive clearance control systems are employed to change the size of the tip clearance.

Various geometries of casing or hub treatments have been investigated with varying success. The spacing, size, and direction of the grooves or slots have been altered to find the optimum design. The effect on stall margin is positive; however, the treatment with the most stall margin increase suffered the most efficiency loss. According to Wisler [5], the most successful casing treatments have 65 to 75 percent open area, and most of the benefits come from treating the center 60 percent of the chord projection. The effectiveness of casing/hub treatment is a subject of many researchers: Bailey and Volt [10], Osborne et al. [11], Moore et al. [12], Bailey [13], Boyce et al. [14], Prince et al. [15], Fabri and Reboux [16], Takata and Tsukuda [17], and Hunter and Cumpsty [9].

Trenching consists of cutting a trench into the casing and then extending the rotor tip to allow the tip clearance to be buried in the

trench. Trenching is used primarily to improve efficiency. A combination of trenching and casing treatment gave a return in efficiency approaching the baseline while increasing the stall margin in the cases cited by Robideau and Nuler [18] and Roberts [19].

Tip treatment is defined as a modification or treatment to the airfoil tip in order to reduce the effects of tip clearance leakage. Several treatments investigated include the squealer tip, the deep groove treatment, and various winglet configurations. Notwithstanding the differences between compressor and turbine flow fields, the deep-groove treatment and pressure-surface winglet reduced the leakage by about 15 percent as reported by Booth et al. [20]. Additional numerical and experimental contributions to this subject have been made by Wadia and Booth [21], and Wadia [22].

Another solution to the tip clearance problem is passive or active clearance control. The tip clearance problem is compounded by the transient thermal response of the casing and rotor, centrifugal loading of the rotor, and from various loads encountered through surge/stall, maneuvering, gusts, and landing. Passive control is achieved by altering the thermal response of the casing or rotor through added mass or secondary air flows. Investigations by Owen [23] and Hennicke [24,25] have shown that a small amount of vent air through the disk cavities and hub can strongly affect the temperature response of the rotor. If close tolerances are to be maintained during flight, bleed air is used to control rotor and casing temperatures as a means of active clearance control.

#### 2.4 Investigations of Tip Clearance Flow in Compressors

Wu and Wu [26] performed a theoretical analysis of the blade tip flow using a rotating, relative, cylindrical coordinate system moving with the blade at the same speed. Order of magnitude analyses were performed for both high and low Reynolds number flows in order to derive the equations of motion. The velocity field across the clearance was generated by simply integrating the resulting governing equation and applying the boundary conditions. The pressure distribution across the clearance was calculated by solving Laplace's equation after the Joukowski transformation was applied to the airfoil. Wu and Wu concluded that the velocities through the clearance vary with the square of the tip clearance and that the mass flow across the tip clearance varies with the cube of the tip clearance. This differs significantly with the theory of Rains [27] and Vavra [28].

Dean [29,30] used a cascade to study the influence of tip clearance on boundary layer flow. Combining measurements with theory, Dean described and modeled the tip leakage flow and secondary flow in the wall boundary layer. Dean stated that rotation increases the lift on the blade tip. This change in lift directly affects the circulation of the end-wall vortex.

Jefferson and Turner [31] studied tip clearance effects in an actual, multi-stage axial compressor. The work dealt chiefly with shroud leakage clearances, although the radial tip clearance was also investigated. Contrary to Wisler [5], Jefferson and Turner claimed that a moderate value of tip clearance improved the stalling characteristics.

## 2.5 Investigations of Tip Clearance and End-wall Vortex Flows

Lakshminarayana and Horlock [32,33] used a modified lifting line approach to model the tip clearance flow. In the model it is assumed that the lift is uniform all along the span and only a part of the bound vortex is shed off. Lakshminarayana [34] acknowledged the deficiencies of these earlier models and developed an alternative model which takes into account the presence of the vortex core. This model predicts blade-to-blade variation in outlet angles and total pressure losses.

In the derivation of the total pressure loss using his earlier model, Lakshminarayana [34] noted the dependence of the tip lift upon tip clearance. The presence of the wall retains a portion of the lift while the remaining circulation is shed. The values of the retained lift fraction,  $K$ , were determined from blade pressure measurements at the tip in the absence of secondary flow. The following relationship was given for the variation of  $K$  with the clearance to blade spacing ratio:

$$(1 - K) = 0.23 + 7.45 \frac{h}{S} \quad 0.01 < \frac{h}{S} < 0.1 \quad . \quad (2.1)$$

Lakshminarayana [34] criticized the assumptions of Rains [27] and Vavra [28] that 1) the leakage flow occurs in an annulus of height equal to the clearance height and 2) the leakage flow perpendicular to the chord rolls up into a vortex whose energy is unrecoverable. He stated that these models omitted solidity and spanwise effects. Lakshminarayana included the spanwise flow analytically in a semi-empirical development of an efficiency degradation - tip clearance

relation. The relation compared reasonably well with some experimental results; however, the agreement with Rains' data was poor.

Lakshminarayana acknowledged the presence of other parameters in the tip region: blade thickness at the tip, Reynolds number effects, and wall boundary layer thickness.

A more detailed model of the tip clearance flow was required because the previous models were satisfactory for efficiency calculations only and did not predict the presence of a loss core or the outlet angle distribution. The new model considered the effect of solid body rotation in the viscous core of the leakage vortex. The modified clearance model is shown in Figure 2.1 in the tangential plane of a cascade. The core region behaves as a solid body rotation, and the outer region behaves as a free vortex. The boundary condition of zero normal velocity at the wall is satisfied by the image vortices. Lakshminarayana [34] used Rains' equations to calculate the core size and angular speed. This distance  $b$  at which the vortices are located at any axial location can be calculated by knowing the flow field and the point of the vortex origin. Lakshminarayana solved for the induced flow field and the fluid outlet angles due to two infinite rows of vortices. Downstream of the rotor trailing edge, Lakshminarayana applied laminar flow theory to the viscous vortex to calculate defects in longitudinal velocity and stagnation pressure which occur as the forced core increases and the vorticity diffuses outward.

Lakshminarayana compared the prediction of this theory with cascade data. The predictions of outlet angles were good. Near the tip, the leakage flow produces underturning while the secondary flow

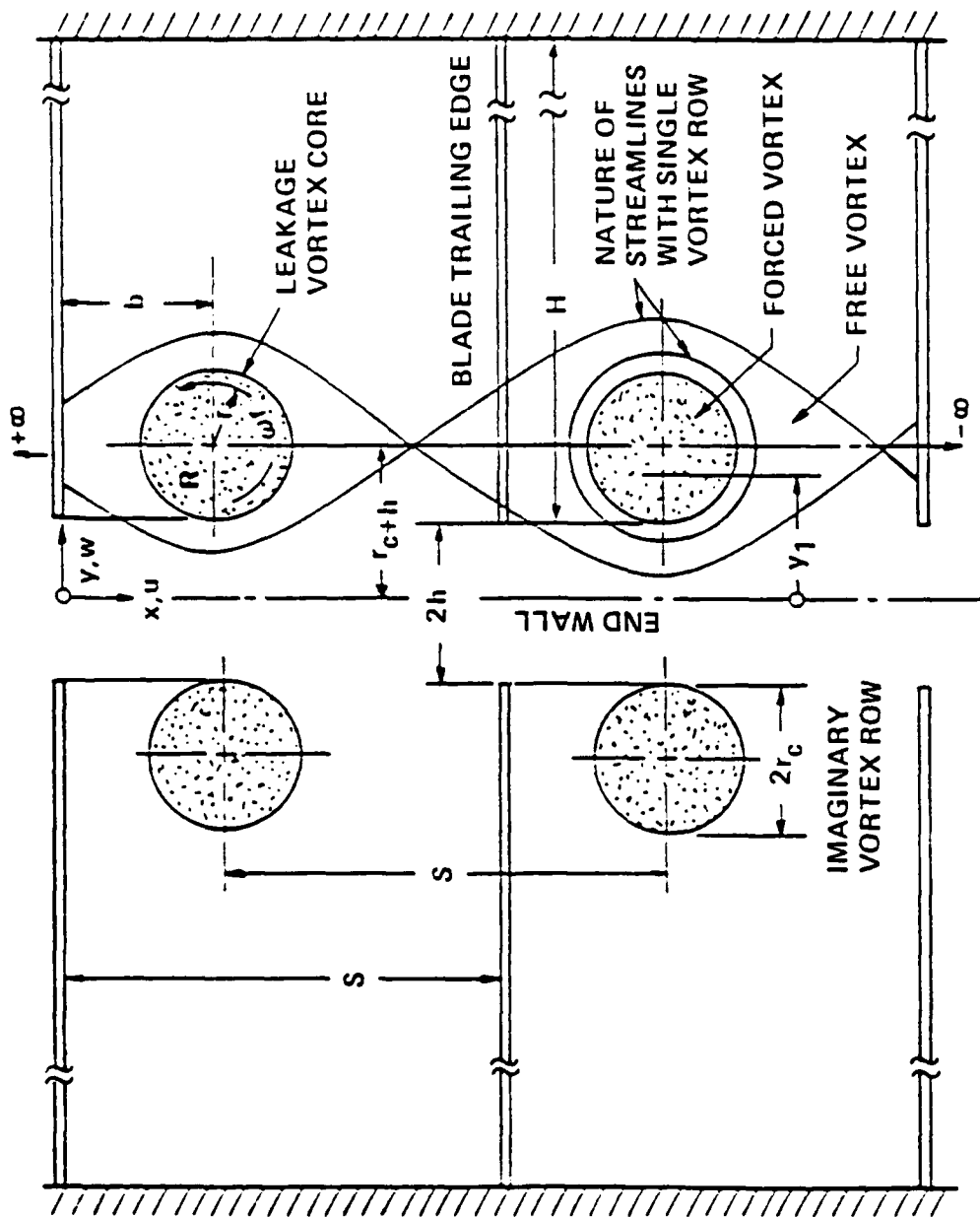


Figure 2.1. Modified Tip Clearance Model of Lakshminarayana [34] in the Tangential Plane of a Cascade

produces overturning. Lakshminarayana noted that the interaction is beneficial since maximum underturning and overturning angles are reduced. He also stated that for practical purposes, it was sufficient to include only the leakage effect in calculating outlet angles. Furthermore, the discrepancy between the theory and the experimental results was attributed to the "moving wall" effect. Comparisons of measured and calculated stagnation pressure deficiencies were not very good; the only conclusion made was that the maximum loss region is located inboard from the blade tip.

Lakshminarayana provided an argument for the existence of an optimum clearance. He stated that, since the leakage and secondary vorticities are located in the same region and are opposing in nature, the criterion for optimum clearance would be a net circulation of zero. The effect of rotation produces a scraping vortex which also must be included with the other vortices. This theory is substantiated by smaller optimum clearances for rotating blades than for a cascade. The optimum clearance, however, may not result from the zero sum of the individual circulations. The individual values of the circulation may be large, and thus in the case of the clearance circulation, form an end-wall vortex of considerable strength.

Lewis and Yeung [35] outlined the importance of tip clearance flows in axial fans as a source of loss and derived an expression for the dimensionless loss through the application of Rains' [27] jet loss theory. Several vortex shedding models were also presented for a single airfoil in a freestream. Theoretical predictions from these models were compared to Lakshminarayana and Horlock [32]. Calculations

by the investigators showed that the concentrated tip vortex method is the superior method for airfoils of varying aspect ratio and as a prediction method for overall lift coefficient. Experimental work by the investigations showed that there is a reduction in lift at the tip compared with the value of lift coefficient with no gap. Lewis and Yeung found the following empirical correlation which predicts values of the retained lift ratio,  $K$ , as a function of tip clearance:

$$K = \exp (-14 h/c). \quad (2.2)$$

They also stated that the tip clearance loss is likely to be smaller than that given by the tip leakage jet theory. The shedding of circulation along the blade span contributes another portion of the loss. They also theorized that for small clearances the total loss can be approximated by that given by jet theory, but for larger clearances the vortex development and the induced velocities must be included.

Lakshminarayana, Pouagare, and Davino [36] measured the flow field in the end-wall and tip region of a compressor rotor. The measurements showed that the leakage flow starts after the quarter-chord point and tends to roll up farther away from the suction surface than that observed in cascades. Lakshminarayana et al. also noted that within approximately 10 percent of the blade span at the tip, a region of intense viscous and leakage flow interaction and mixing occurs at 65 percent of the tangential distance from the suction side to the pressure side of the blade passage. The normalized streamwise velocity deficiency was attributed to low momentum fluid and inward radial flows from this mixing and reaches a maximum value of 0.6 of the mean relative velocity. Also within 10 percent of the blade span from the

tip, the normal velocity indicated both underturning of the flow due to the combined effect of the tip leakage flow and wall boundary layer and overturning due to the rolling up of the tip leakage flow by the mainstream flow. Furthermore, the end-wall boundary layer profile undergoes substantial changes as it passes from the leading edge to the trailing edge. A complex profile results from the energizing of the boundary layer by the leakage flow. Finally, large radial, inward velocities were observed near the outer 8 percent of the span.

In a companion paper by Lakshminarayana et al. [37], the turbulence properties of the compressor rotor tip region were investigated. A growing core of high turbulence was located near 65 percent of the blade passage distance from the suction side, corresponding to the interaction region mentioned earlier. The maximum intensities measured at the tip in the mid-chord region were 32, 27.5, and 15 percent for the radial, normal, and streamwise components, respectively. Pandya and Lakshminarayana [38,39] extended the measurement efforts of Lakshminarayana, Pouagare, and Davino at axial positions downstream of the rotor. They found that at three-quarter chord downstream, the rotor exit flow was essentially uniform.

Lakshminarayana, Sitaram, and Zhang [40] completed detailed measurements of relative stagnation pressure losses inside the rotor of a low-speed axial-flow compressor. Tip losses were found to increase with an increase in pressure rise. Furthermore, they verified the location of the tip region loss core near mid-passage and that the spanwise extent of the core increases from leading to trailing edge. Finally, the tip leakage loss seemed to dominate the end-wall region

with the secondary flow and end-wall boundary layer losses significantly smaller.

Inoue, Kuroumaru, and Fukuhara [41] made detailed flow measurements with various tip clearances and compared their results to the flow model of Lakshminarayana [34]. The reduction in efficiency did not agree with existing predictions in this experiment. Inoue et al. found that, at the same incidence, the relative exit flow angle and total pressure loss changed little with tip clearance except in the casing boundary layer. The exit axial velocity was found to increase due to the blocking effect of the annulus-wall boundary layer. The leakage vortex was found to roll up more intensely with increasing clearance and at a location more distant from the suction side of the blade. The large vortex motion caused reverse flow near the casing wall. The comparison of the vortex with Lakshminarayana's model showed only qualitative agreement. Finally, the amount of circulation in the leakage vortex was substantially larger than that predicted by Lakshminarayana for moderate-to-large tip clearances. The comparison of the results of Inoue et al. with the predictions of Lakshminarayana is shown in Figures 2.2 and 2.3.

Lakshminarayana and Murthy [42] performed detailed laser velocimeter measurements in the tip region of a compressor rotor and confirmed details of the flow field, although they offered no new observations. The eventual roll-up of the end-wall vortex resulted in higher and lower relative tangential velocity components at higher and lower radii, respectively. Also, the end-wall vortex originated at a quarter chord and extended toward the pressure surface to form an

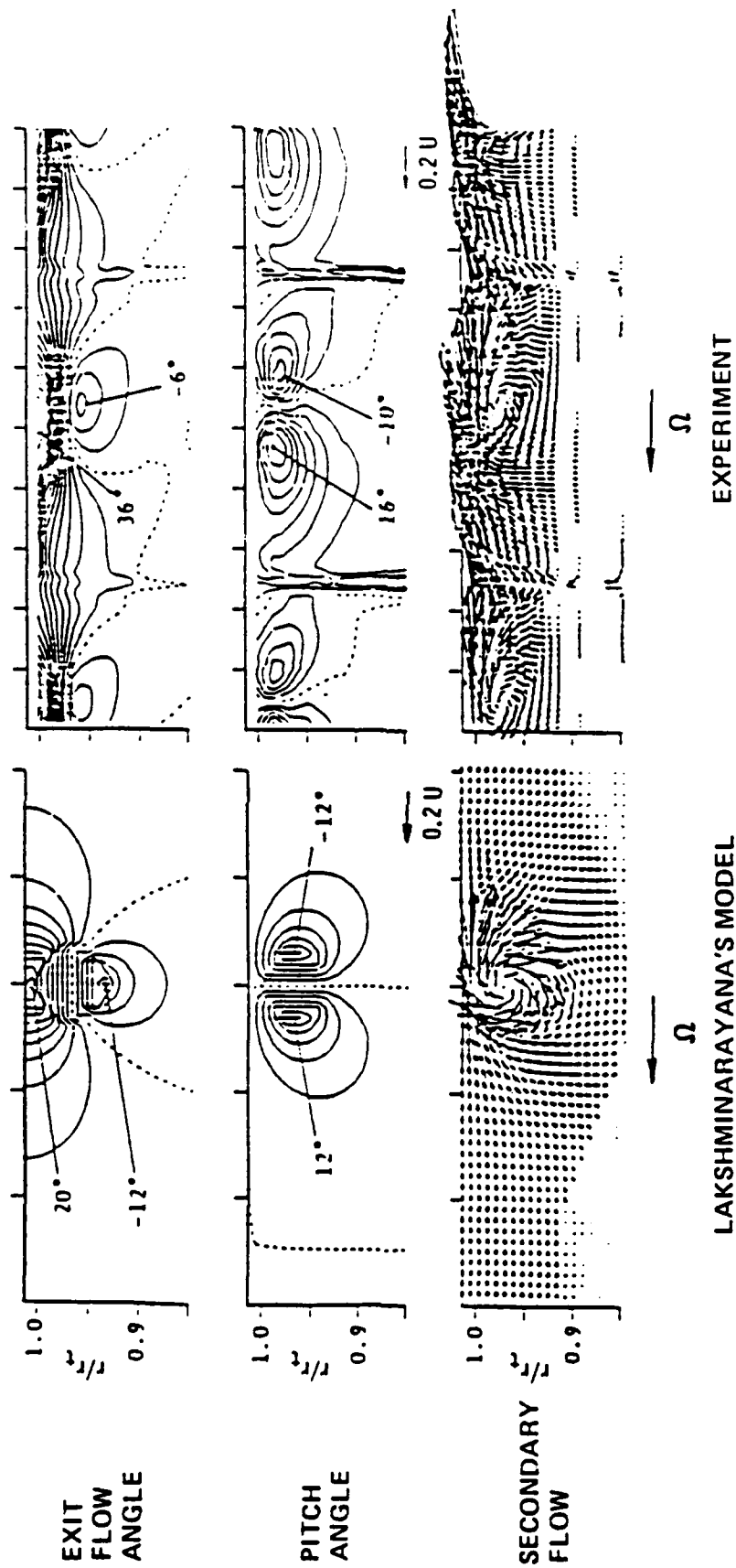


Figure 2.2. Comparison of Measured Results with the Tip Clearance Model of Lakshminarayana [34], Inoue et al. [41]

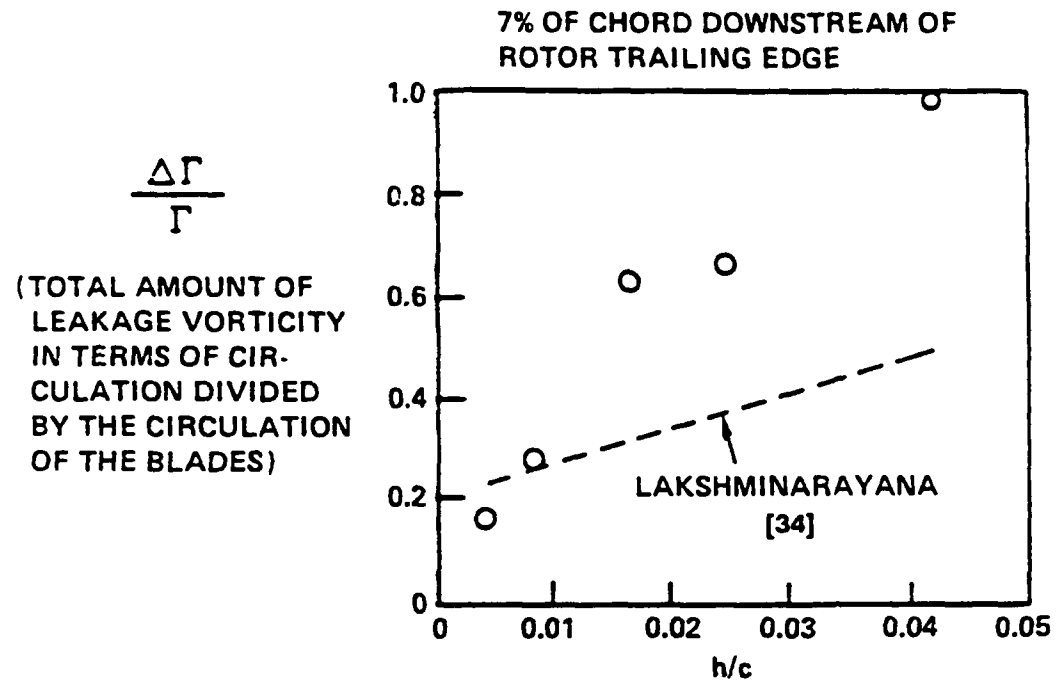


Figure 2.3. Comparison of Measured Retained Circulation as a Function of Tip Clearance with the Predictions of Lakshminarayana [34], Inoue et al. [41]

interaction region that was nearly 12 percent of the blade span at the tip. The diffusion of the end-wall vortex was augmented by blade rotation as it convected downstream.

Most of the literature dealing with the tip clearance flow is associated with the aircraft industry. The results of the compressor tip clearance work can be applied, to varying degrees, to axial-flow pumps. It should be emphasized that the end-wall vortex associated with a pump is largely different from the tip or trailing vortex originating from the tip of a wing or propeller. The wall retains a fraction of the lift in a pump, whereas the wing sheds all the lift at the tip. However, several significant studies of pumps have been completed, and most are largely experimental in nature. Some of the studies have included investigations into the cavitation phenomena of the tip clearance flow.

Rains [27] conducted the first systematic investigation of tip clearance flows with cavitation studies in an axial-flow pump. Rains was mainly concerned with developing models for the end-wall vortex, but experimental work was also completed. Rains' main purpose in deriving the model was to devise a way in which clearance losses could be calculated in a systematic manner. Cavitation was used as a tool to study the size and strength of the end-wall vortex.

Rains' preliminary model of the tip clearance flow was a perfect fluid model. A wing with a slot was chosen as the best model from the flow visualization results. The Kutta condition was satisfied along the edges of the slot. A stiff jet issues from slot on the suction side and meets the cross flow at an angle. Rains reasoned that a

correction to this model was necessary because of the viscous effects which were manifested through the tip and end-wall boundary layers. He also stated that the pressure driven flow is a perfect fluid phenomenon while the shear flow due to rotation is a real fluid phenomenon. His experiment later showed that the two cannot be treated separately.

According to Rains, the perfect fluid effects dominate the real fluid effects in determining the clearance flow. He solved the two-dimensional potential flow problem and compared the results with an experiment. Rains placed a hydrofoil normal to a wall which contained static pressure taps in the configuration of the airfoil profile. By running the experiment at various clearances and Reynolds numbers, it was determined that viscous effects are dominant when  $\lambda Re_c \ll 1$ , and inertia forces are dominant when  $\lambda Re_c \gg 125$ . Rotational effects were neglected, and Rains admitted that the assumption limits the application of the results.

Rains calculated the laminar flow field in the clearance for a stationary blade. First, he used the techniques of complex variables and conformal mapping to solve for the pressure field. Second, he solved the Navier-Stokes equations without the inertial terms. In comparing the real fluid model with the perfect fluid model, the validity of the solution for  $\lambda Re_c \ll 1$  was reinforced. To incorporate both viscous and inertia terms, the Bernoulli equation was solved with loss terms added. The rotation of the machine was included by simply adding the kinetic energy normal to the blade to the Bernoulli equation.

Rains could not evaluate the model directly, so he assumed that the kinetic energy of the velocity component normal to the free stream is not recoverable. Rains substantiated this by claiming that the rolled up vortex dissipates this energy without recovery. In this manner, losses were calculated and compared to measurements with good agreement.

Rains studied the formation of the end-wall vortex in some detail. His first step was the calculation of a parameter defining the degree of deformation. Next, the vortex core radius and length were given in terms of this parameter. The circulation and cavitation number of the vortex followed. These equations can be written as:

$$t^* = \frac{(\xi/c) C_{L_{tip}}}{\lambda \epsilon} \quad (2.3)$$

$$r_c = 0.14ht^{*0.85} \quad (2.4)$$

$$b = 1.0ht^{*0.72} \quad (2.5)$$

$$\Gamma^* = \lambda \epsilon \left( \frac{4 + C_{L_{tip}}}{C_{L_{tip}}} \right)^{\frac{1}{2}} \frac{b}{h} \quad (2.6)$$

$$\sigma = -C_p + \frac{C_{L_{tip}} (4 + C_{L_{tip}}) \left(\frac{b}{h}\right)^2}{8\pi^2 \left(1 + \frac{r_c}{h}\right)^2} \quad (2.7)$$

Inherent in these equations are the following assumptions: 1) the blade has zero thickness, 2) the pressure distribution is constant along the chord, 3) the lift coefficient is estimated at the tip, and

4) the contribution of secondary vorticity to the leakage vorticity is zero.

Rains also performed end-wall vortex cavitation experiments to determine the effect of rotation. In both the stationary and rotating case, the cavitation number increases with decreasing flow coefficient. In the stationary case, the lowest cavitation numbers exist for the smallest clearances. However, in the rotating case for  $\lambda < 0.1$ , the cavitation index increased with decreasing clearance height. Rains concluded that rotation strongly affected the end-wall vortex location and structure and that the tip clearances should not be the smallest possible to construct. Using his analytical model, Rains calculated the cavitation index at various stations along the chord for the design flow coefficient. A discrepancy of 20 percent was noted. Rains concluded that he had not correlated the cavitation index with all of the important parameters for end-wall vortex cavitation, and that bubble dynamic effects should be included. However, it is evident that one or more parameters of the tip flow field were omitted from the correlation.

Mitchell [43] completed an experimental investigation of cavitation in the tip region of an axial-flow pump. His objectives were to determine the variation of cavitation number with flow coefficient, both for tip clearance and blade surface cavitation, and to study the mechanism of tip clearance flow. Mitchell stated that the variations in cavitation number are determined by the total effect of three factors: tip incidence, tip-clearance flow velocity, and static pressure rise through the blade row.

Mitchell described the individual effects of each of the factors. The effects of increasing incidence are to decrease the minimum pressure and move the position at which it occurs toward the leading edge. Incidence is dependent upon the flow coefficient and tip clearance. The static pressure rise through the rotor blade row will also affect the cavitation number, according to Mitchell, because it may modify the chordwise suction pressure distribution obtained from the tip incidence and tip clearance flows. He also noticed two forms of cavitation: blade surface cavitation due largely to the two-dimensional characteristics of the tip section and end-wall vortex cavitation formed as a result of the interaction of the tip clearance flow with the main flow. Mitchell made several important conclusions. First, except at high flow coefficients, there exists an optimum value of the tip clearance to maximum tip thickness ratio between 0.09 to 0.105. Blade surface cavitation appeared at clearances below the optimum value, and end-wall vortex cavitation appeared at clearances larger than the optimum value. Second, larger flow coefficients had smaller cavitation inception numbers. Finally, the optimum clearance value was independent of RPM and flow coefficient. It seemed likely, Mitchell theorized, that the optimum clearance was dependent on another parameter which would also be a function of the end-wall boundary layer.

Shalnev [44] conducted cavitation experiments in which he modified the geometry of the blade tip and end-wall. The slope of the clearance walls and the condition of the inlet edge were altered during the test.

The two degree diverging wall version with a rounded inlet provided the lowest overall cavitation inception number.

McCormick [45] performed an analytical and experimental study of cavitation produced by the vortex trailing from several types of wings. He showed that the minimum pressure coefficient of a tip vortex depends on the boundary layer thickness on the pressure side of the blade and on the local lift. McCormick also showed that the cavitation number scaled as Reynolds number to a power. This was confirmed by Gearhart and Ross [46]. Finally, the importance of air content in varying the cavitation number of the tip vortex was emphasized. This phenomenon was also addressed by Billet and Holl [47].

Similar to Shalnev's work, Gearhart [2] conducted an investigation to determine the best tip shape for optimum cavitation performance. In the analysis, he neglected viscous effects and used Bernoulli's equation in combination with a perturbation approach borrowed from Rains. The angle of the leakage flow with the chord was related to the lift coefficient at the tip. The strength of the vortex sheet due to the leakage flow was also calculated. Since the experiment was conducted in a wind tunnel, the cavitation results were implied by the minimum pressure coefficient. Gearhart stated that reducing the clearance exit velocity improves the end-wall vortex cavitation performance and that reducing the separation in the tip region improves gap cavitation. The combination of a rounded pressure side and diverging gap would seem to provide the best overall cavitation performance; however, Gearhart questioned whether the increased mass flow through the clearance would reduce the efficiency of the machine.

Gearhart and Ross [46] continued the work of Gearhart [2] in a subsequent experiment at the Garfield Thomas Water Tunnel. Experimental data was given showing the dependence of end-wall vortex cavitation on Reynolds number and tip clearance. A scaling relationship for end-wall vortex cavitation was presented. Resistance to end-wall vortex cavitation decreased with increasing Reynolds number and tip clearance. The optimum dimensionless clearance was also found to be 0.125 in agreement with Rains [27], Mitchell [43], and Shuba [1].

It is difficult to determine what parameter in the flow field that can be modeled by a Reynolds number. Gearhart and Ross gave an expression which states that the cavitation inception number varies as the ratio of Reynolds numbers raised to the power  $n$ . This value of  $n$  was found to depend upon the tip clearance to maximum tip thickness ratio. This differed from McCormick's value of 0.4 which was based on experiments on an isolated, stationary hydrofoil. The differences between a stationary foil and a rotating blade row are obvious: namely the existence of the casing boundary layer, secondary flows, and the radial boundary layer of the rotor. The inherent difficulties of cavitation scaling are realized in the work of Okamoto et al. [48] and Narita et al. [49] who attempted to compare model and full scale end-wall vortex cavitation results for a shrouded propeller.

Shuba [1] studied end-wall leakage vortex cavitation on a 12-inch diameter pump and made significant progress in correlating the relevant parameters which affect end-wall vortex cavitation. Cavitation inception data were obtained for six gap spacings, three different incoming boundary layers, and three reference velocities. All tests

were operated at design flow coefficient. Flow visualization was also done with the oil-paint-film technique. A simple correlation model was derived based on a Rankine vortex tangential velocity distribution.

## 2.6 Current Correlation Model of End-wall Vortex Cavitation

One can make several observations from the literature, subject to experimental verification, which form a foundation for the present work. The simple correlation model of Shuba [1] incorporates several sub-models from the literature and represents the most complete model of the end-wall vortex phenomenon. If the end-wall vortex is assumed to have a Rankine tangential velocity distribution, then the cavitation index can be related to the minimum pressure coefficient of the vortex as follows:

$$\sigma = -C_{P_{\min}} = 2 \left( \frac{\Gamma}{2\pi r_c V} \right)^2 \quad (2.8)$$

The circulation about a section of a finite wing is given by:

$$\Gamma = C_L W \frac{c}{2} \quad (2.9)$$

The determination of  $C_L$  was complicated because of the end-wall which retains a portion of the lift. Shuba borrowed a sub-model from Rains for the variation of  $C_L$  with the clearance. The expression for the lift in the vortex was then

$$C_{L_{tv}} = B \sqrt{\lambda} \quad (2.10)$$

where  $B$  is an unspecified constant. A sub-model for the core size  $r_c$  was also borrowed from Rains. Using Lakshminarayana's assumption that

the sheet radius is roughly equivalent to the core radius, the sub-model for the core size is

$$r_c = 0.14 h \left(\frac{h}{c}\right)^{-0.85} \left(B \sqrt{\lambda}\right)^{0.425} \left(\frac{\xi}{c}\right)^{0.85} \quad (2.11)$$

Combining the four previous equations, an expression for the cavitation inception index results

$$\sigma = 0.646 \left(B \sqrt{\lambda}\right)^{1.15} \left(\frac{W_1}{U}\right)^2 \left(\frac{c}{h}\right)^{.30} \left(\frac{\xi}{c}\right)^{1.70} \quad (2.12)$$

The parameters in the expression are the clearance and incidence velocity which is a function of the boundary layer profile. The constants are B,  $\xi$ , the tip speed U, and the blade geometric properties t and c. The value of  $\xi$  is the location of  $C_{p_{\min}}$  which is usually the location of maximum tip thickness. The model developed by Shuba agreed well with his experimental data and the experimental data of Mitchell and Gearhart. Shuba noted that the results showed a significant variation with RPM through a constant B. A linear dependence of B upon Reynolds number was found. The functional forms for the shed lift coefficient and the vortex core radius must be verified, and this investigation is suitable to that end.

## Chapter 3

## EXPERIMENTAL FACILITIES AND PROCEDURES

3.1 Hydrodynamic and Mechanical Design

A High Reynolds Number Pump (HIREP) Facility was designed to conduct studies of cavitation and related fluid dynamic phenomena in the rotor tip region. The purpose of this facility is to provide an axial-flow multi-blade row pump of sufficient size to accommodate a variety of instrumentation in both a stationary and rotating frame. Several advanced instrumentation systems for blade static pressure measurement, dynamic tip clearance measurement, and cavitation viewing were developed. The hydrodynamic and mechanical design, the instrumentation systems, and the operating characteristics of HIREP are discussed in this chapter.

HIREP consists of a 42-inch diameter pump stage driven by a 48-inch diameter downstream turbine. A mechanical drawing of the facility is shown in Figure 3.1. The two units rotate together on a common shaft in the 48-inch diameter test section of the Garfield Thomas Water Tunnel. The energy losses incurred in the system are overcome by the main drive impeller near the second turn of the Water Tunnel as shown in Figure 3.2. The facility is analogous to a gas turbine engine where the air is compressed, then burned with fuel in the combustor, and finally expanded through the turbine. The energy contained in the fuel of the gas turbine is comparable to that provided by the tunnel main drive impeller.

Five blade rows comprise the HIREP facility. The upstream blade row or inlet guide vanes provide a specified distribution of swirl at

- MAXIMUM BLADE REYNOLDS NUMBER OF 8 MILLION • 1200 HP TURBINE DRIVE
- VARIABLE RPM (40-400) • MAXIMUM AXIAL VELOCITY 50 FT/SEC

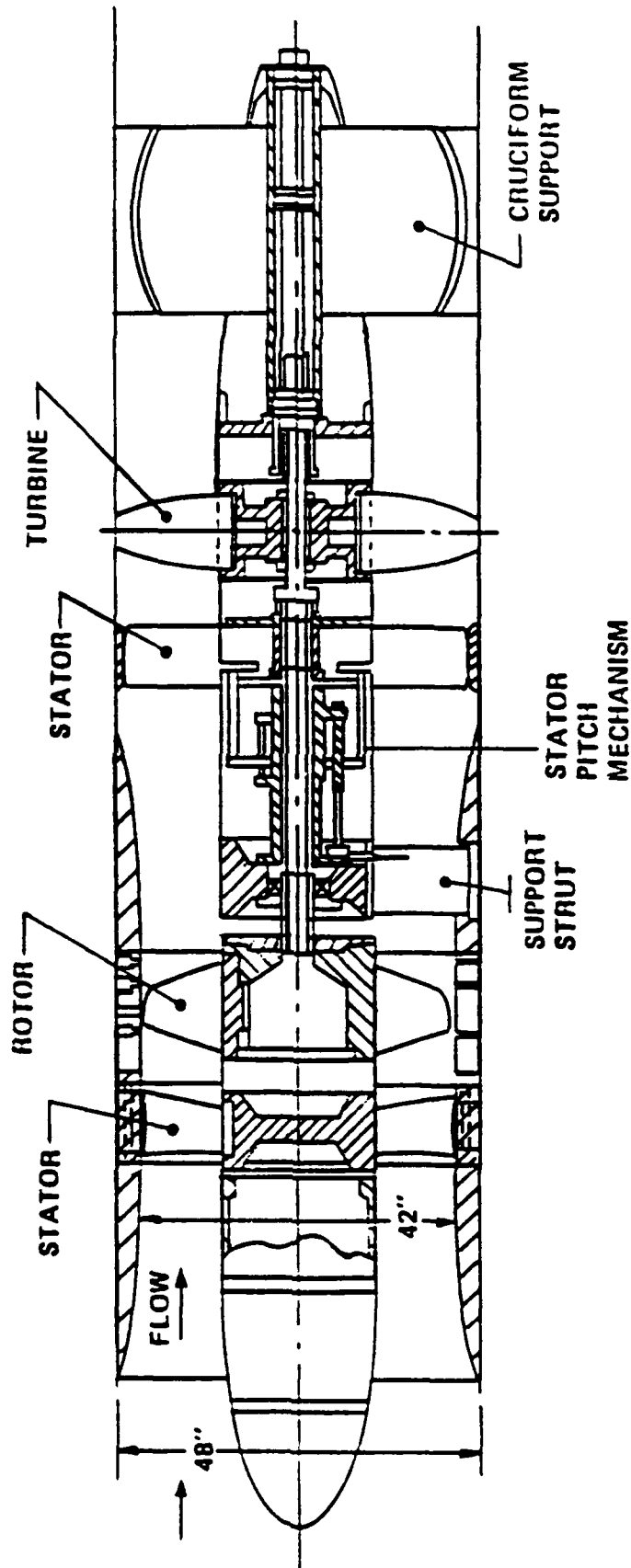


Figure 3.1. Mechanical Drawing of the High Reynolds Number Pump

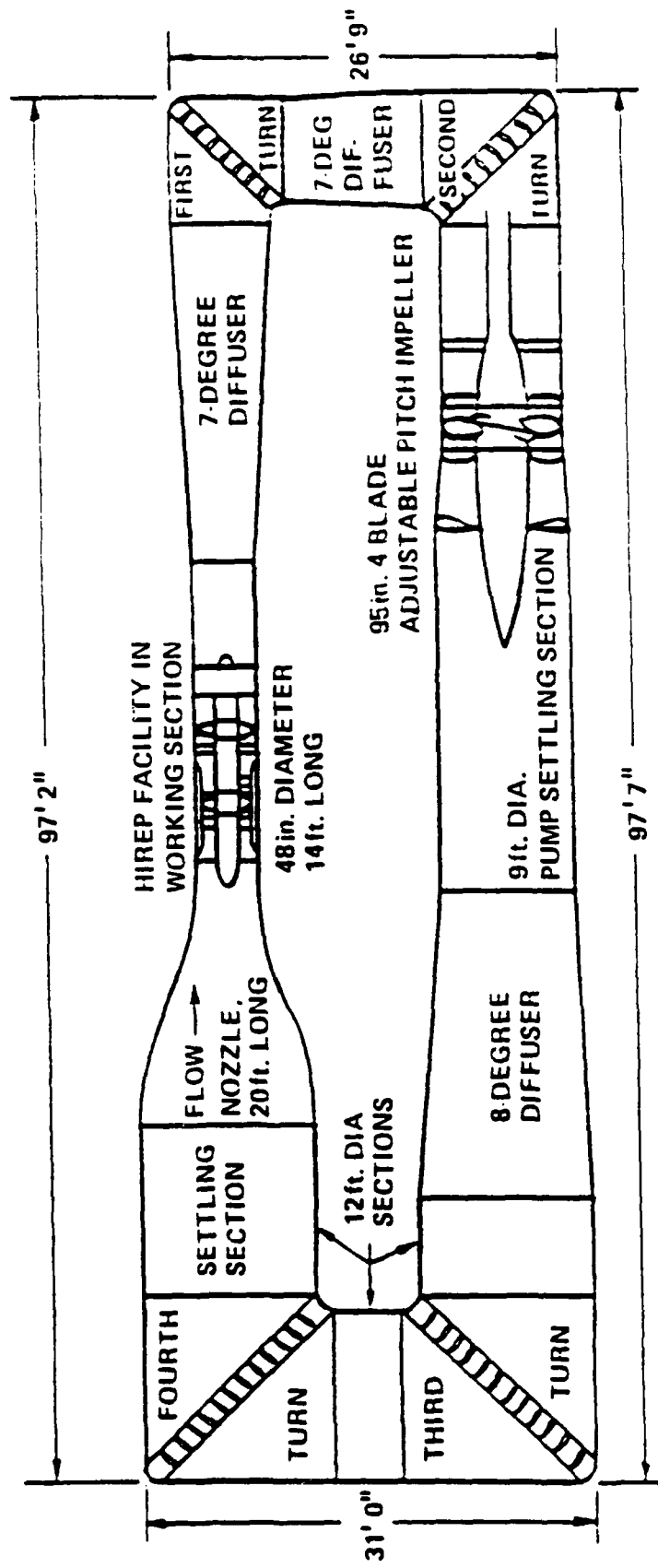


Figure 3.2. Relationship of the High Reynolds Number Pump to the Garfield Thomas Water Tunnel

the rotor leading edge which is essentially uniform circumferentially. The viscous wakes and secondary flows influence the rotor in terms of overall performance, cavitation, and unsteady forces. The IGV's are also structural members for the forward centerbody.

The second blade row is the pump rotor. The rotor consists of a hub with individual blades attached to mounting blocks. The hydrodynamic shape of the blades is determined by consideration of spanwise loading, the amount of swirl generated by the inlet guide vanes, and the power available from the regenerative turbine. One of the independent variables of this investigation, the tip clearance, is varied by changing the thickness of spacers installed under the blade mounting blocks. Several blades contain special instrumentation which will be discussed subsequently. A spanwise cavity in the blades provides a passage for wire leads from the blade-tip to pass into the hub chamber. A large disc welded to the driveshaft is bolted to the hub. The upstream end of the hub is open to allow access to the instrumentation and is sealed after electronic connections have been made. The rotor is capable of absorbing 1200 hp at a through-flow velocity of 50 ft/s. At this condition, a blade chord Reynolds number at mid-span of six million based on relative velocity is attained.

Downstream of the rotor is a set of structural vanes which provide support for the main shaft bearing. The strut hub contains the upstream termination of the centerbody support housing. This housing contains lubrication for the bearing and is an attachment point for the turbine inlet guide vane pitch mechanism.

The fourth blade row is a set of adjustable turbine inlet guide vanes. The pitch is continuously variable from minus forty degrees to plus fifteen degrees, relative to the shaft centerline. The adjustment capability is external to the facility and thus allows variability during operation. A swash plate, which is the common slider of fourteen slider-crank linkages, one for each vane, provides simultaneous adjustment without binding. The swash plate moves axially along four keys and is guided by two cylindrical rods. A power screw and miter gear set transmits control of this mechanism to the Water Tunnel exterior.

The fifth blade row is the regenerative turbine. The pitch of the turbine vanes is discretely variable in 2.5 degree increments. The blades are cast integral with a cylindrical base which is held stationary by a retaining ring. The downstream end of the shaft is supported by a cruciform strut assembly which houses a thrust bearing for the driveshaft. A fared enclosure further downstream provides a passage for wire leads connecting the stationary end of the slip-ring unit with the data acquisition equipment and the power supplies.

The hydrodynamic design of the HIREP facility was performed utilizing the Streamline Curvature analysis method [50]. The method is an Euler solver which includes loss models associated with each blade row. The results yield predictions of velocity and pressure profiles at the blade row leading and trailing edges. For the design of HIREP, the flow through four blade rows was solved simultaneously. The spanwise loading on the turbine was modified in order to balance the torque. The analysis predicted an overall hydraulic efficiency of

approximately 75 percent, relative to generated power on the HIREP drive shaft.

Initial questions of system starting and stability led to the construction of a one-sixth scale model. A photograph of the air model is illustrated in Figure 3.3. A bell-mouth inlet was installed on the upstream end while a transition into a centrifugal blower was installed downstream of the turbine. An axial velocity of 50 ft/s was achieved with a corresponding angular speed of 1600 RPM. There were no undesirable transients or unstable operating characteristics observed during the testing of the air model. On the basis of these tests and the flow analysis, the full size HIREP facility was mechanically designed and fabricated. A photograph of the facility in a 48-inch fixture is illustrated in Figure 3.4.

### 3.2 Instrumentation System

The High Reynolds Number Pump Facility contains provisions for a wide range of fluid dynamic measurements and methods. The high capacity, low-noise slip-ring unit accommodates many measurements in the rotating frame. Thin, wide ribbon cables were used to bring instrumentation leads from the rotor tips through the hollow passages in the rotor blades to a centralized collection of insulation displacement connectors in the hub chamber. Ribbon cables with high flexing capability also carry signals from the hub termination to the slip-ring unit and from the slip-ring unit to the data acquisition equipment and power supplies outside of the facility. The hollow rotor blades, hub chamber, and driveshaft provide passages for the

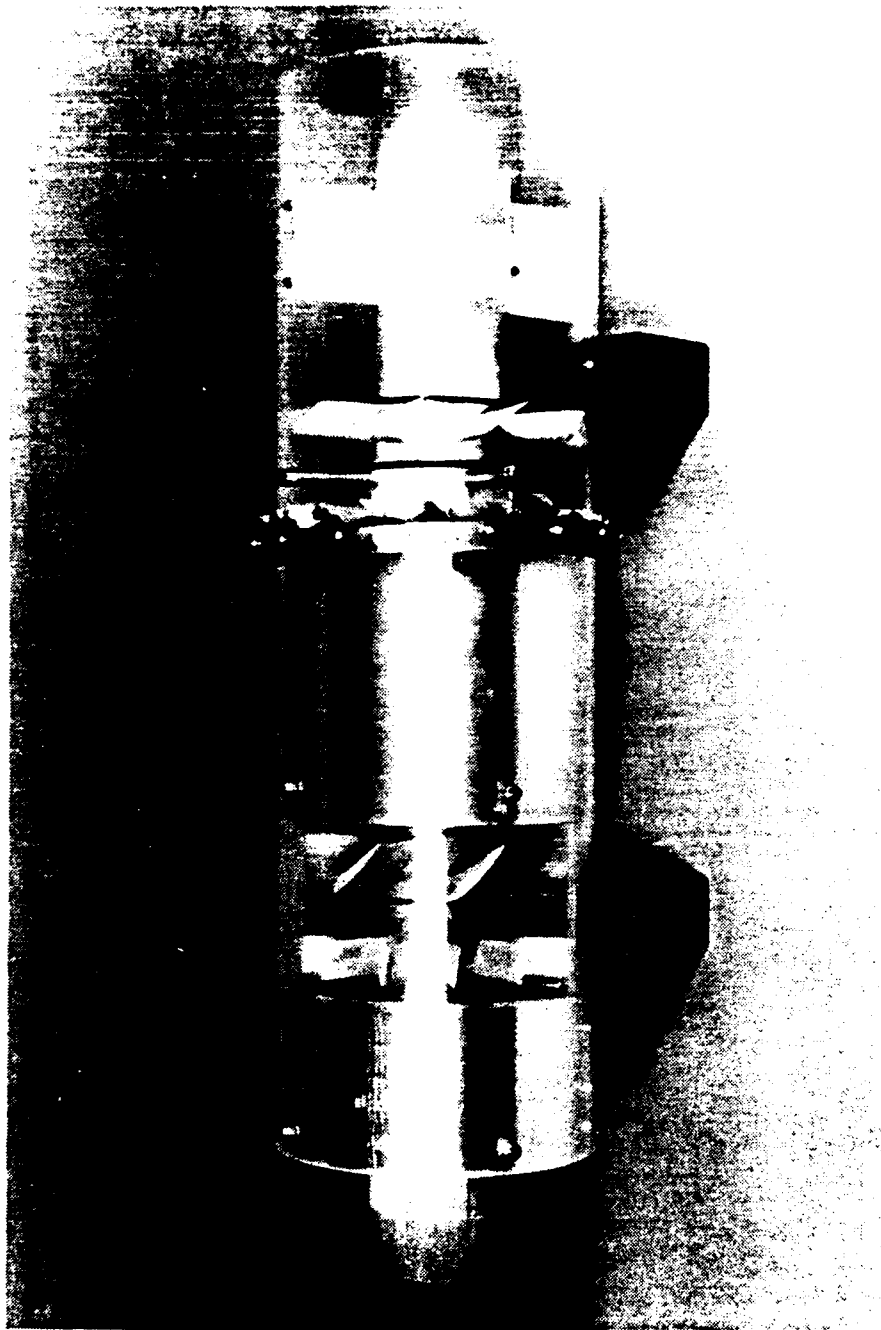


Figure 3.3. Photograph of the One-sixth Scale Model of the High Reynolds Number Pump

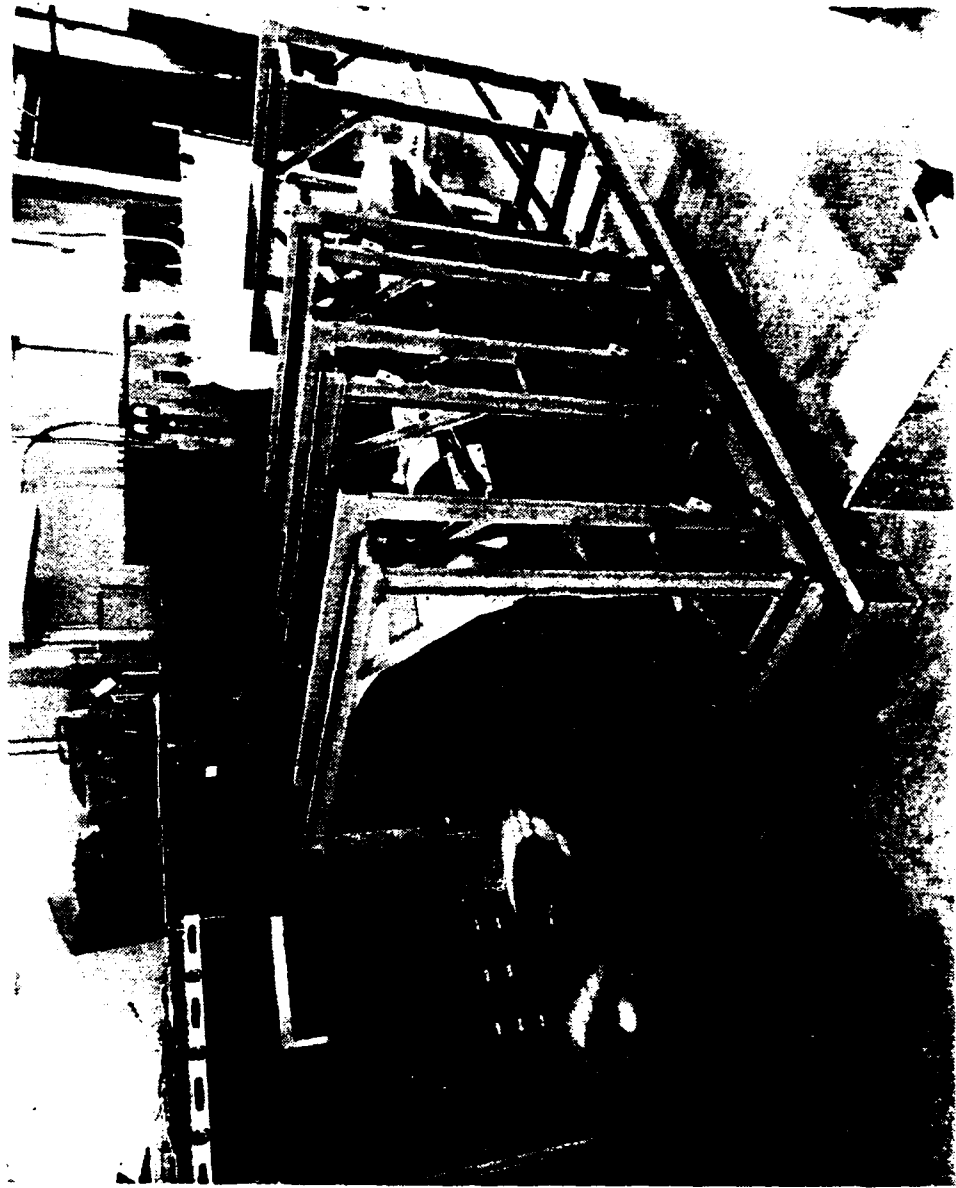


Figure 3.4. Photograph of the High Reynolds Number Pump in the 48-inch Fixture

cables. The cables are held stationary wherever possible to prevent chaffing. The signals from the transducers are acquired through an extensive acquisition system consisting of a low pass filter (where applicable), an integrating voltmeter, a multiplexer, and a VAX computer system. The data are manipulated through a large software package, called the Data Acquisition and Data Reduction (DADR) Program, which was developed specifically for the Garfield Thomas Water Tunnel. Furthermore, since the facility is housed in the test section of the Water Tunnel, numerous ports and windows are available for visual observation, laser velocimetry, and other instrumentation access on the stationary reference frame.

Many types of measurement systems were used in the facility: laser velocimetry in the pump stage, radially traversing five-hole probes in every stage, and a number of transducers in the rotating frame of reference: steady and unsteady pressure transducers, force and torque cells, and accelerometers. In addition, several unique measurement systems were developed specifically for the subject cavitation studies. The following paragraphs describe the instrumentation used for the cavitation studies. A block diagram of the instrumentation system is given in Figure 3.5. A downstream view of the rotor cross-section in Figure 3.6 illustrates the location of the instrumentation.

### 3.2.1 Laser Velocimetry

A laser velocimeter (LV) system was used to measure the flow field at the rotor tip inlet, exit, passage, and gap flow fields in



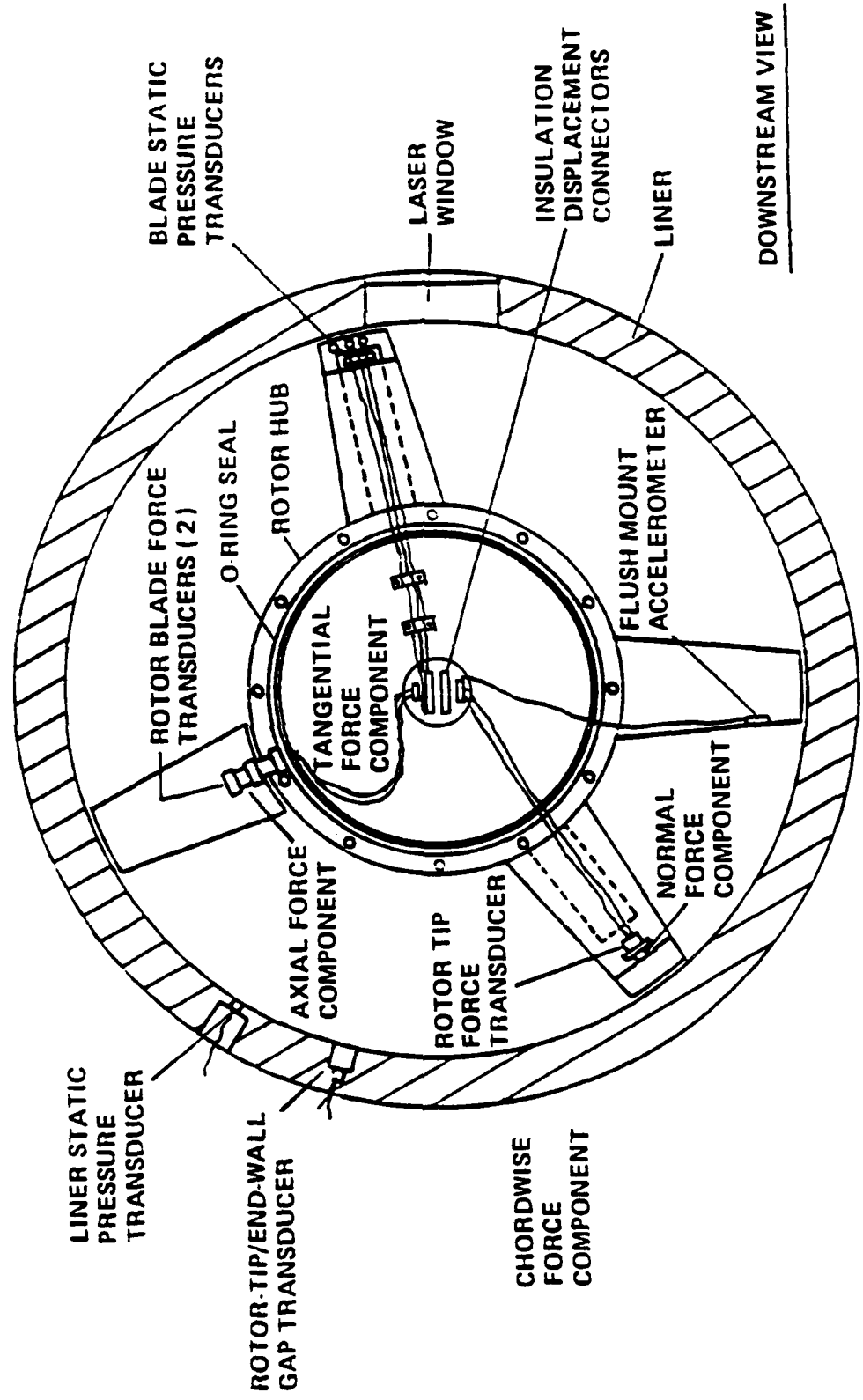


Figure 3.6. Downstream Cross-sectional View of the Rotor Hub

the axial and tangential directions. A schematic of the system is illustrated in Figure 3.7. The laser and associated optics were mounted on a three-axis traversing table. The table was used to position the location of the beam cross-over spot in the horizontal plane of the tunnel centerline. In the dual backscatter mode, the light scattered from particulate passing through the control volume was collected through the transmitting lens and focused on an aperture in front of a photomultiplier. The counter-processor filters and digitizes the information from the photomultiplier signal for processing by a VAX computer. The data collection continues until the desired number of samples has been collected. The data include the rotor angle, mean velocity, turbulence intensity, skewness, kurtosis, and the number of samples within each bin. The bin size (angular increment) can be varied in post processing to produce plots of different resolution.

The measurements were made on the test section centerline through a specially designed tunnel window. The outer radius of the window was designed to produce a zero net magnification cylindrical lens. As a result, both control volumes for each component of velocity cross at the same location. Data were collected using the field point measurement system. In this procedure, the laser beam crossover is stationary, and each LV measurement sample is tagged with the angular position of the rotor via the shaft encoder. Each test consisted of 8,000 or 50,000 data points distributed into 3600 bins, one for each one-tenth of a degree.

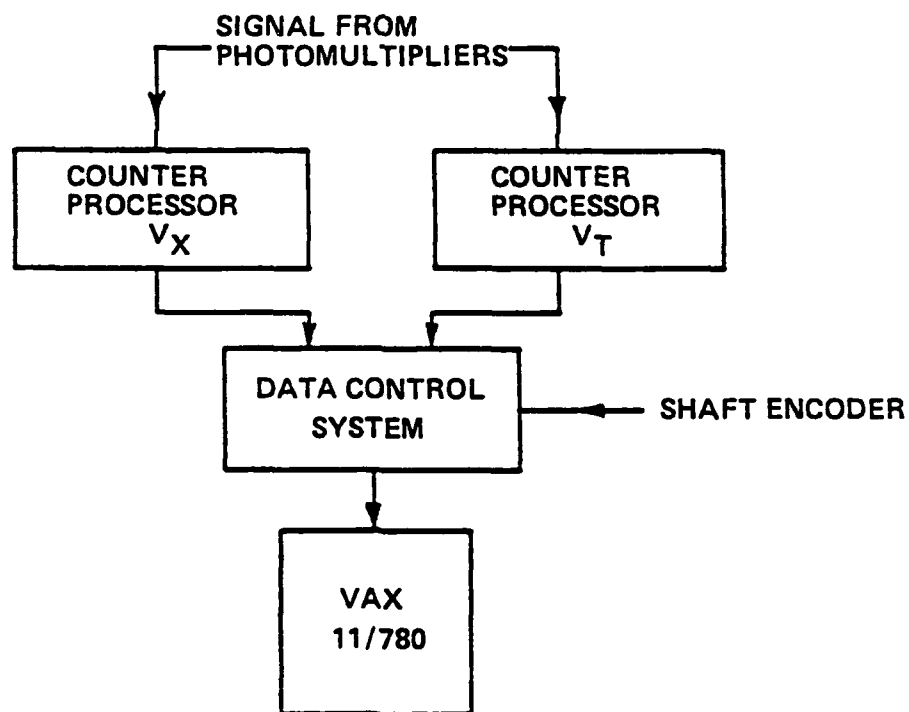
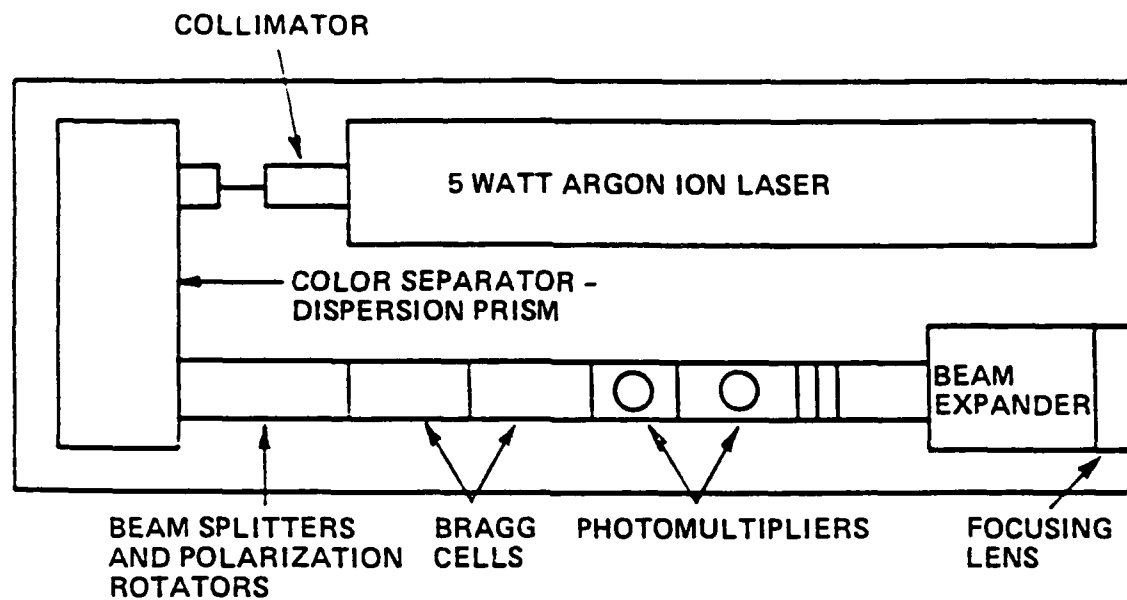


Figure 3.7. Schematic of Laser Velocimeter System

The primary objective of the LV surveys was to measure the effect of rotor tip clearance on the leakage flow and subsequent end-wall vortex. Surveys of the leakage vortex were completed at two axial stations, 0.5 inches and 2.75 inches downstream of the rotor trailing edge. The cavitation of the end-wall vortices was used to locate and record their angular position as derived from the encoder signal conditioning unit. Velocity surveys were also completed at several chord positions in the tip clearance gap, at several locations within the blade-to-blade passages, and at the rotor tip inlet. In all instances, the control volume was moved in subsequent runs of a given test to measure the flow field at different radial positions.

### 3.2.2 Conventional Velocity and Pressure Measurement

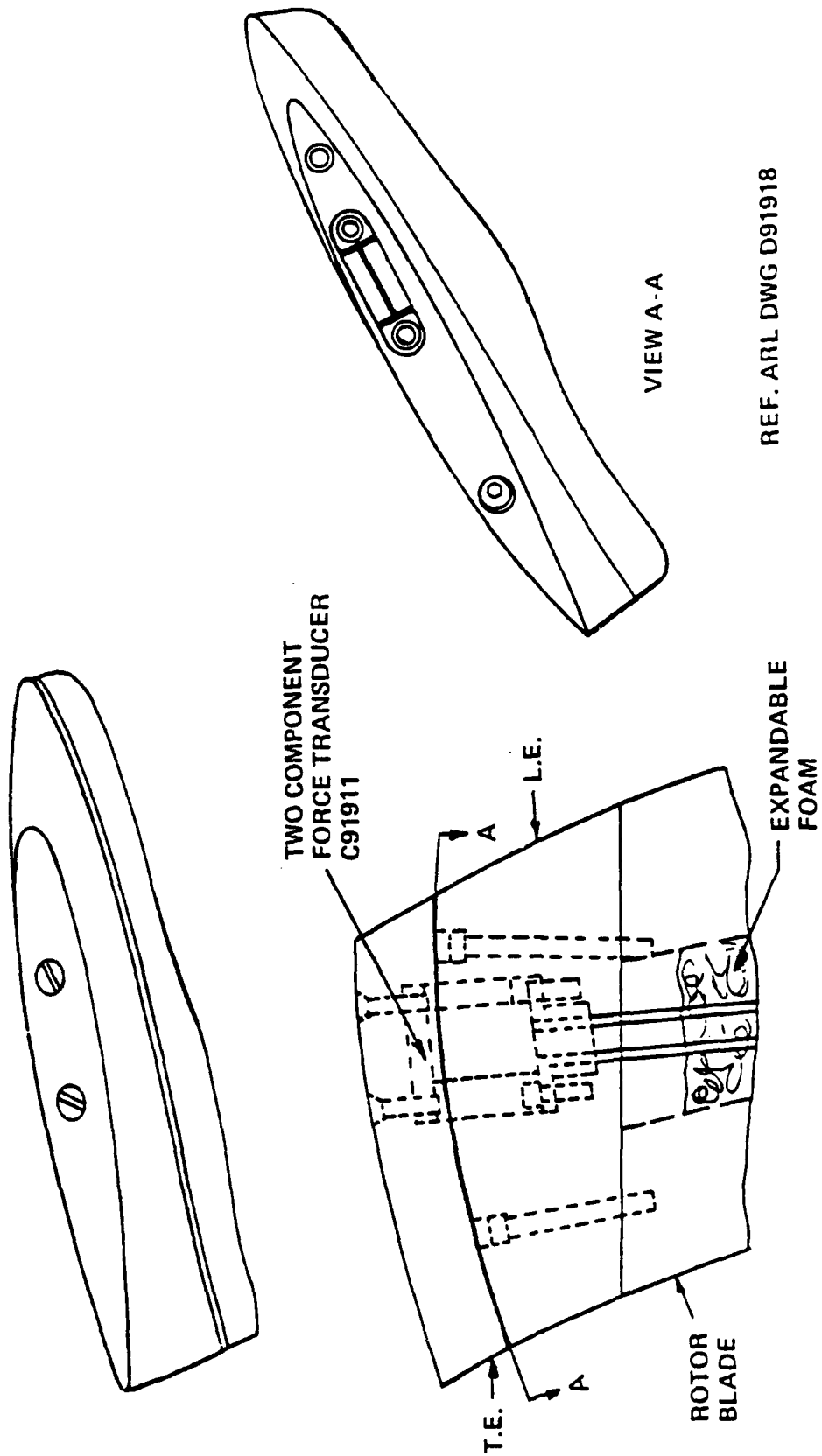
Five luminaire windows on the removable cover of the Water Tunnel were replaced with drilled metal inserts. Traversing five-hole probe assemblies were attached to the exterior of the inserts, and the probe traversed radially through a fitting, the drilled hole, and into the flow field. The probes were located at the inlet and exit of the rotor, at the inlet of the turbine inlet guide vanes, at the exit of the turbine inlet guide vanes, and at the turbine exit. A pitot-static probe was placed upstream of the rotor inlet guide vanes where the forward centerbody and the liner are parallel and was used to calculate a velocity through the facility. A total pressure probe in the nozzle upstream of the test section and a static pressure port in the test section were also used to determine the axial velocity through the pump. The static port was located at the same axial

position as that of the four static holes on the pitot-static probe. The latter velocity measurement was used as the reference velocity and for data normalization. The pressure from this static port was used as the input to the pressure regulating system. A differential pressure transducer and a bourdon tube pressure transducer were used to display the tunnel static pressure both digitally and in analog form. The hydraulic lines from each of the probes were connected to a bank of differential pressure transducers located on the tunnel centerline. The transducers were calibrated prior to the tests and were bled and zeroed at the beginning and end of each test.

### 3.2.3 Force and Torque Measurements

#### 3.2.3.1 Tip Force Measurement

The top 10 percent of the rotor blade span was instrumented with a two-component force transducer to measure the steady-state hydrodynamic loads. A diagram of the transducer assembly is given in Figure 3.8. The transducer consists of two orthogonal shear webs, one above the other. The tip of the rotor blade is attached to the remaining portion of the blade through the transducer mounting flanges. Both components were powered with a 3.5 volt DC source which is remotely sensed at the bridge to account for line loss. The powering and signal leads were connected to the connector plate in the hub chamber. The wire leads for the transducer pass from the hub connector plate, through the hollow passage in the blade body, through a gland on the bottom of the transducer, and on to the strain gauge solder tabs.



REF. ARL DWG D91918

Figure 3.8. Tip Force Transducer Assembly

The tip force transducer was designed to produce two shearing members: one sensitive to the chordwise force and the other to the normal force. The shear measuring technique has several advantages. First, the point loading of a cantilevered beam produces a constant value of the shear force along the length of the beam, whereas the moment diagram is sloped. Thus the point of action of the force is not required to determine the load. Second, the shear stress is maximum at the neutral axis of the beam cross section; however, the bending stress is maximum at the outer fiber of the beam. The location of the strain gauges near the neutral axis is preferred because waterproofing and compact wiring are more convenient. The principal strains caused by the shear forces are measured by mounting the strain gauges at forty-five degrees to the longitudinal axis. The wiring of the strain gauges in the four-active-arm Wheatstone bridge causes the cancellation of outputs due to bending and torsional strains. Moreover, deflections of less than 0.001 inches are inherent in the shear beam measurement technique. A computer algorithm was developed to provide rapid optimization of mechanical, electrical, and geometrical parameters. The computed sensitivities were within 5 percent of the actual values.

#### 3.2.3.2 Rotor Blade Force Measurement

The rotor blade force was measured by two two-component shear beams transducers which were mounted in the base and extended radially outward through a portion of the blade span. Each transducer measured the force in the axial and tangential direction relative to the axis

of rotation. A diagram of the assembly is given in Figure 3.9. The shear measuring technique as outlined above in Section 3.2.3.1 was also the basis for the rotor blade force transducer design. The four Wheatstone bridges were powered with a five volt DC source. Since two dual component transducers were used in this measurement, the pitching moment of the rotor blade can also be calculated.

The transducers were fabricated from round steel stock to simplify attachment to the blade span and base. Line-to-line fits were maintained on both ends of the transducer. The base was also pinned, and the blade span was attached with four dog-point set screws as shown in Figure 3.9. A groove was machined circumferentially on each transducer for the set screw points. The intent was to allow minute rotations of the transducer body while still preventing separation of the blade span from the transducer. The minute rotations must be avoided because they introduce unknown moments in the static equilibrium of the blade. The transducers were fabricated from precipitation-hardening stainless steel because of the high yield strengths attainable with a simple heat treating operation.

#### 3.2.3.3 Torque Measurement

The torque on the HIREP driveshaft was measured via a four-active-arm Wheatstone bridge of strain-gauges bonded to the inner diameter. Again, as in the shear measuring techniques discussed hereinabove, the gages were bonded at forty-five degrees to the shaft centerline and spaced 180 degrees apart in groups of two. The axial location of the strain gauges is between the rotor hub and the main

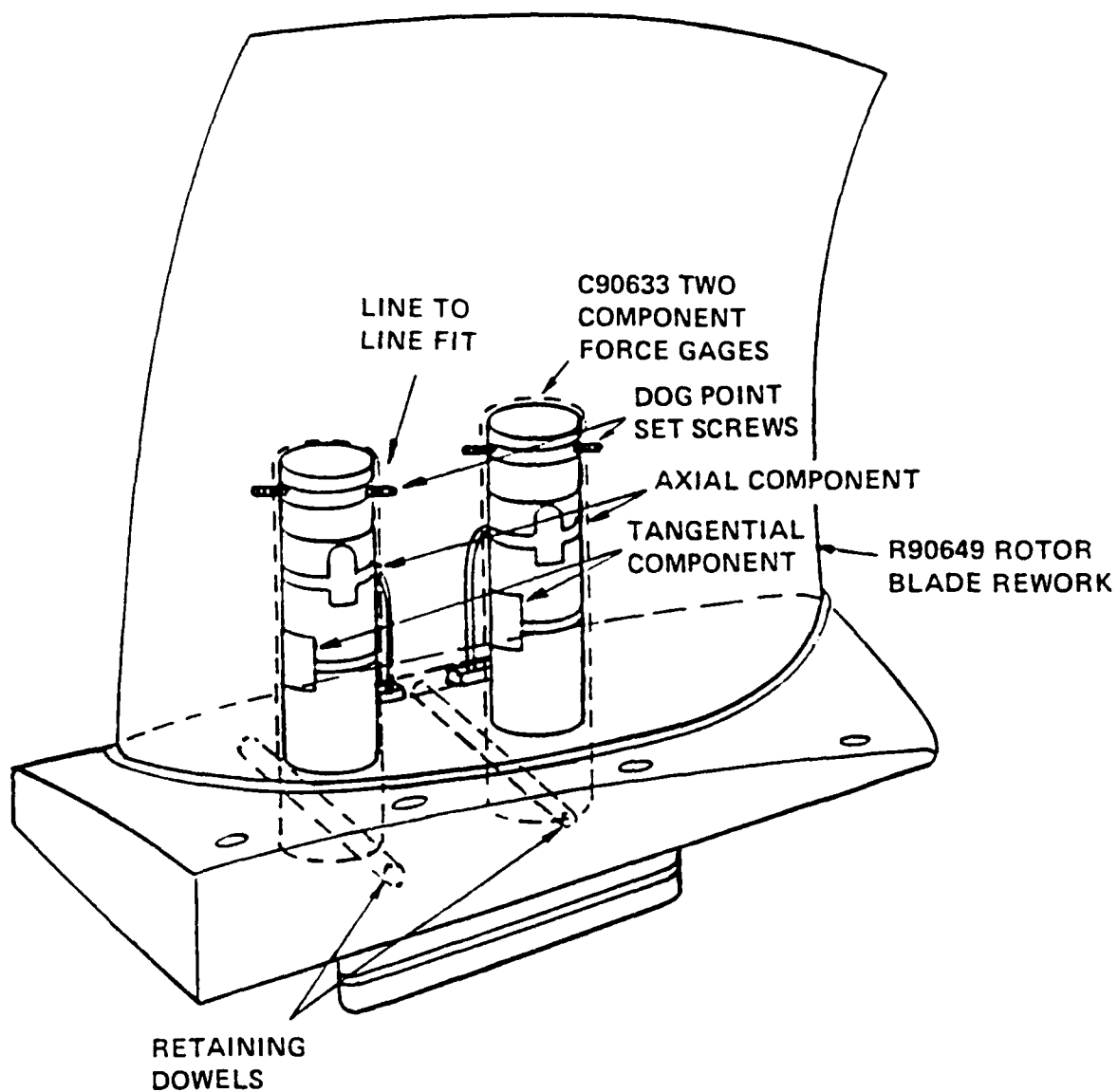


Figure 3.9. Blade Force Transducer Assembly

shaft bearing. The arrangement of the gauges is such that the output of the bridge is not sensitive to adverse loads and bending moments. The leads to the torque cell attached to the hub chamber connector plate. The bridge was powered with a five volt DC source. The input voltage was sensed at the bridge to account for line loss. The strain gages were potted with silicone rubber to prevent damage from humidity and from the four ribbon cables which lie in the inner diameter of driveshaft.

#### 3.2.3.4 Calibration of Force and Torque Transducers

Each of the force and torque transducers was calibrated prior to the tests. Since each of the force transducers had two components, a two-by-two matrix of calibration coefficients was required. The method was to load the cell in each of the orthogonal directions, one at a time, and record the output of both bridges on the transducer. In this manner, both the principal, diagonal terms and the cross talk, off-diagonal terms of the coefficient matrix can be calculated. The cross talk terms were a small fraction of the diagonal terms as expected; nevertheless, they were included for accuracy. The tip force transducer was calibrated over its entire operating range. Because of the large forces and torques generated on such a large turbomachine, the rotor blade force transducers and the torque cell were calibrated over approximately 10 percent of the operating range. The assumption of linearity over the entire range is a good assumption when the stresses are much lower than the yield point and when the strain gauge is correctly bonded to the metal surface of the web.

#### 3.2.4 Blade Static Pressure Measurement

The static pressures on the blade tip surfaces are of interest in any investigation of leakage flow phenomena; consequently, several pressure transducers were located at the 99% span position on both surfaces, on the rotor tip surface, and on the inner diameter of the casing. The transducers consisted of stainless steel diaphragms which were bonded with a four-active-arm Wheatstone bridge of semiconductor strain gauges. Both the steady-state and unsteady pressures can be measured with the piezoresistive transducer; however, the former is the exclusive use of the transducers in the subject investigation.

The transducers were cylindrical in shape with a diameter of one-eighth of an inch and a length of one-quarter of an inch. Five leads were located at the rear of the small module. The design included a temperature compensating and bridge balancing element between the two positive output leads. However, in the present application, there was not sufficient space for this compensating element, so it was omitted. An evaluation of the transducer sensitivities at several temperatures showed that the temperature dependence was small but not negligible. Consequently, the transducers were calibrated in situ. The procedure will be discussed subsequently in Section 3.4.

The logistics of imbedding the transducers in the blade surface, connecting the electrical leads, and maintaining accuracy in a wet, cavitating, rotating environment proved to be an interesting exercise in itself. The transducers were mounted in the blade from the opposite side in which the measurement was to be made. The mounting

holes were drilled slightly oversized, and the transducer was cemented in with epoxy. On the measurement side of the blade, a small brass insert containing a Helmholtz cavity was pressed into the hole. The cavity was filled with petroleum jelly to match the acoustic impedance of water. The intent was for the transducer to seat against the insert, forcing the petroleum jelly out of the small pinhole and thus eliminating any trapped air from the cavity. The purpose of the Helmholtz cavity was to protect the diaphragm from the high pressures generated from bursting cavitation bubbles without compromising the useful frequency range of the transducers in the event of unsteady pressure measurements. The transducer mounting arrangement is illustrated in Figure 3.10. The pressure transducer on the rotor tip surface was mounted through an access hole on the blade face. The transducer on the pump casing was mounted in a manner similar to those mounted on the blade surface.

The leads from the three transducers located on the rotor blade were channeled along the blade surface to a hole in the blade. Inside the blade tip, a slot was machined for a small printed circuit board. This board was the common termination of the transducer leads as shown in Figure 3.10. A fifty conductor cable was used to connect the pressure transducers in the tip to the hub chamber connector plate via a right angle header on the printed circuit board. The cable was fastened down where possible, and the hollow passage in the rotor blade was filled with foam rubber to prevent chaffing of the cable.

The transducers had an operating range of 0 to 50 psia. Based on a three volt DC source, the sensitivities were of

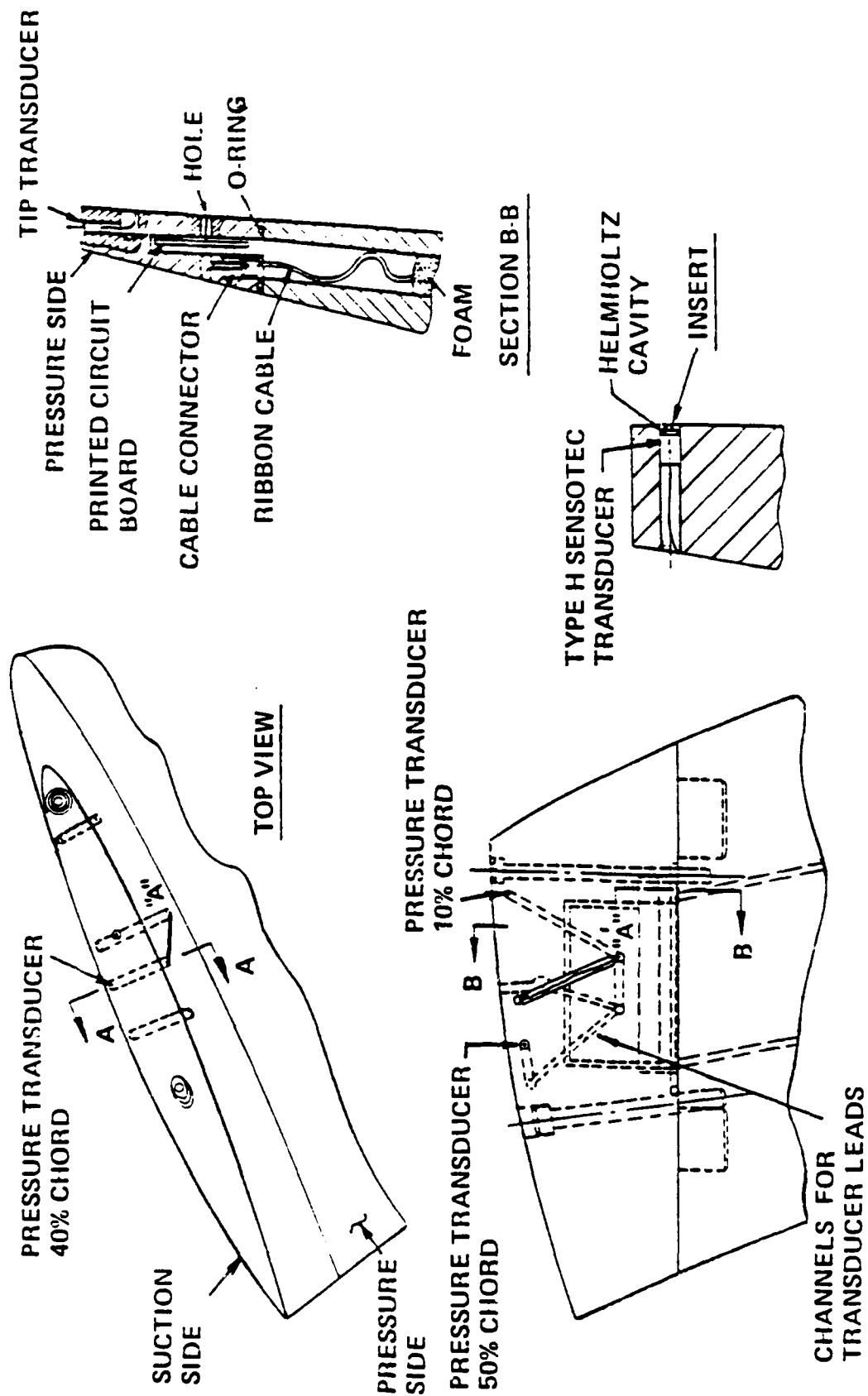


Figure 3.10. Pressure Transducer Mounting Arrangement in the Rotor Tip

the order of one millivolt per psi. Calibrations were performed before and after installation in the rotor blade. A deadweight, pressurized air calibrator was used for this purpose. A dynamic calibration was also conducted using the comparative technique in a standing wave tube; however, the unsteady pressures were not measured due to the high zero offset, low signal to noise ratio, and the fact that the unsteady pressures were of secondary importance in this investigation.

### 3.2.5 Dynamic Tip Clearance Measurement

One of the fundamental independent variables of this investigation is the tip clearance between the rotor tip and the end-wall. Due to the dynamic nature of a rotating turbomachinery blade, it is questionable whether the tip clearance remains constant during operation. Certainly, the blades of the compressor and turbine in a gas turbine engine grow due to both dynamic and thermodynamic loading as discussed in Chapter 2. To address this question in the High Reynolds Number Pump (HIREP), a dynamic measuring system was developed to measure the rotor tip clearance during operation.

The basic components of the system are a fifteen volt power supply, an oscillator, a linearization network, amplifiers, a demodulator, the transducer, and an analog-to-digital acquisition system. The variable impedance transducer was placed in the casing surrounding the pump such that the face of the transducer was flush with the casing inner diameter. The impedance in the coil is changed by eddy currents which are induced in the conductive, metallic rotor

tip. The relative interaction between the blade tip and the transducer is directly proportional to their displacement. Using the encoder output, the gap of any particular blade can be measured by sampling the transducer output during the correct angular window. A bell shaped curve is formed as the blade passes the transducer; thus the resulting signal was digitized, and a simple software program searched for the minimum voltage and applied the calibration. The minimum voltage corresponds to the point when the rotor tip is directly over the transducer face. A block diagram illustrating the operation of the dynamic gap measuring system is illustrated in Figure 3.11.

#### 3.2.6 Cavitation Viewing

The standard method of cavitation viewing is through stroboscopic lighting triggered by the home pulse of the shaft encoder. An adjustable delay between the home pulse and the strobe trigger allows one to vary the angular position of the illuminated region. At high rotational speeds, the blade appears stationary because the eye blends the individual pictures together similar to a motion picture projection. However, at lower rotational speeds, the eye is unable to integrate the pictures into one continuous image and substantial flicker is observed by the observer. A low-RPM video viewing system was developed which captures a stroboscopically illuminated image and maintains a display of this image on a video monitor until the next image has been digitized and placed in memory. A video cassette recorder was used to save the cavitation tests for post-test review.

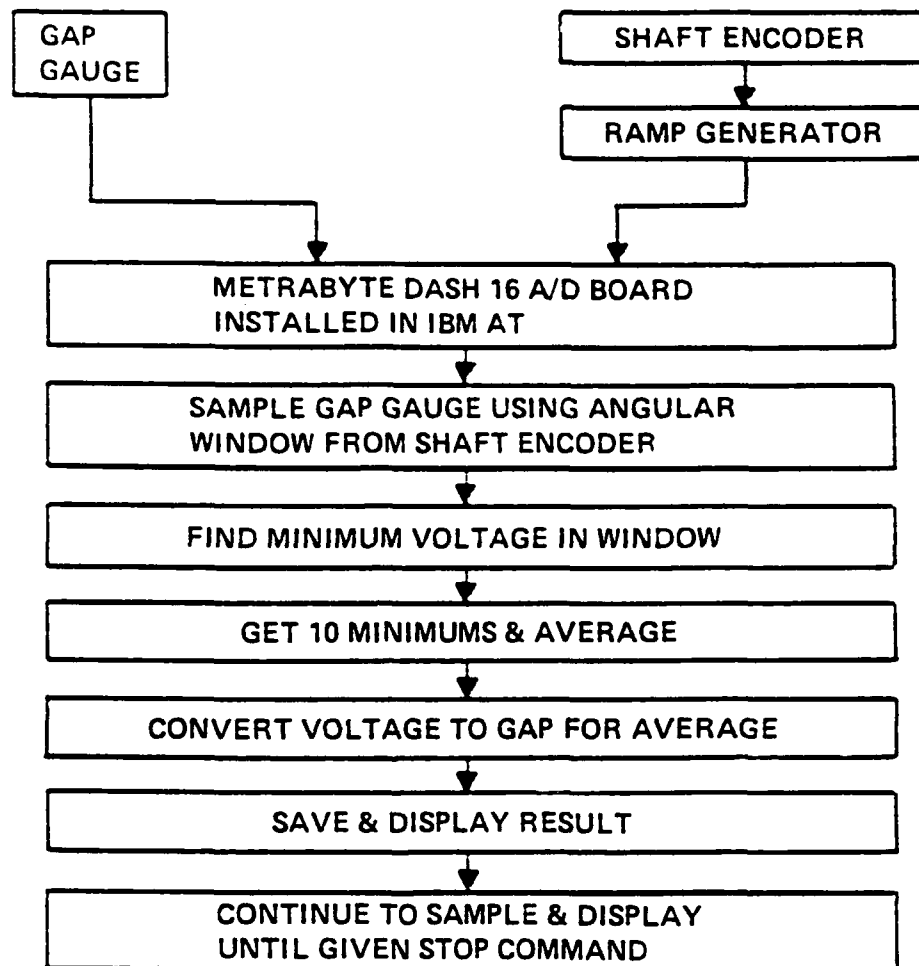


Figure 3.11. Block Diagram of the Dynamic Tip Clearance Measurement System

### 3.2.7 Angular Speed and Position

An incremental, optical shaft encoder was used to provide angular position and speed. The encoder was mounted near the downstream end of the slip-ring unit. The encoder produces 3600 pulses per revolution, one every one-tenth degree. One of these has a higher voltage than the other 3599, and is termed the home pulse. A encoder interface unit, built in-house, produces a saw-tooth wave which rises and falls once per revolution. This signal was used during the dynamic gap measurement as outlined above in Section 3.2.5. In addition, the encoder interface unit has an output for the counter which measures the angular speed of the rotor and a trigger for the low-RPM viewing system.

### 3.3 Operating Characteristics

An evaluation of HIREP's operating characteristics was the first test conducted on the new facility. The performance was evaluated using measurements of shaft torque and change in total pressure over the stages. A five-hole probe located at the 50-percent mass flow streamline was used for this purpose. The limitations of single point measurements, when used to quantify the performance, should be noted. Ideally, a mass averaged value of the total pressure would be desirable, but the long span of the blades and the high velocities were prohibitive to a full radial traverse.

The shaft of HIREP begins to rotate at approximately five ft/s and rotates at 40 RPM at the nominal flow coefficient. Axial

velocities of 50 ft/s are possible with rotational speeds reaching 400 RPM. The flow coefficient of the machine is adjustable by changing the stagger angle of the turbine inlet guide vanes. By making this adjustment, the amount of swirl entering is changed, and the torque delivered to the rotor is varied. A counter on the pitch mechanism makes it possible to return to the exact position of a previous data point. The range of flow coefficient can be adjusted by changing the stagger angle of the turbine blades when the facility is not operating. These two capabilities give a wide range of operation.

The operating static pressure range at the inlet to the machine is 6 to 50 psia. This pressure range was adequate to conduct the cavitation tests. The turbine blade tips are also a source of cavitation; however, the flow has received a static pressure rise from the rotor and has diffused before it reaches the turbine. The by-pass loop of the Garfield Thomas Water Tunnel was utilized to degas the water to a desired level. Further details concerning the Garfield Thomas Water Tunnel are given by Lehman [51]. Further details concerning the hydrodynamic design, the instrumentation system, and the operating characteristics are discussed by Farrell, McBride, and Billet [52].

#### 3.4 Experimental Procedures

Several types of tests were conducted during the present investigation in the High Reynolds Number Pump (HIREP). Performance tests consisted of force measurements, blade tip static pressure measurements, and five-hole probe surveys. During the cavitation

tests, only the pressure of desinent cavitation was measured with those parameters necessary to define the operating point of the pump. Thus the velocity, torque, tunnel static pressure, pump angular speed, and tunnel temperature were common measurements among all the test types. The performance and cavitation data were collected using the Data Acquisition and Data Reduction (DADR) Software developed at the Water Tunnel. A data acquisition system separate from the DADR program was used for the laser velocimeter because of the additional complexities inherent in the system. The dynamic gap measurement was accomplished using a stand-alone personal computer. This made it possible for simultaneous data collection with the laser velocimeter. A description of the various tests is discussed in the following paragraphs.

Prior to filling the large 48-inch diameter Water Tunnel, the rotor blades were adjusted with spacers to obtain the desired tip clearances. The tip clearance was measured statically near the cavitation viewing window using a hole gage. The hole gage was adjusted so that it just passed through the gap. A digital micrometer was used to measure the diameter of the hole gage. The large mass of the hub and the fact that the center of mass of the rotor blades was near the hub allowed one to run with different tip clearances on the blades without significant vibration.

In addition, the cables from the instrumented blades were connected to the hub chamber connector plate. After sealing the hub with the cover plate, the tunnel was partially filled, and pressurized air was forced through the inner passageways. If leaks were present,

bubbling would occur. Once the integrity of the seals was established, the hatch cover was put on the test section, and the tunnel filled completely and pressurized. Next, the hydraulic tubes from the ports and probes were attached to the transducers and allowed to bleed. Offset voltages are measured before and after the test to account for zero drift. The change in zero offset is varied linearly with time over the duration of the test with the data reduction procedure.

Depending on the required measurements for a performance test, other preparatory steps were required. For the in-flow boundary layer survey, a five-hole probe was mounted on the hatch cover of the test section. The probe was traversed from the 50-percent mass flow streamline to the pump casing in one tenth inch increments. When blade static pressure measurements were made, an in-situ calibration was conducted. After filling and pressurization, the water tunnel pressure was increased in discrete increments while recording the output of the transducers. In this manner, a calibration coefficient was calculated at the temperature of the medium. When the force transducers were used, the positive directions were verified by applying a positive load and observing the sign of the output.

All of the tests were conducted as a function of the flow coefficient and reference axial velocity through the flow annulus. Once the desired velocity was reached, the turbine inlet guide vanes were adjusted to provide the desired flow coefficient. In this manner data points could be taken over a range of flow coefficients. The adjustment was made during operation of the facility at velocities

less than 30 ft/s. For the performance tests, three data points were taken at one condition and averaged. Once data was taken over the range of flow coefficients, the main drive impeller rotational speed was changed to adjust the velocity.

After the performance tests were completed the desinent cavitation tests were conducted on the same configuration. After filling, and pressurization, a sample of water was taken from the tunnel. The Van Slyke Manometer was used to determine the air content of the water on a mole basis. If the air content level was greater than 10 ppm, the degassing system was run for a length of time while repeated measurements of air content were made. Air content effects were accounted for with a procedure outlined in Section 4.1. With the tunnel filled and pressurized, the velocity and flow coefficient were set to the desired point. Next, the tunnel operator lowered the pressure until fully developed end-wall vortex cavitation appeared as viewed with the aid of the low-RPM viewing system. At this point, the pressure was systematically increased until only trace flashes of cavitation were observed, i. e. about once every three seconds. At this point the static pressure was entered into the computer, and the transducer outputs required to define the nominal operating point and cavitation index were sampled. At least two values of the cavitation number were used to determine an experimental value at a particular condition.

At the conclusion of the performance and cavitation tests, the oil-paint flow visualization technique was employed on the pump rotor.

A mixture of cadmium orange and heavy weight oil was applied to the tip section of the rotor blades. One of the blades was painted entirely. Each of the blades was set to a different tip clearance to observe the streak pattern as a function of this variable. The operating point of 36 ft/s at a flow coefficient of 1.33 was achieved as rapidly as possible, and then the tunnel drive was shut down. The blades were then carefully removed from the rotor hub for photographing.

## Chapter 4

## EXPERIMENTAL RESULTS

4.1 Cavitation Results

Cavitation occurs when the pressure at a point in the liquid equals the vapor pressure of the liquid. Moreover, the pressure reduction is formed by the dynamic action of the liquid in the interior and/or boundaries of the system. The resulting vapor bubbles may grow in size, and voids or cavities can be formed. The presence of cavitation in turbomachines can lead to vibration, material erosion, and performance breakdown. Traditionally, the cavitation performance of a turbomachine is described by the Thoma cavitation parameter, which is the ratio of the total head above vapor pressure, or the net positive suction head (NPSH), divided by the head change across the impeller. The cavitation performance of a turbomachine can also be quantified by the cavitation index,  $\sigma$ ,

$$\sigma = \frac{P_{\infty} - P_v}{\frac{1}{2} \rho U^2} \quad (4.1)$$

The definition of Equation 4.1 will be used for the present investigation, where  $P_{\infty}$  is the static pressure in the upstream annulus. A high index usually means poor cavitation performance.

End-wall vortex cavitation indices were determined in the High Reynolds Number Pump (HIREP) for three flow coefficients and for axial velocities of 26, 31, and 36 ft/s on three blades. The data were acquired with different values of liquid air content level. The

effects of air content level on the cavitation index have been understood for some time.

A procedure was developed to account for the air content effects so that all cavitation indices could be compared on the same basis, even though tests were conducted at different air content levels. Billet and Holl [47] noted that tip-vortex cavitation is strongly affected by the free gas content which can be correlated with the liquid air content level. Ignoring the dynamic and surface tension effects, the cavitation number was defined by Billet and Holl [47] as

$$\sigma = -C_P + \frac{P_G}{\frac{1}{2} \rho U^2} \quad (4.2)$$

Holl [53] indicated that the gas pressure could be approximated by Henry's law

$$P_G = \alpha \beta k \quad (4.3)$$

where  $\alpha$ ,  $\beta$ , and  $k$  are the dissolved gas content, Henry's law constant, and an empirical adjustment factor, respectively. By substituting Equation 4.3 into Equation 4.2 and rearranging one obtains

$$-C_{P_{\min}} = \sigma - \frac{k\alpha\beta}{\frac{1}{2} \rho U^2} \quad (4.4)$$

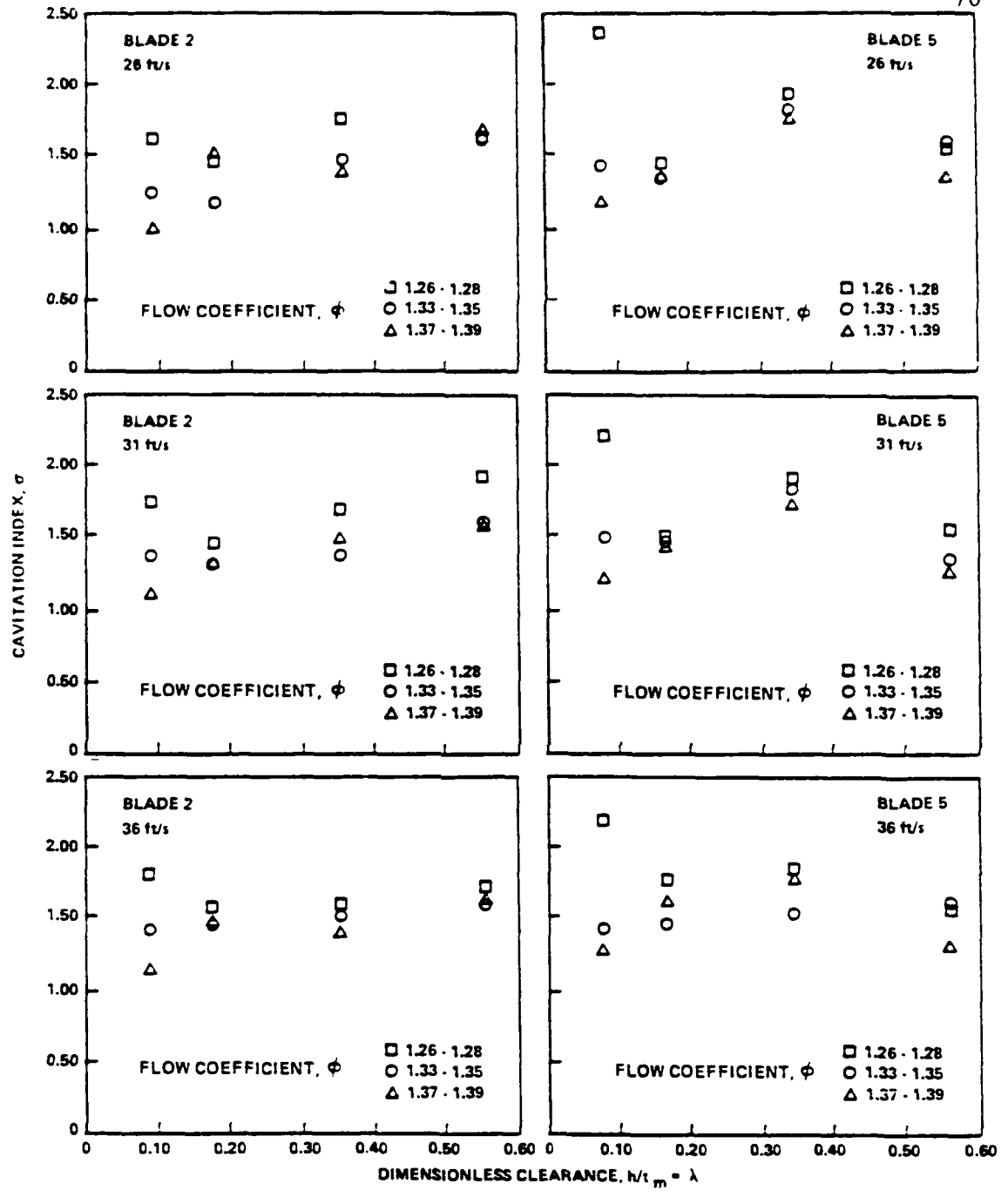
where the unknowns are  $k$  and  $C_{P_{\min}}$ . Two cavitation tests at different air content levels were conducted at the same flow conditions. The same rotor blades were examined in each test. Ideally, the value of  $C_{P_{\min}}$  is identical for the same flow conditions. Thus, the value of  $k$  was determined by minimizing the difference in  $C_{P_{\min}}$  for the two tests conducted at different air content levels. Using this procedure, the

value of  $k$  was found to be 0.11, and this value was used to account for air content effects in subsequent cavitation indices obtained from the HIREP facility.

The values of end-wall vortex cavitation number obtained for this experiment are given in the Appendix with appropriate flow conditions and the dimensionless tip clearance. Data were obtained as a function of axial velocity, flow coefficient, and tip clearance. By examining one parameter while the others are held constant, one can evaluate the influence of this parameter on the cavitation index.

#### 4.1.1 Cavitation Index versus Tip Clearance

The cavitation data from the Appendix are plotted in Figures 4.1a, 4.1b, and 4.1c for blade numbers 2, 5, and 6, respectively, as a function of tip clearance. The values of the cavitation index recorded for the High Reynolds Number Pump were normalized by a dynamic pressure based on the tip speed. For the 1.26-1.28 and 1.33-1.35 ranges of flow coefficient, the curve of  $\sigma$  as a function of tip clearance indicates a minimum occurring at a dimensionless tip clearance near  $\lambda = 0.15$ . An optimum tip clearance for cavitation performance was also noted by Rains [27], Mitchell [43], and Shuba [1] for a dimensionless tip clearance near 0.15. Mitchell and Shuba noted that for clearances less than  $\lambda = 0.15$  gap cavitation was observed, and for clearances greater than  $\lambda = 0.15$  end-wall vortex cavitation was observed. Rains observed end-wall vortex cavitation for all clearances tested except  $\lambda = 0.026$ . However, this value is much smaller than normal operating clearances. For the subject data,

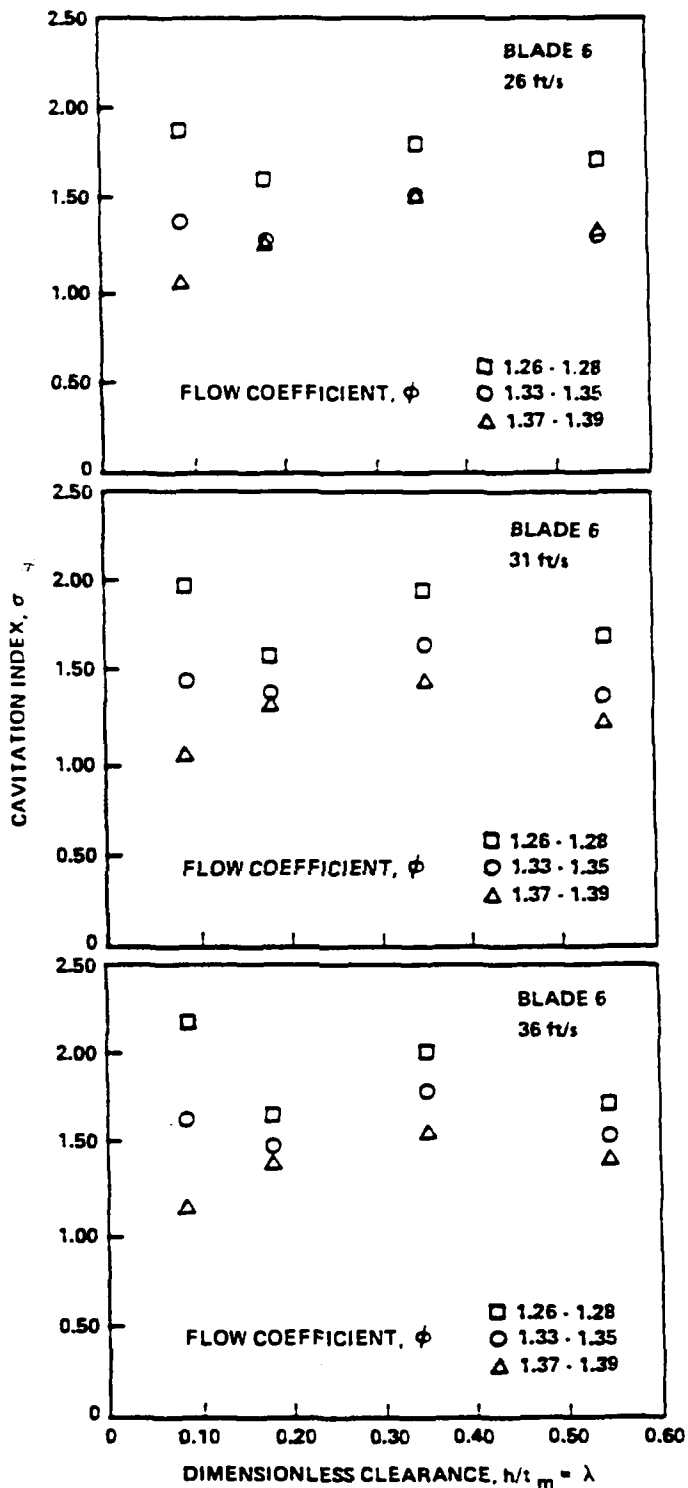


(a)

(b)

Figure 4.1. Cavitation Index versus Dimensionless Clearance at Axial Velocities of 26, 31, and 36 ft/s Representing  $Re_c$  of  $1.6 \times 10^6$ ,  $1.9 \times 10^6$ , and  $2.2 \times 10^5$  for a) Blade Number 2, b) Blade Number 5, and c) Blade Number 6

(cont. on next page)



(c)

Figure 4.1 (cont.)

cavitation was observed in a region indicative of end-wall vortex cavitation. The maximum cavitation number usually occurred for tests conducted at the smallest tip clearance.

Clearly the characteristics of the flow field in a small tip clearance provide conditions for vortex formation. The pressure difference across the blade is largest relative to larger tip clearances. For larger tip clearances, the angle between the leakage and through-flow velocity vectors is smaller as is the magnitude of their resultant because of the smaller pressure difference across the blade tip. The angle of the leakage flow is clearly observed by the streaklines generated by flow visualization studies discussed in Section 4.6. The concentration of circulation is high in the case of a small tip clearance. The leakage vorticity is the sum of other vorticities generated and shed at the tip. The pressure side boundary layer flow is a principal contributor to the vorticity in the leakage vortex. The angle of the leakage flow with the chord line is representative of the pressure difference at the tip and determines the length scale for the dissipation and disorganization of the boundary layer vorticity across the tip surface. For a small tip clearance, this length scale is minimized.

For  $0.15 < \lambda < 0.35$ ,  $\sigma$  increases for all flow coefficient ranges except for two values measured in the 1.37 - 1.39 flow coefficient range at 26 and 36 ft/s. Both these values were measured on the same blade. Data taken near  $\lambda = 0.33$  illustrates this point. The blade lift on the tip varies in an inverse exponential manner as the tip clearance is increased. Thus near the wall the tip lift changes more

rapidly with tip clearance. For values of tip clearance near  $\lambda = 0.35$ , it seems reasonable that while the shed lift has lessened somewhat, the mass flow through the clearance has increased significantly. The main result of larger clearances, then, is to increase the momentum and hence the strength of the leakage vortex. This increased strength results in a lower minimum pressure coefficient and thus a larger cavitation index. The dependence of the strength and size of the end-wall vortex on the tip clearance will be discussed subsequently.

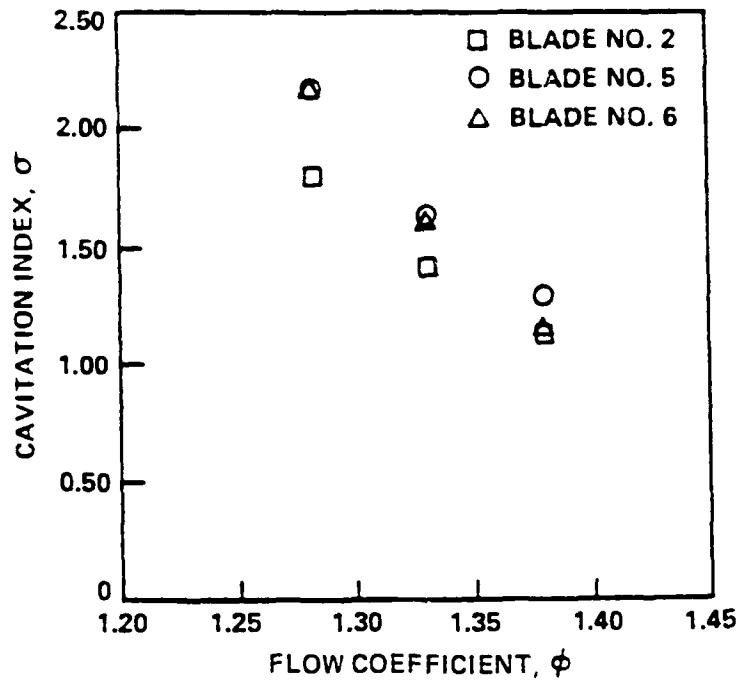
For  $0.35 < \lambda < 0.55$ ,  $\sigma$  decreases for the data taken on blades five and six with the exception of data taken in the flow coefficient of range 1.33 - 1.35 on blade five for an axial velocity of 36 ft/s. For blade two, the cavitation index is largest at  $\lambda = 0.55$ . The massflow through the clearance is maximum while the lift on the rotor tip is minimum relative to the other smaller clearances. The angle of the leakage velocity vector with the chordline is small, and hence a large portion of the blade tip surface provides dissipation to the kinetic energy of the leakage jet. Several laser velocimeter (LV) surveys in the tip clearance of the rotor showed that the kinetic energy of the fluid in the subject gap is reduced from its value at a position near the mid-chord to a smaller value near the trailing edge of the rotor blade. These surveys will be discussed further in Section 4.5.2. It is not clear from the data whether the cavitation index is increasing or decreasing; but it is clear that as the clearance is widened, the pump rotor begins to operate as an open propeller, i. e. all of the tip lift is shed into the conventional tip

or trailing vortex. The cavitation number should then asymptotically approach a value representative of this condition.

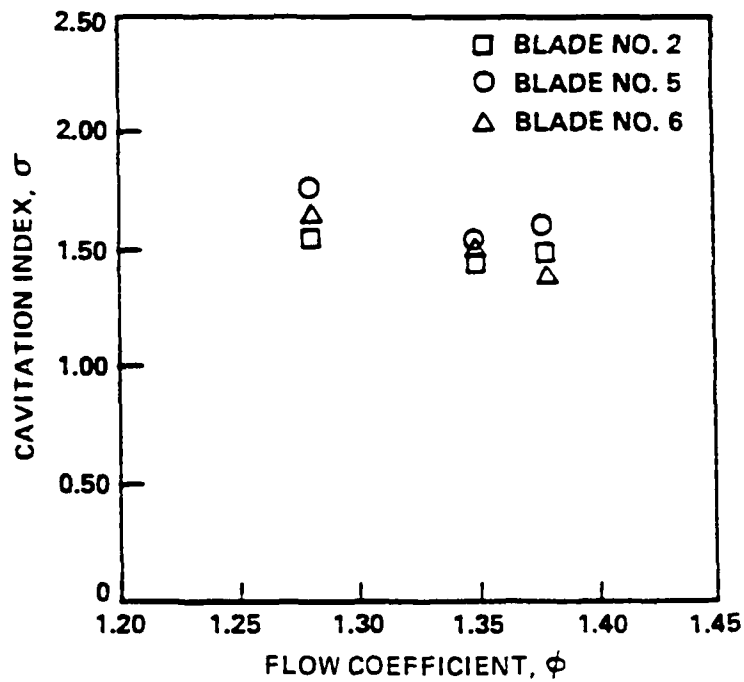
#### 4.1.2 Cavitation Index versus Flow Coefficient and Angular Speed

The cavitation data are presented in Figures 4.2a, 4.2b, 4.2c as a function of flow coefficient for constant tip clearance. It is obvious that the derivative of  $\sigma$  with respect to flow coefficient is greatest in magnitude for the smallest tip clearance. As mentioned in section 4.1.1, the smallest tip clearance represents the highest incidence angle and thus the greatest pressure difference across the blade tip.

For constant flow coefficient and tip clearance, the angular speed is increased by increasing the axial velocity through the facility. By examining the data in this way, one can estimate the effect of the pressure side boundary layer in terms of Reynolds number over this small range of 26 to 36 ft/s. The variation in cavitation index over this range of Reynolds Number was less than 0.3  $\sigma$ 's. The variation of cavitation index with Reynolds number has been discussed by McCormick [45] and Gearhart and Ross [46]; for a trailing vortex from a stationary wing, the cavitation index was shown to vary with Reynolds number to the 0.40 power. Applying this to the subject data which has a mean value of approximately 1.5, one obtains a variation 0.2  $\sigma$ 's, in agreement with Figures 4.3a, 4.3b, 4.3c. It is the intent of this investigation to incorporate a viscous effect in terms of a Reynolds number dependency of the cavitation index into the correlation model.



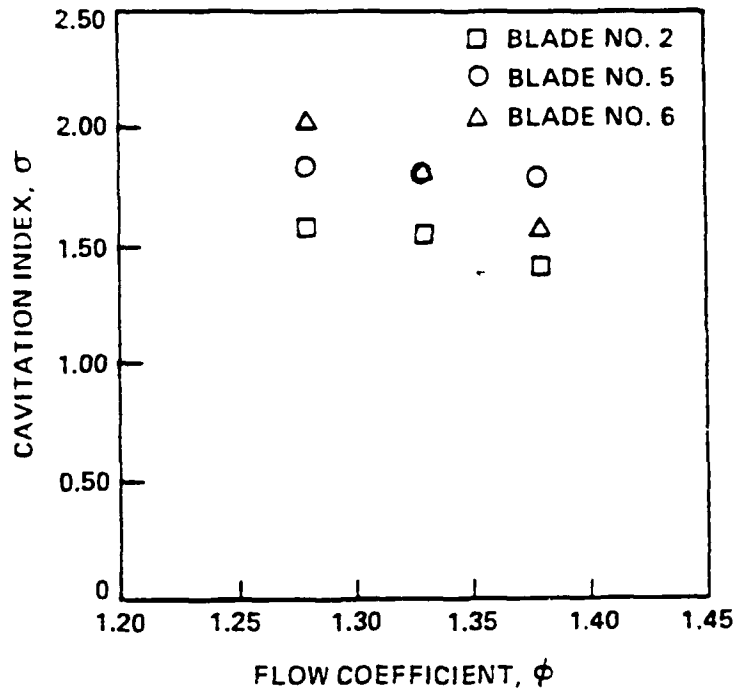
(a)



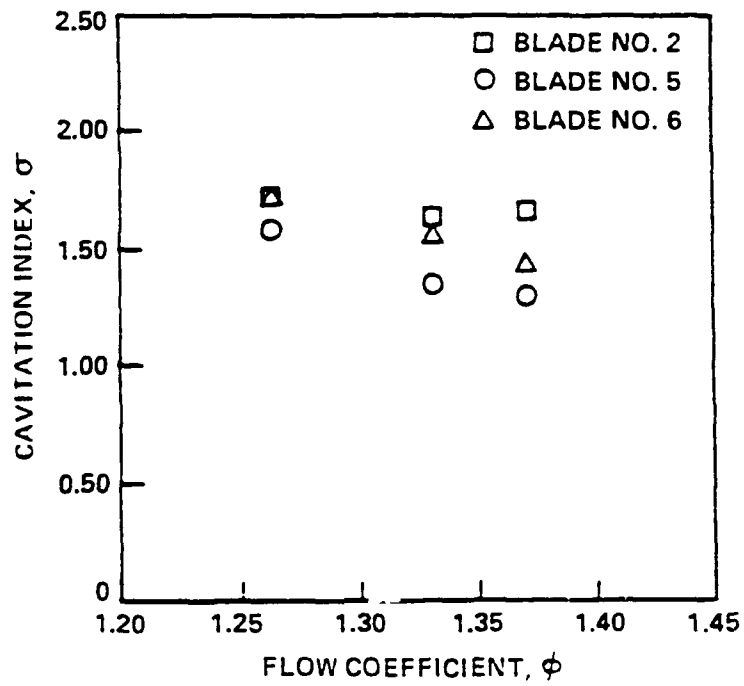
(b)

Figure 4.2. Cavitation Index versus Flow Coefficient for Dimensionless Tip Clearances of a) 0.08, b) 0.17, c) 0.35, and d) 0.55

(cont. on next page)

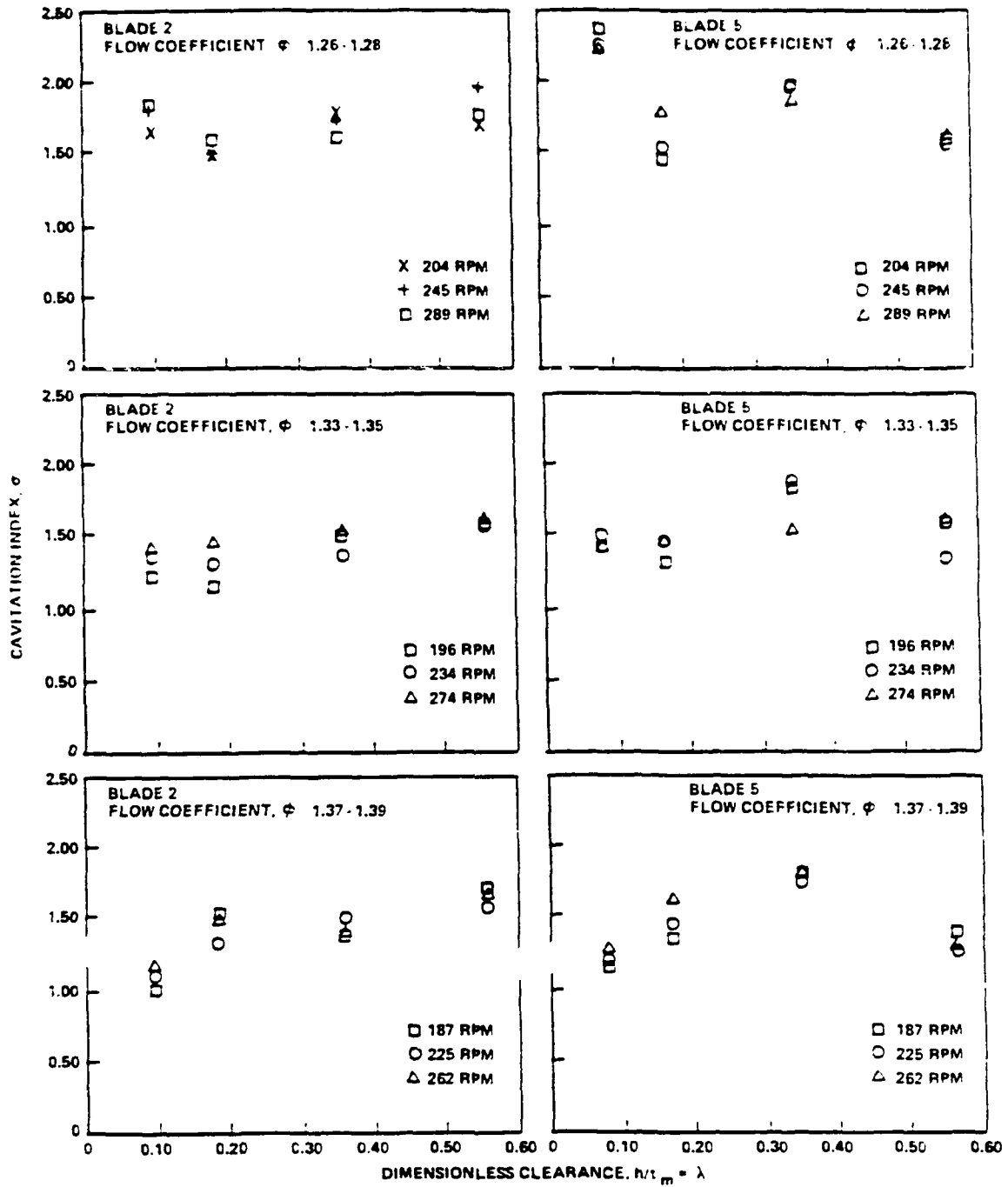


(c)



(d)

Figure 4.2 (cont.)

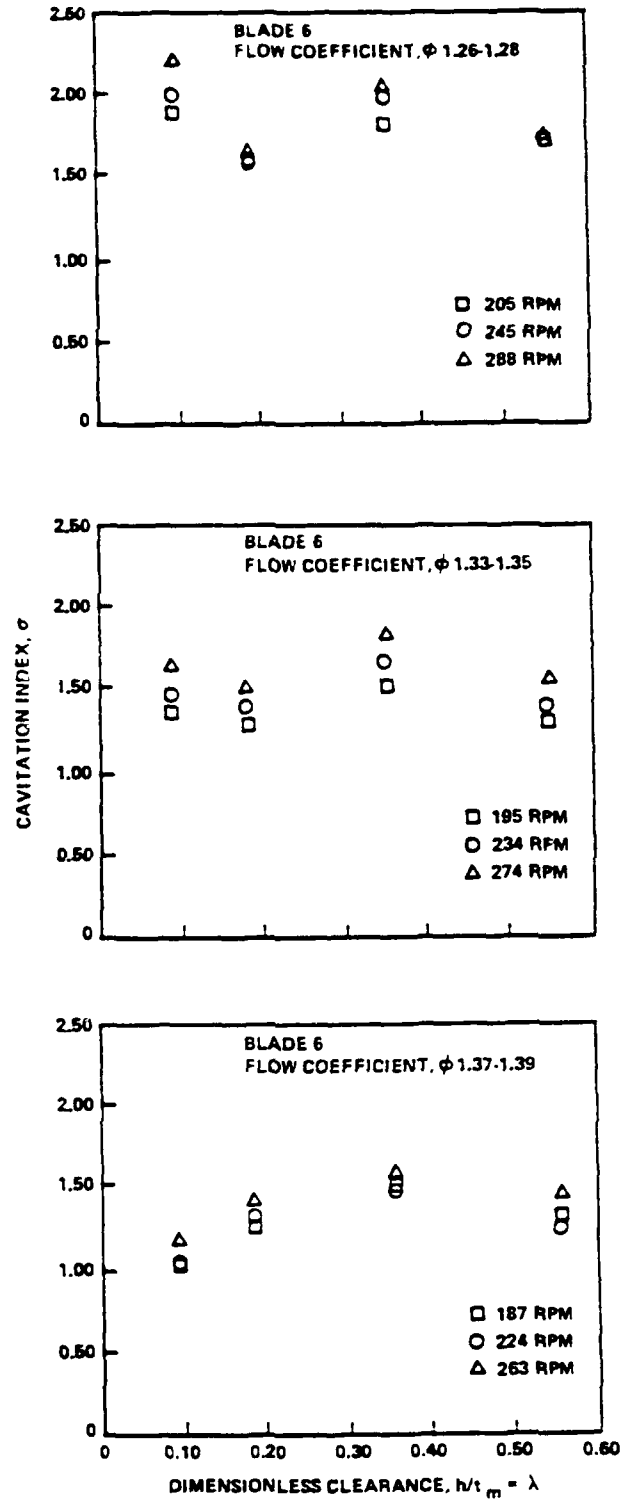


(a)

(b)

Figure 4.3. Cavitation Index versus Dimensionless Clearance for Flow Coefficient Ranges of 1.26 - 1.28, 1.33 - 1.35, and 1.37 - 1.39 for a) Blade Number 2, b) Blade Number 5, and c) Blade Number 6

(cont. on next page)



(c)

Figure 4.3 (cont.)

## 4.2 Force Measurements

### 4.2.1 Tip Lift Measurements

The lift on the top 10 percent of the rotor blade span was measured as a function of flow coefficient, axial velocity, and tip clearance. Figure 4.4 illustrates the relationship between the tip lift coefficient and the flow coefficient for four values of tip clearance. The curves in Figure 4.4 illustrate a second order polynomial curve fit applied to the data. However, the tip lift coefficient is nearly a linear function of the flow coefficient for the tip clearances tested. The tip lift decreases with flow coefficient because the blade is operating at a higher angle of attack for lower flow coefficients.

A cross plot generated from the data of Figure 4.4 is illustrated in Figure 4.5 for a flow coefficient of 1.33, the nominal operating point of the HIREP facility. The tip lift coefficient decreases asymptotically from its maximum value at zero clearance to a value representative of the open propeller condition. In Figure 4.6, the retained lift ratio,  $K$ , is plotted as a function of the dimensionless tip clearance  $\lambda$ . The subject experimental data agreed very well with the empirical correlation of Lewis and Yeung [35], while Lakshminarayana's cascade data over-predicted the retained lift ratio for most clearances. The data of Figure 4.6 determines one of the sub-models needed for the analytical model of end-wall vortex cavitation. The relationship of the tip lift with the tip clearance

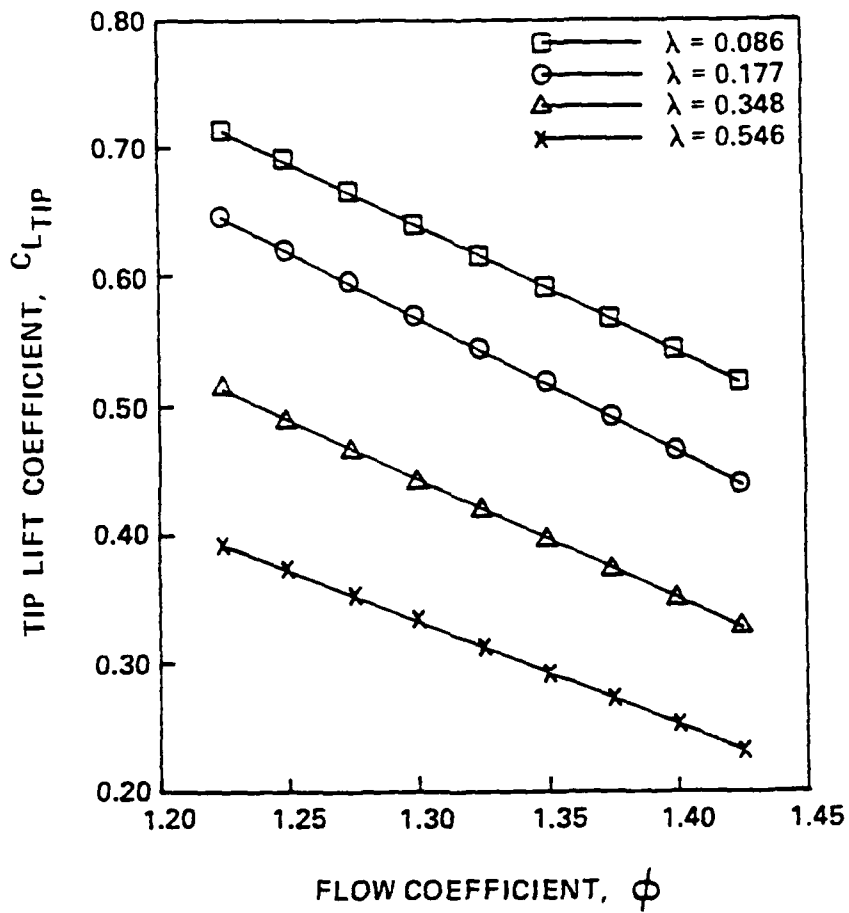


Figure 4.4. Tip Lift Coefficient versus Flow Coefficient for Four Values of Dimensionless Tip Clearance

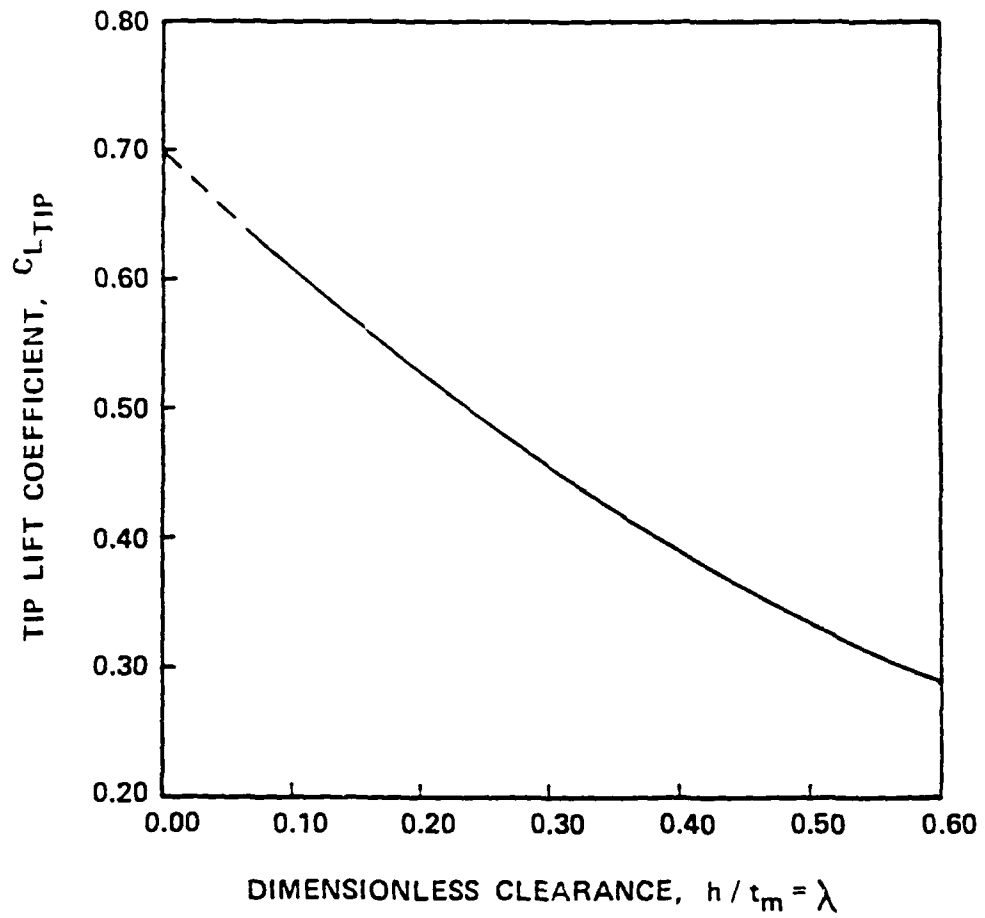


Figure 4.5. Tip Lift Coefficient versus Dimensionless Tip Clearance for a Flow Coefficient of 1.33

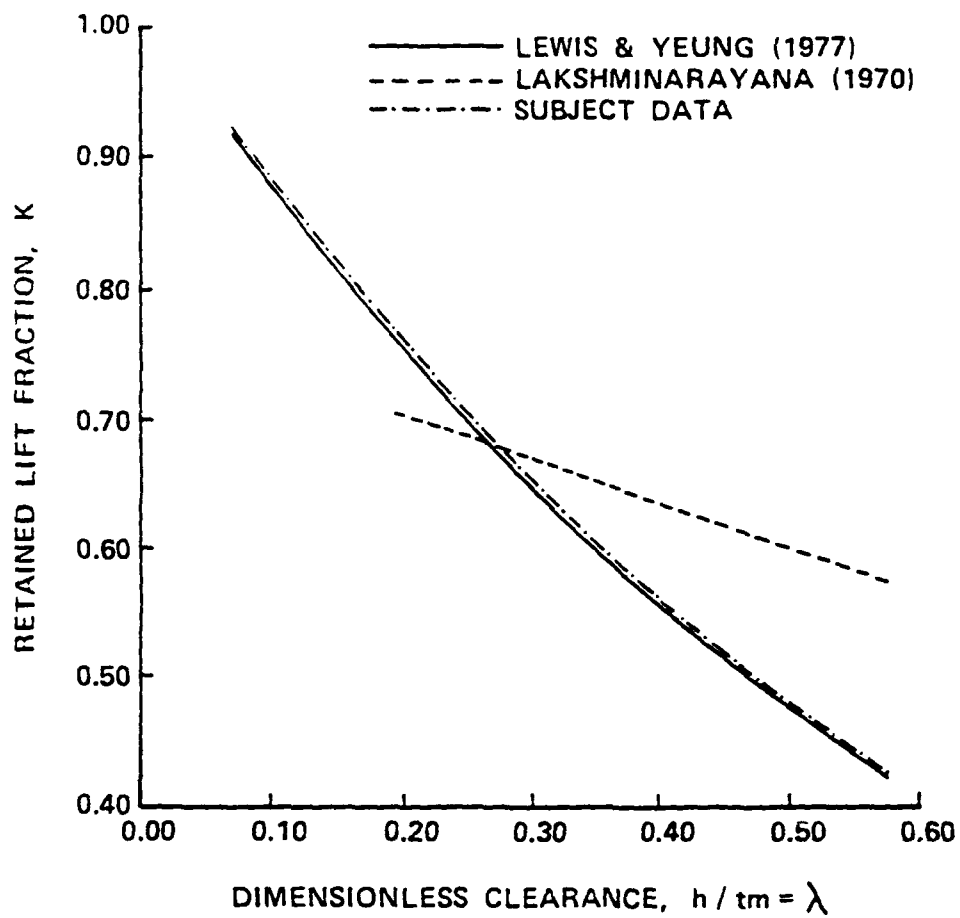


Figure 4.6. Retained Lift Ratio versus Tip Clearance for Lewis and Yeung [35], Lakshminarayana [34], and the Subject Data

was given in Section 2.5 as

$$K = \exp(-14 h/c) \quad (2.2)$$

#### 4.2.2 Blade Force Measurements

The measurements of total blade lift show that the lift produced by the top 10 percent of the blade span represents only a small fraction of the total lift on the blade. In order to compare similar forces, the ratios of the tangential tip and total blade forces for several tip clearances are illustrated in Figure 4.7 as a function of flow coefficient. The tangential component was used rather than the lift force itself for two reasons: 1) the direction of the lift changes as a function of the spanwise position, and 2) the tangential force is that which does work on the fluid. The measurements substantiated the initial assumption that a force transducer was required for the rotor tip only, since it would be difficult to resolve the small variation of lift with tip clearance on the force transducers measuring the total blade force. In order to define a lift coefficient, the component of total blade force normal to the chord at the 0.7 radius position was used. The experimental lift coefficient is illustrated in Figure 4.8 as a function of flow coefficient.

#### 4.3 Blade Static Pressure Measurements

Blade static pressures were measured five positions in the tip region: 10-percent chord, pressure side; 50-percent chord, pressure side; 40-percent chord, suction side; mid-chord, tip

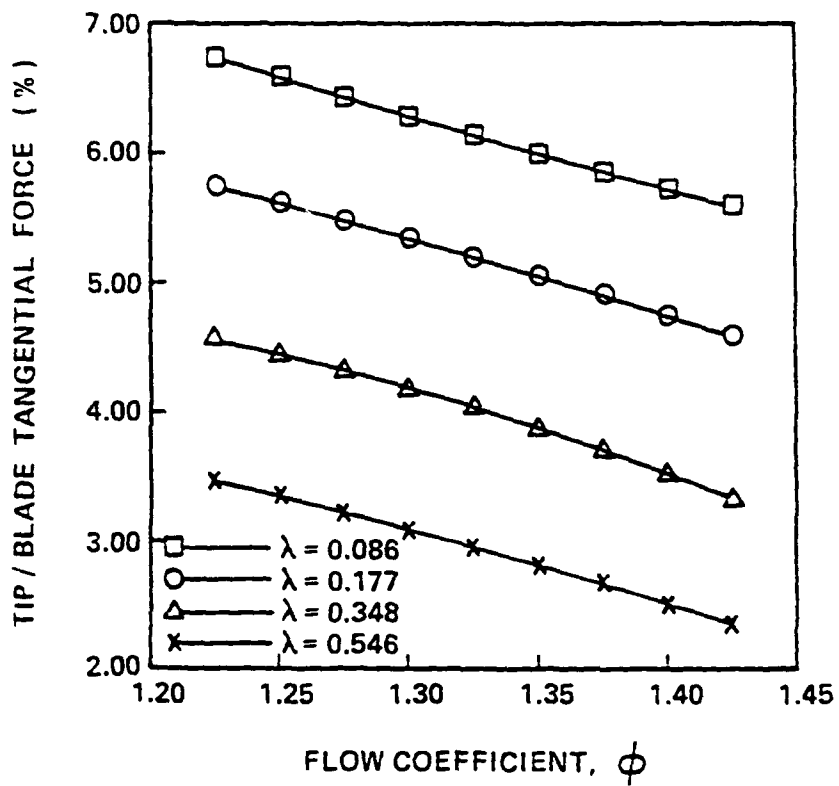


Figure 4.7. Percentage of Tangential Force at Rotor Tip versus Flow Coefficient for Four Values of Dimensionless Tip Clearance

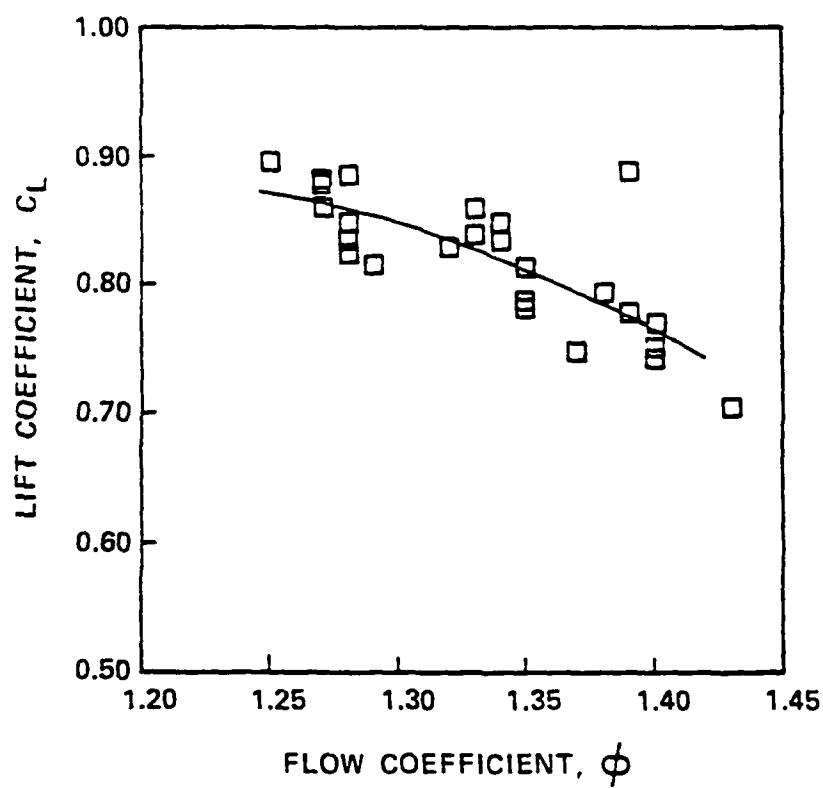


Figure 4.8. Lift Coefficient versus Flow Coefficient

surface; and the liner surface opposite the tip transducer. The measurements of pressure represent integrated values, and thus are steady-state.

The design of the HIREP rotor blade sections incorporates an elliptical loading distribution over the chord. The theoretical point of maximum loading is at the 50-percent chord. The distribution is relatively flat over the middle of the chord and tapers to zero at the leading and trailing edges. Using the 50-percent chord, pressure side transducer and the forty percent chord, suction side transducer, a pressure coefficient was calculated. This pressure coefficient is defined as

$$C_P = \frac{P_{p50} - P_{s40}}{\frac{1}{2} \rho U^2} \quad (4.5)$$

This pressure coefficient, which represents a local lift coefficient at the mid-chord position, was obtained by subtracting the values of the transducers nearest the mid-chord region. The relative position of the two transducers, one on the suction face, the other on the pressure face, is tolerable since the elliptical loading distribution is nearly flat at this position. The pressure coefficient was determined as a function of flow coefficient for several values of axial velocity and tip clearance. The results are given in Figure 4.9. The highest values for each tip clearance represent the highest velocities measured. Using interpolated values of the pressure coefficient for a flow coefficient of 1.33 at the highest axial velocity of 36 ft/s, a value of the retained lift ratio was determined as in section 4.2.1 for the three tip clearances tested.

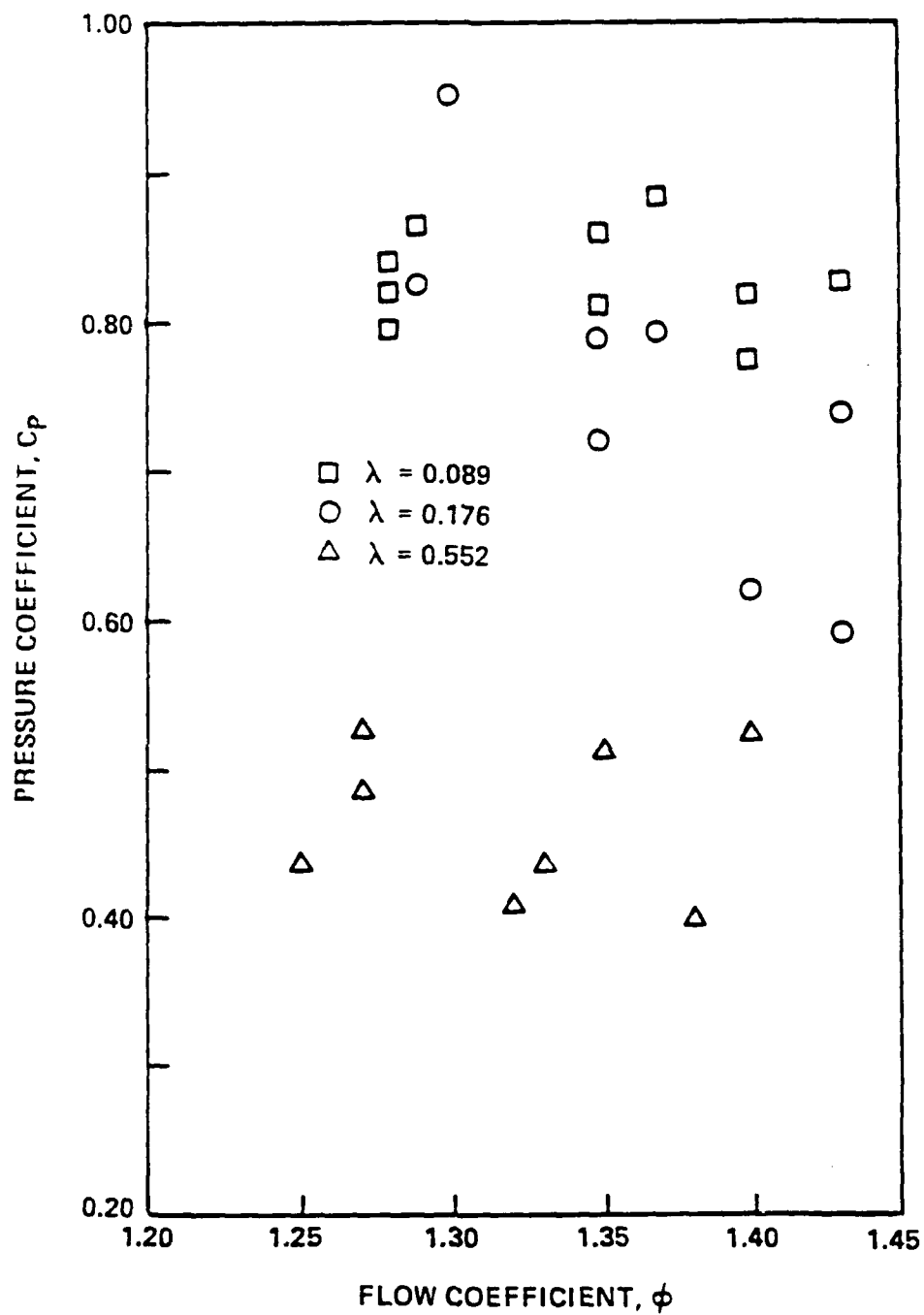


Figure 4.9. Pressure Coefficient,  $C_p$ , versus Flow Coefficient for Three Values of Dimensionless Tip Clearance

These values compare very reasonably with the tip force measurements as shown in Figure 4.10. The pressure coefficient values are higher than the tip lift coefficient values since a direct comparison assumes a uniform pressure distribution over the chord when in fact it is elliptical.

A second pressure coefficient was defined using the transducers on the rotor tip surface and the liner duct surface. Again, as above, the voltages from the transducers were integrated and thus provide steady-state values of the pressures. A time history of the liner pressure would be modulated by the rate of blade passage. The coefficient is defined as

$$C_{P_g} = \frac{P_{\text{tip}} - P_{\text{liner}}}{\frac{1}{2} \rho U^2} \quad (4.6)$$

The pressure coefficient is given in Figure 4.11 as a function of flow coefficient for several values of axial velocity and tip clearance. The pressure coefficients calculated across the blade tip and from the blade tip surface to the liner have values which are the same order of magnitude. The pressure gradient from the wall to the tip surface would appear to drive the leakage flow radially inward, as was depicted in the rotor tip flow field of Figure 1.2. The effect of this pressure gradient would be minimal, however, since it travels with the blade and thus is highly localized. From a time history of the pressure, one could observe the strength and duration of the pressure pulse from the blade tip passage.

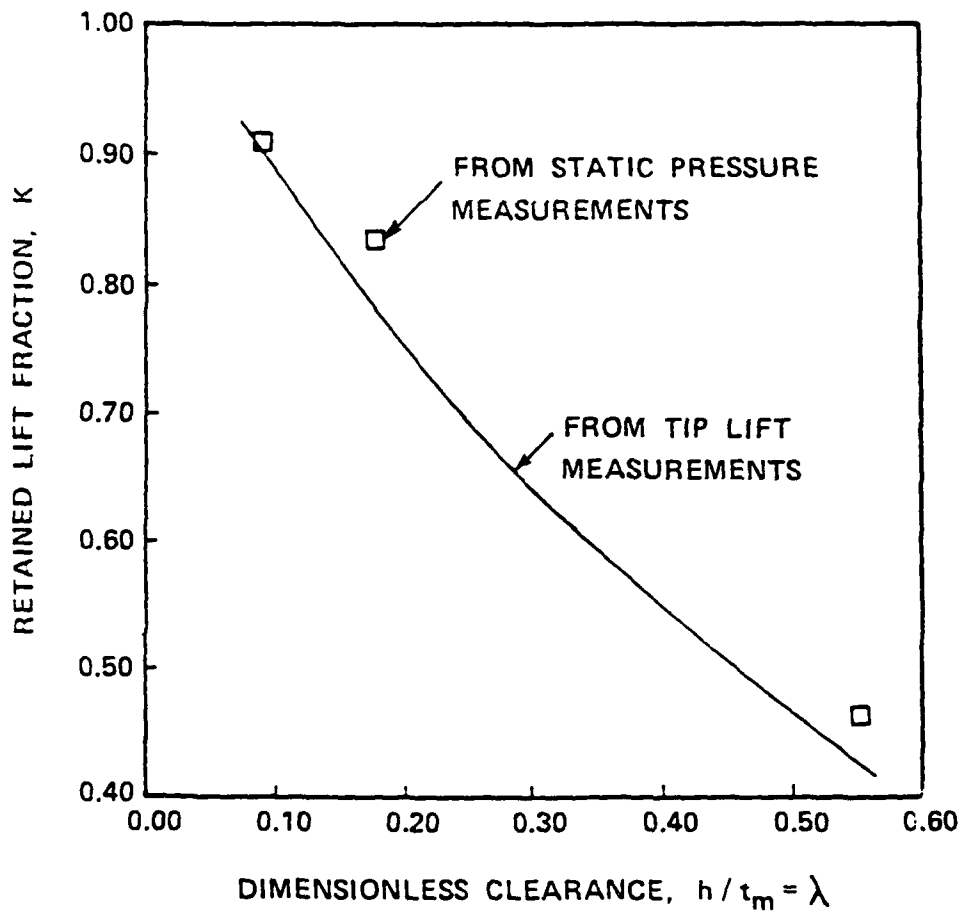


Figure 4.10. Retained Lift Fraction versus Dimensionless Tip Clearance for both Pressure and Force Measurements

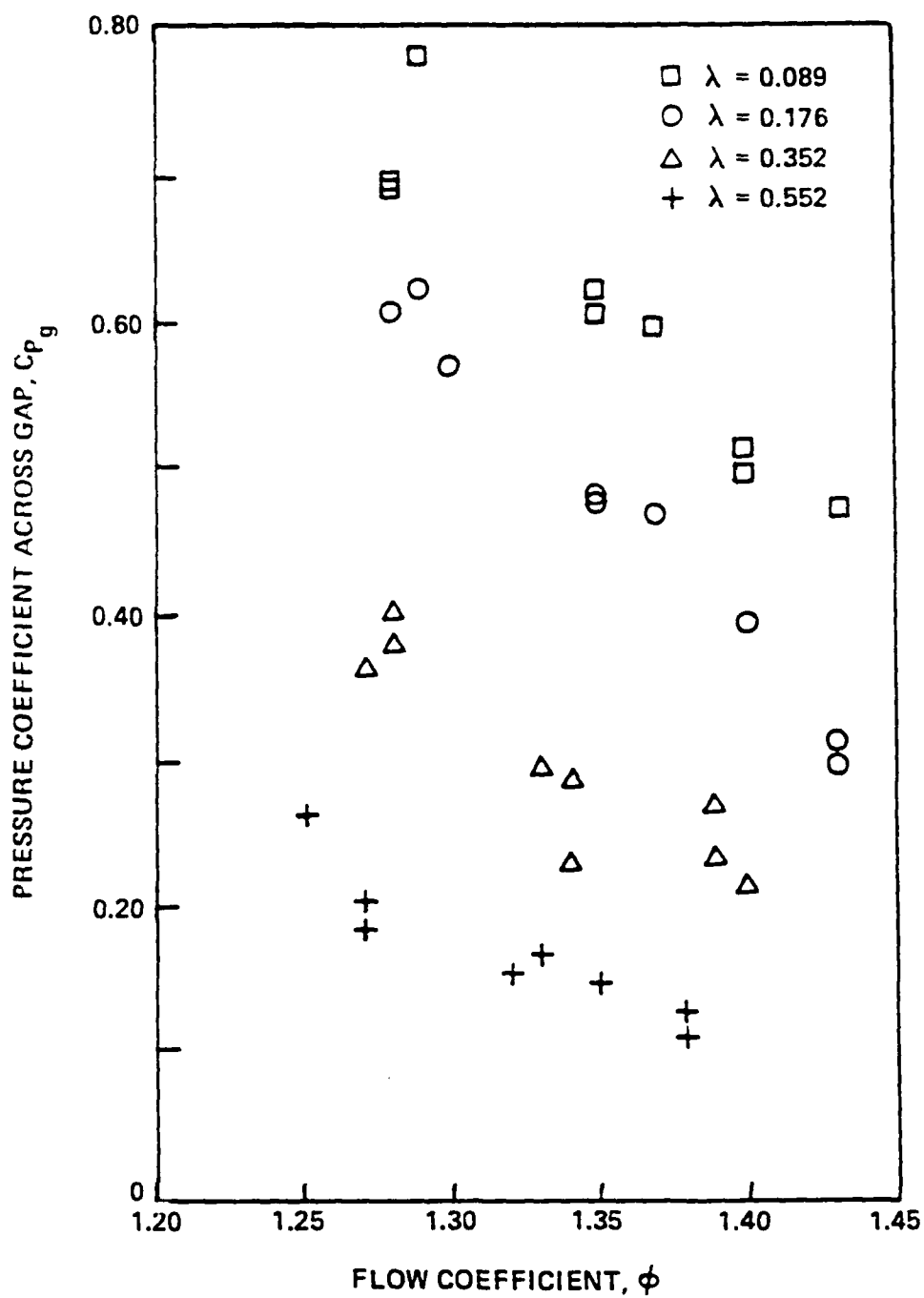


Figure 4.11. Pressure Coefficient,  $C_{p_g}$ , versus Flow Coefficient for Four Values of Dimensionless Tip Clearance

#### 4.4 Dynamic Tip Clearance Measurements

The dynamic tip clearance measurements made on the High Reynolds Number Pump show that the tip clearance does not change significantly during operation at axial velocities up to 36 ft/s. Figure 4.12 illustrates a comparison of dynamic measurements with the static measurements for seven rotor blades. The variation of tip clearance with velocity had no particular trend, and thus can be attributed to random error in the measurement. The range of values is certainly within the resolution error of the system, which is estimated to be  $\pm 0.005$  inches. If the tip clearance were changing dynamically, one would expect it to increase parabolically with rotational speed. Figure 4.12 shows that the tip clearances of some blades increase, while others decrease. Thus the variation of tip clearance with rotational speed is insignificant in this application, and thus it will not be considered in the correlation model.

#### 4.5 Velocity Surveys

##### 4.5.1 Five-hole Probe Boundary Layer Survey

A five-hole probe was traversed through three inches of the rotor tip inlet flow to determine the incoming flow field. The measured boundary layer is given in Table 4.1. Using these data and the blade stagger and camber angles, one can calculate the incidence angle as a function of flow coefficient and tip clearance for the rotor tip section. The results of this calculation for a range of flow coefficients are given in Figure 4.13. The incidence increases

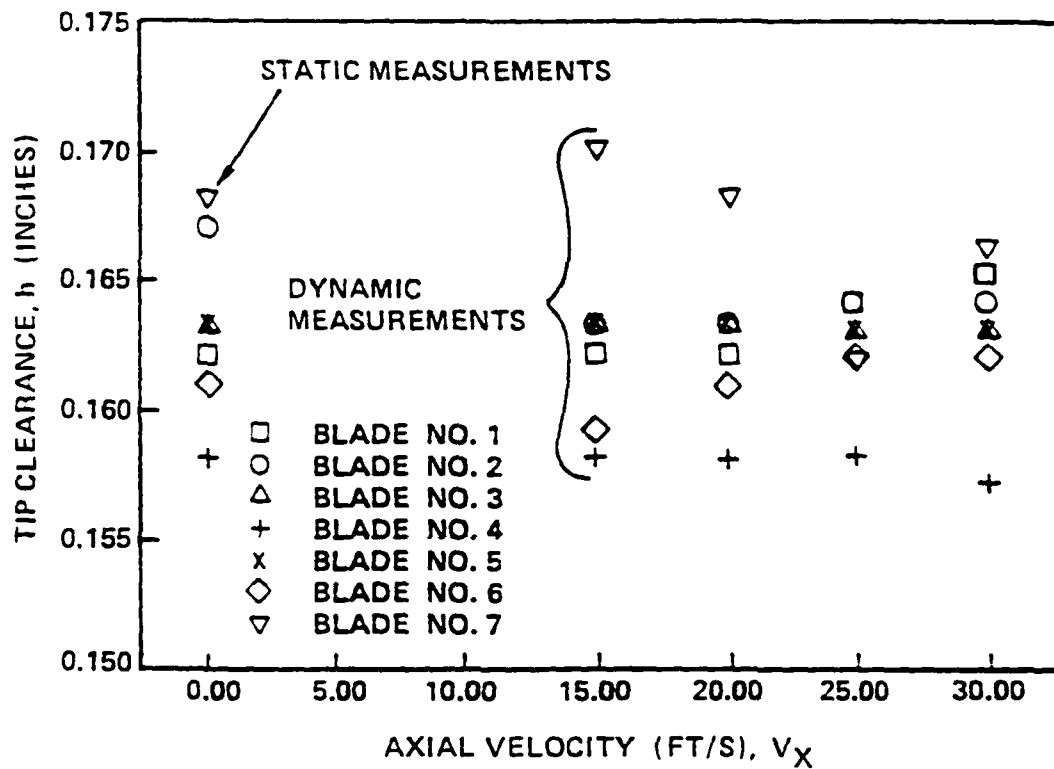


Figure 4.12. Tip Clearance versus Axial Velocity as Measured by the Variable Impedance Displacement Transducer and Compared with the Static Micrometer

TABLE 4.1

Five-hole Probe Boundary Layer Survey at  $V_X = 31$  ft/s

<u>Tip Clearance</u>	<u><math>r/r_s</math></u>	<u><math>V_T/V_{ref}</math></u>	<u><math>V_X/V_{ref}</math></u>
0.10 in.	0.995	-0.032	0.379
0.20	0.990	-0.016	0.600
0.30	0.986	-0.006	0.747
0.40	0.981	-0.001	0.831
0.50	0.976	0.001	0.912
0.60	0.971	-0.006	0.957
0.70	0.967	-0.004	0.986
0.80	0.962	-0.005	0.999

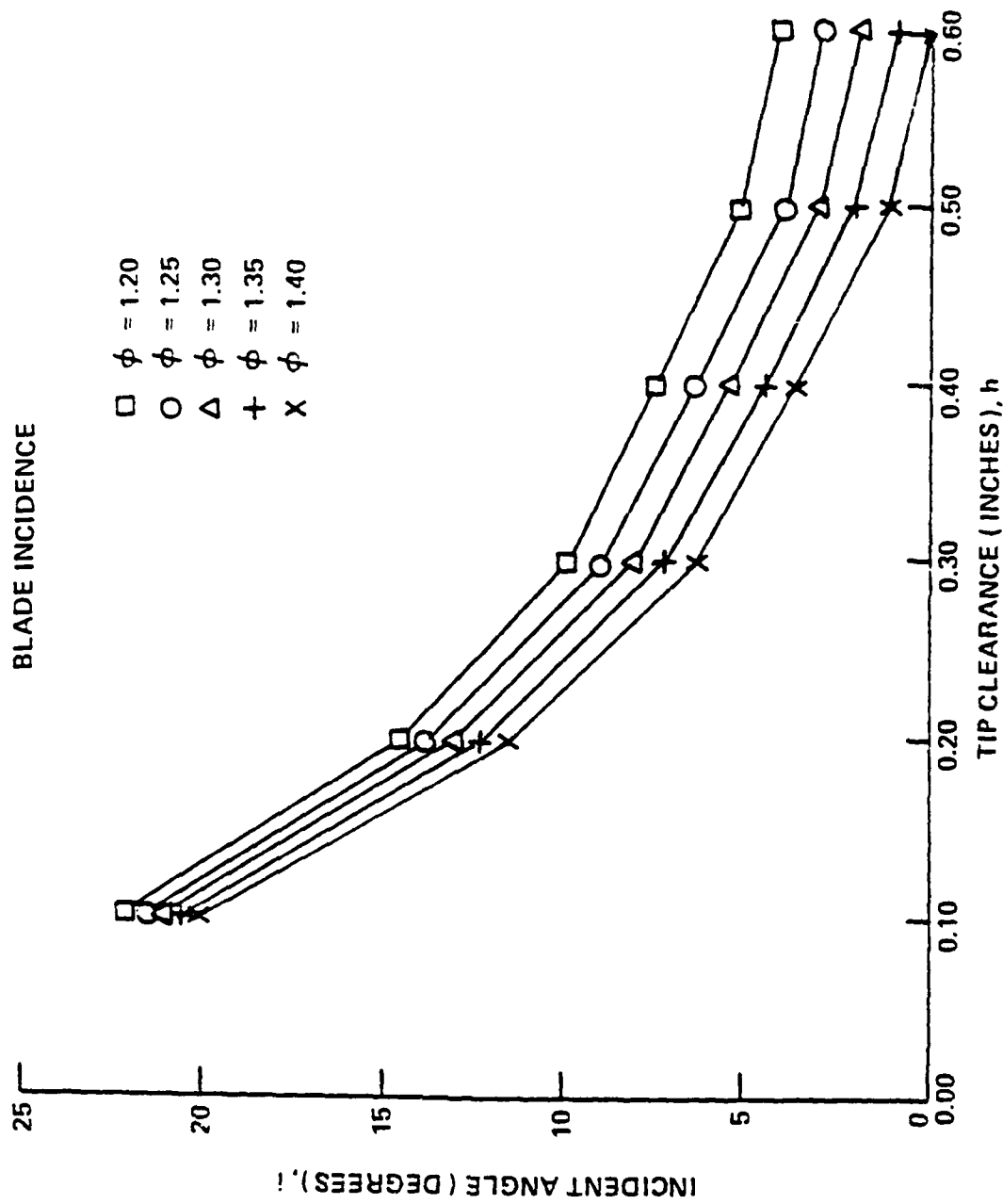


Figure 4.13. Incidence Angle versus Tip Clearance for Several Ranges of Flow Coefficient

rapidly from approximately five degrees at  $\lambda = 0.5$  to approximately twenty degrees at  $\lambda = 0.1$ .

The Douglas Neumann cascade program [54] was used to calculate the minimum pressure coefficient on the HIREP rotor tip section. The subject blade cross section is given in Figure 4.14. The blade contour was defined by 237 points. Several runs were made using the same input conditions and varying the number of points defining the airfoil cross section. A comparison of the output show different solutions for contour definitions having less than 119 points. The tests were then run with 237 points. The agreement between the run with 119 points and the run with 237 points is excellent.

The basic concept of the Douglass Neumann cascade program is to specify a distribution of sources on the surface of the blades such that the combination of the source distribution and the onset flow satisfies the boundary condition on the blade surface of no flow normal to the surface. The code is inviscid, and thus there are no considerations of separation. Pressure distributions were calculated for the airfoil cross section of Figure 4.14 at several angles of attack: 0, 2, 5, 10, 15, 20, and 25 degrees. As observed from Figure 4.15, the minimum pressure coefficient, although correct mathematically, surpasses a physically realizable value, indicating separation and stall at about five degrees of incidence.

#### 4.5.2 Laser Velocimeter Surveys

The laser velocimeter was also used to measure the rotor tip inlet, exit, and gap flows. Measurements were made 3.5 inches

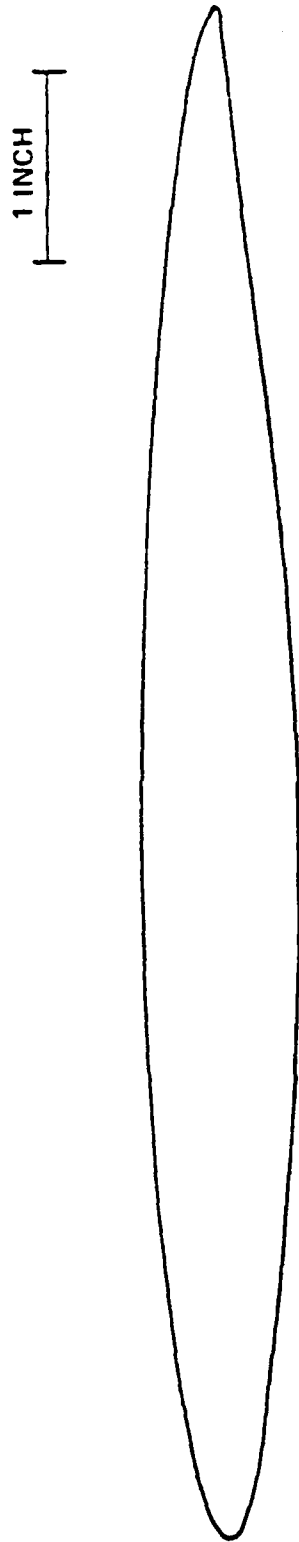


Figure 4.14. Unwrapped Cylindrical Cross-section of the Rotor Tip

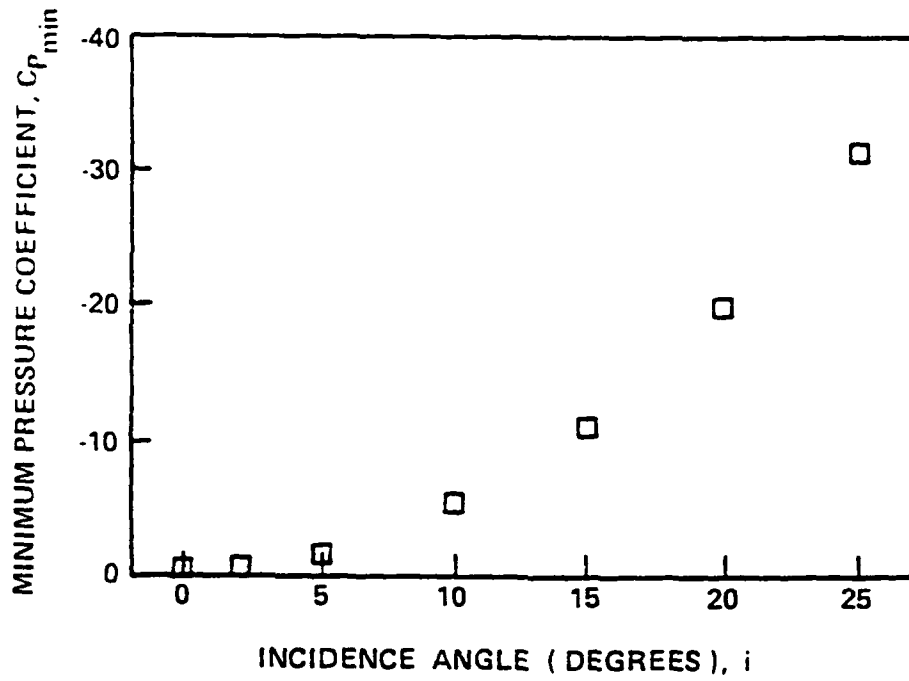


Figure 4.15. Minimum Pressure Coefficient versus Angle of Attack from Douglas Neumann Program

upstream of the rotor tip leading edge and 2.75 inches downstream of the rotor tip trailing edge. Figures 4.16 and 4.17 illustrate the end-wall boundary layer profiles measured at axial velocities of 26 and 31 ft/s, respectively. The latter figure also illustrates a five-hole probe velocity survey taken simultaneously at a different angular location. The data agree quite well. Figures 4.18 and 4.19 illustrate the end-wall boundary layer profiles at the exit of the rotor tip for axial velocities of 26 and 31 ft/s, respectively. The displacement thickness, momentum thickness, and shape factor were calculated for the velocity surveys measured with a five-hole probe and the laser velocimeter. These integral properties are summarized in Table 4.2. The calculations were performed using a quadrature procedure on the cubic spline formed from the data points and the no-slip boundary condition. The boundary layer thickness entering the rotor is approximately 0.8 inches. The boundary layer thickness at the rotor exit is approximately 2.2 inches.

The velocity profile in the tip clearance space was measured at two locations using the laser velocimeter. These locations correspond to 44 percent and 74 percent of the axial projected chord. In general, a plot of either the axial or tangential velocity versus rotor angular position forms an inverted bell shape. The minima of the curves was used to represent the velocity in the tip clearance when the rotor-tip surface was directly adjacent to the measurement control volume. The velocity profile obtained in a rotor tip clearance of  $\lambda = 0.54$  is given in Figure 4.20 with the two no-slip boundary conditions. The downstream 74 percent chord position showed

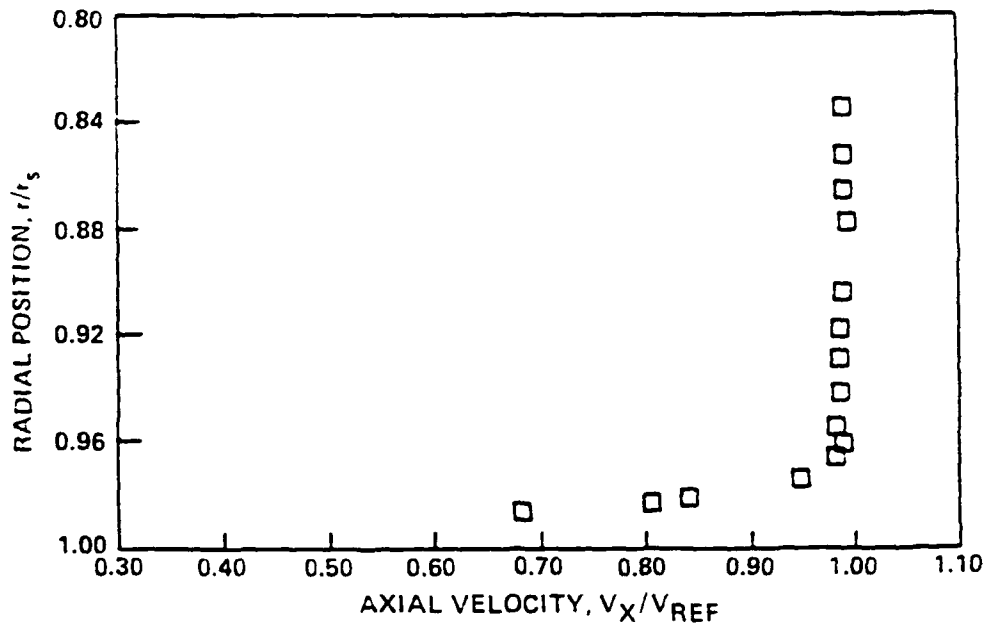


Figure 4.16. Rotor Inlet Boundary Layer Profile at  $V_x=26$  ft/s and  $Re_c=1.6 \times 10^6$ , Measured with Laser Velocimeter

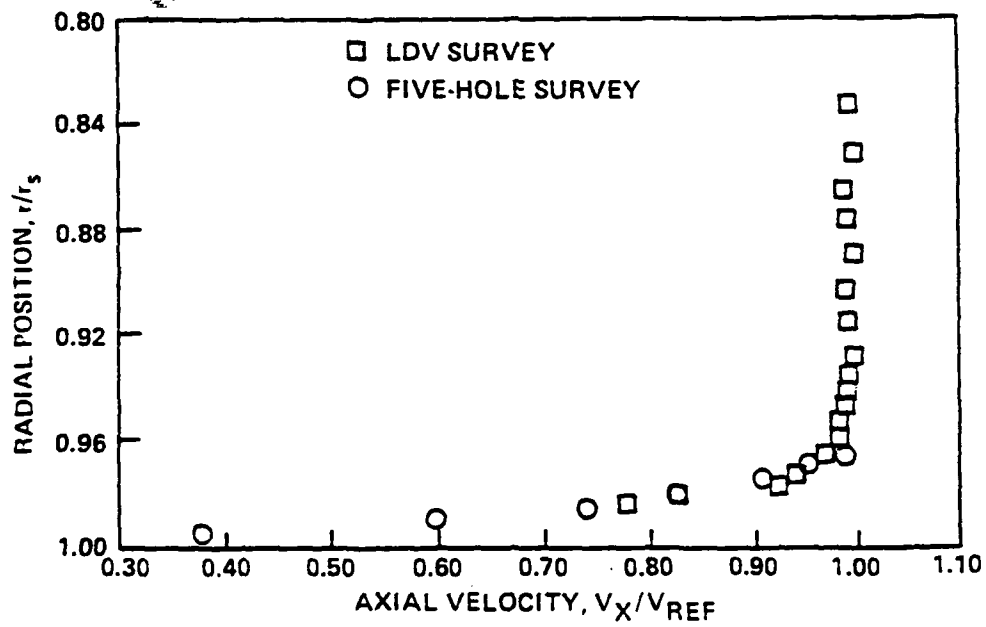


Figure 4.17. Rotor Inlet Boundary Layer Profile at  $V_x=31$  ft/s and  $Re_c=1.9 \times 10^6$ , Measured with Laser Velocimeter and Five-hole Probe

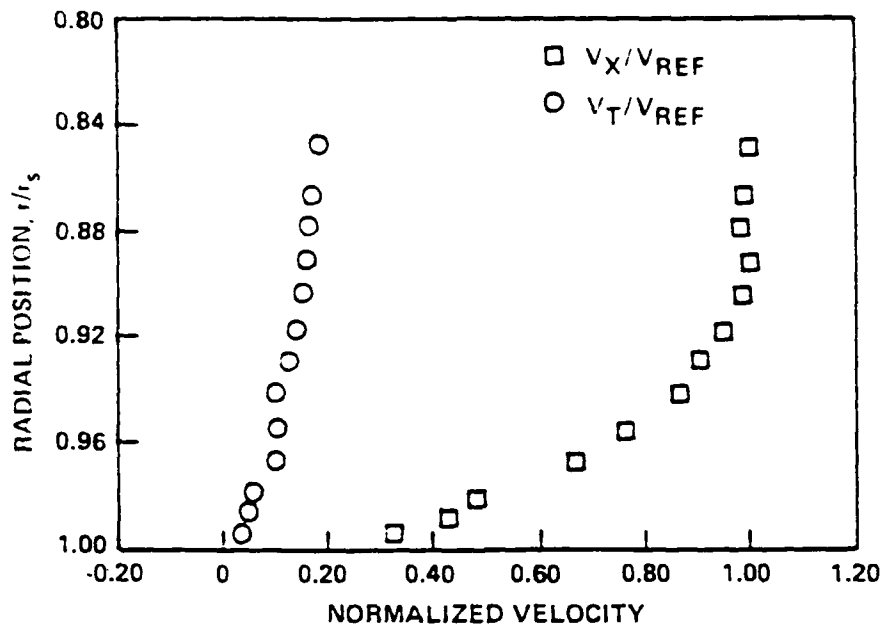


Figure 4.18. Rotor Exit Boundary Layer Profile at  $V_x=26$  ft/s and  $Re_c=1.6 \times 10^6$ , Measured with Laser Velocimeter

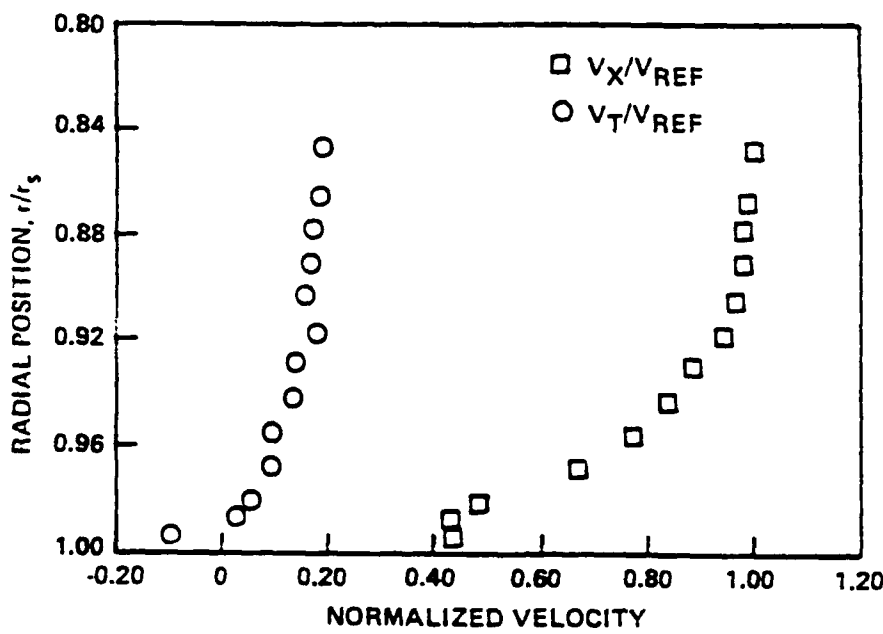


Figure 4.19. Rotor Exit Boundary Layer Profile at  $V_x=31$  ft/s and  $Re_c=1.9 \times 10^6$ , Measured with Laser Velocimeter

TABLE 4.2

Boundary Layer Integral Properties for Various  
Laser and Five-hole Probe Surveys

<u>Location</u>	<u>Method</u>	<u>Test No.</u>	<u>V<sub>ref</sub> (ft/s)</u>	<u><math>\delta^*</math> (in)</u>	<u><math>\theta</math> (in)</u>	<u>H</u>
rotor exit	5-hole probe	14866	31.0	0.567	0.326	1.74
rotor exit	5-hole probe	14867	26.0	0.572	0.325	1.76
rotor inlet	5-hole probe	14870	31.0	0.225	0.097	2.31
rotor inlet	LV	14866	31.0	0.184	0.090	2.05
rotor exit	LV	14866	31.0	0.525	0.299	1.76
rotor inlet	LV	14867	26.0	0.204	0.090	2.27
rotor exit	LV	14867	26.0	0.546	0.291	1.88

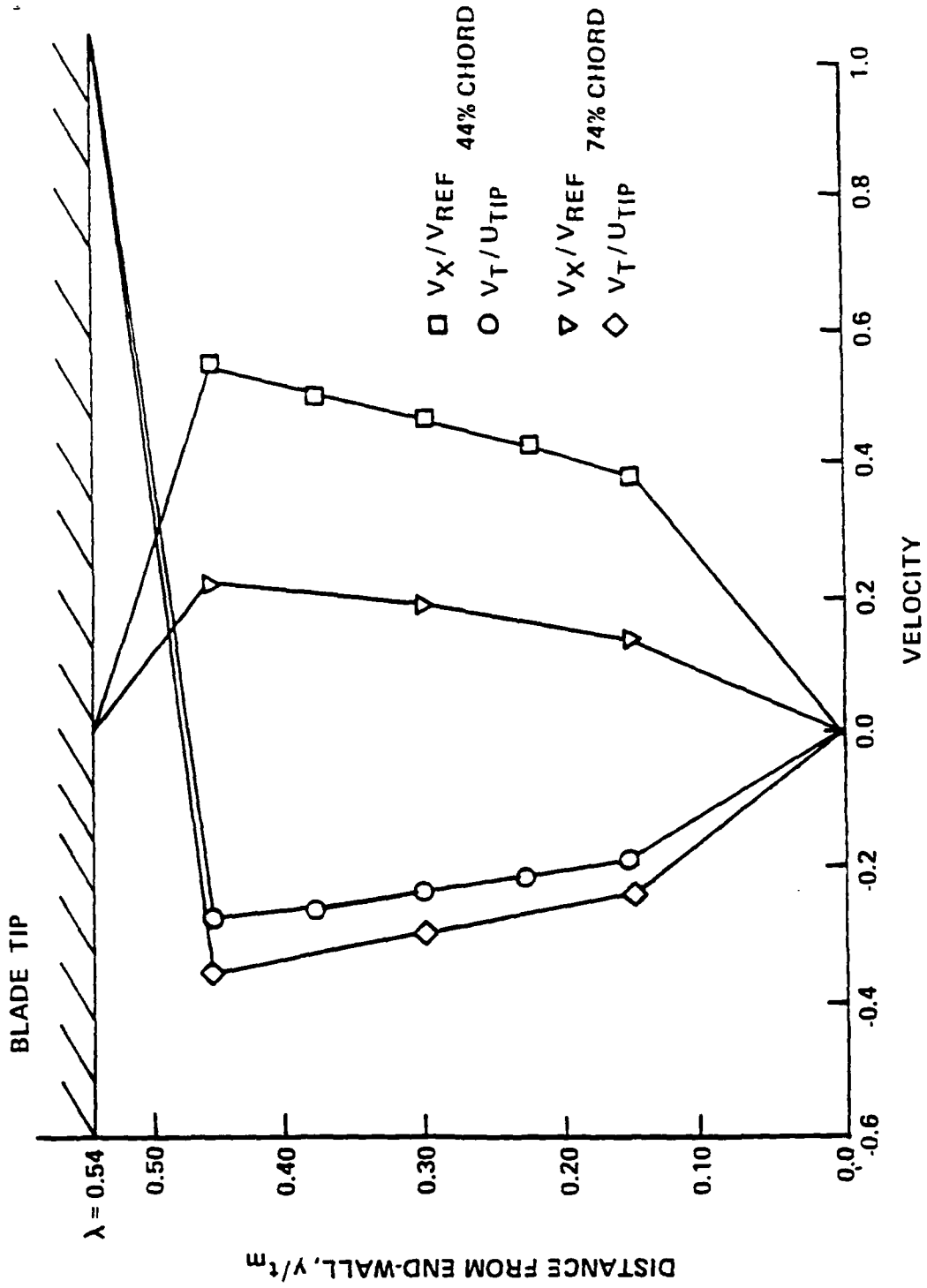


Figure 4.20. Velocity Profile for Dimensionless Clearance of 0.54

increased tangential velocity, but reduced axial velocity. Overall the fluid at the downstream position showed lower energy, Figure 4.21, as one would expect on an elliptically loaded blade. Figure 4.22 illustrates a velocity profile for a rotor blade with  $\lambda = 0.33$ . The corresponding energy profile is given in Figure 4.23. The magnitude of the maximum velocity in both the 0.476 inch and 0.286 inch tip clearances was approximately the same indicating that the momentum of the leakage flow is more dependent on the gap size than the pressure difference across the blade tip in this range of tip clearances. Thus the mass flow through the tip clearance appears to be proportional to the size of the tip clearance gap.

The laser velocimeter was also used to measure the structure of the leakage end-wall vortex at two locations downstream of the rotor trailing edge. The axial and tangential components of the velocity, relative to the shaft centerline were recorded. The end-wall vortices form a helix pattern as they move downstream. The included angle between the vortex and the blade chord varies as the loading on the rotor tip changes. In order to generate a tangential velocity distribution with respect to the axis of rotation of the vortex, the two-component data were rotated through an angle which maximized the tangential velocity and minimized the magnitude of the axial velocity. At a large distance from the vortex, the perturbation on the main through flow should be near zero.

A graphical interpretation of the data from computer generated plots required a simple coordinate transformation. In order to view

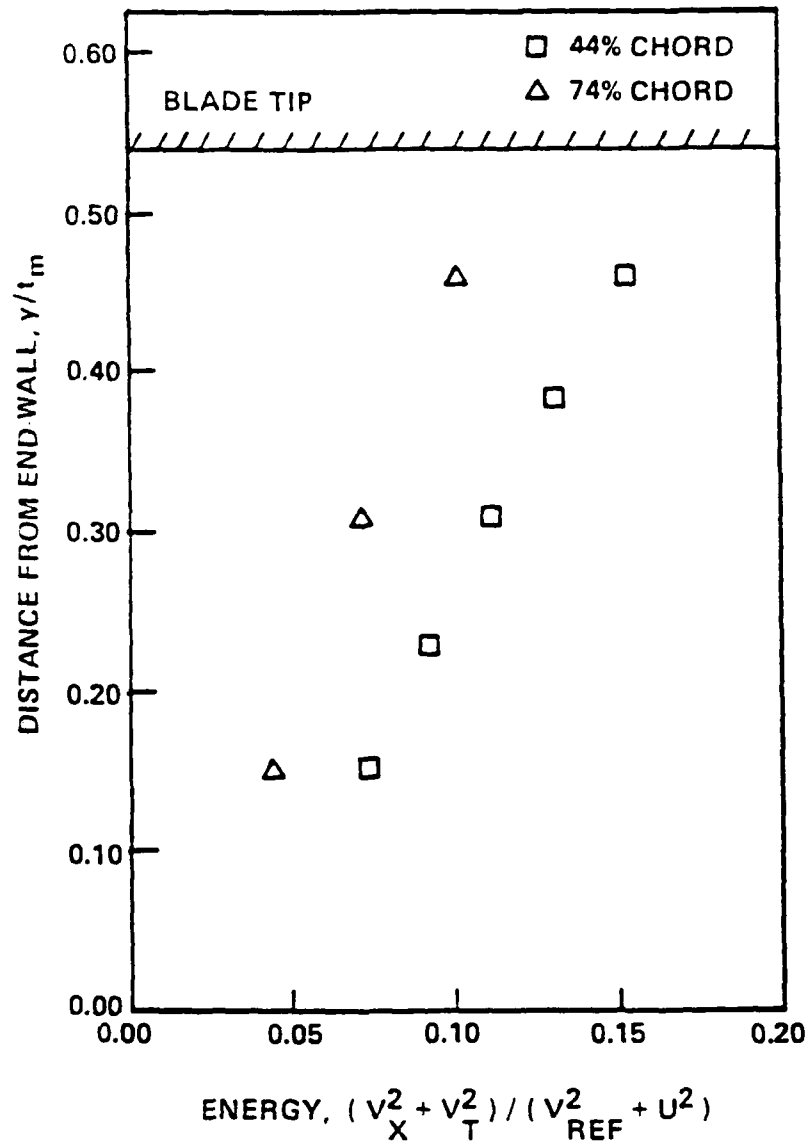


Figure 4.21. Energy Profile for Dimensionless Clearance of 0.54

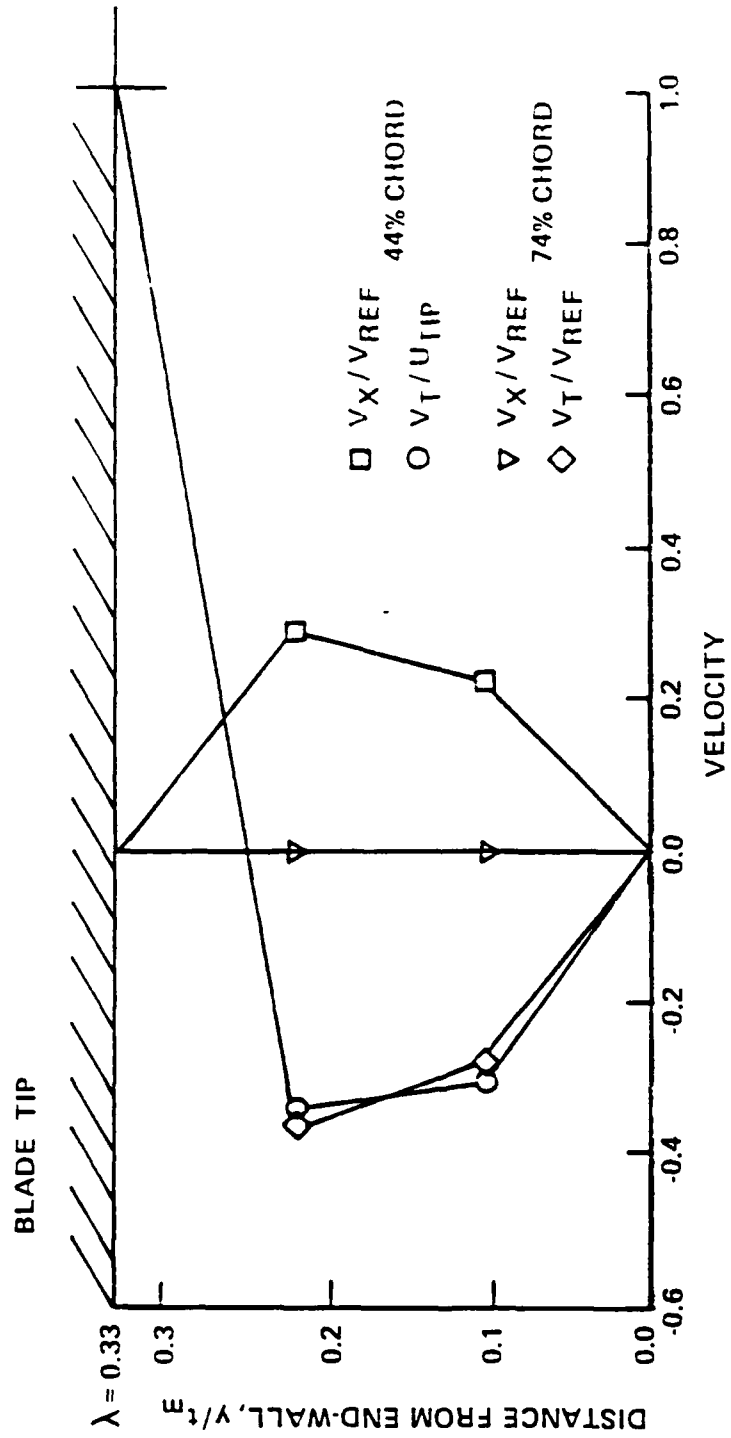


Figure 4.22. Velocity Profile for Dimensionless Clearance of 0.33

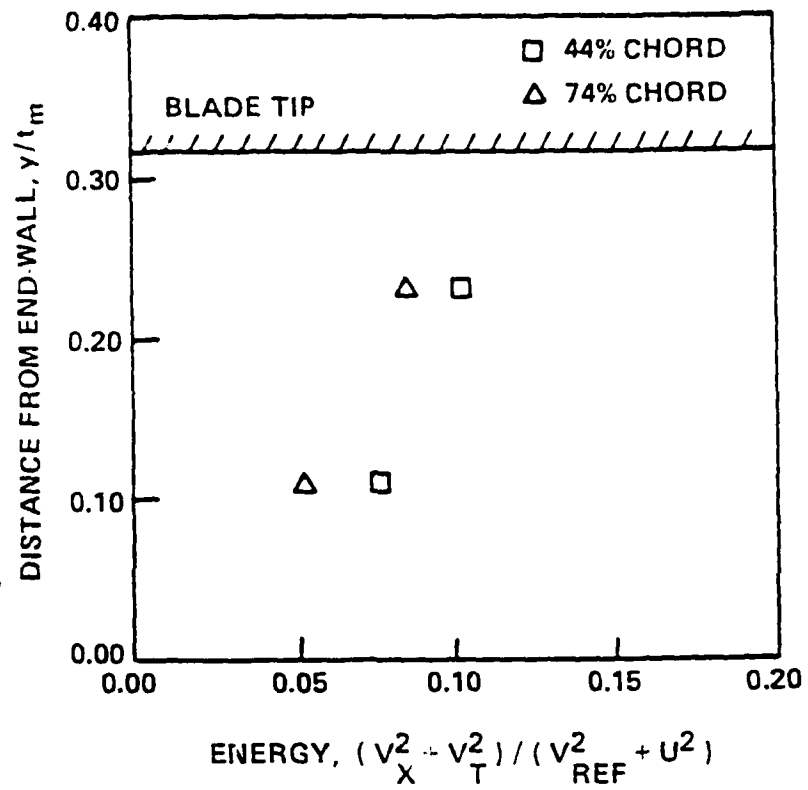


Figure 4.23. Energy Profile for Dimensionless Clearance of 0.33

the flow field in this manner, the axial velocity was transformed to a radial velocity. A sample survey is illustrated in Figure 4.24. Before transforming the data to the vortex coordinate system, the mean values of the flow field at each position were subtracted out to isolate the perturbation on the flow field caused by the leakage flow and the end-wall vortex. Figure 4.25 illustrates the relationship of the global and vortex coordinate system.

For each distance from the end-wall, the location of maximum tangential velocity was obviously the location of the end-wall vortex, exclusive of the blade wake. By tracing this angular position radially inward, one is able to generate the vortex tangential velocity distribution. For the smaller tip clearances, a tangential velocity distribution was obtained for several angular locations. Also, during the cavitation tests, the vortex was observed to move in the circumferential direction. An examination of the data show a region of high turbulence intensity over a region which is several times the apparent core size. From the above, one can conclude that the vortex is wandering significantly in the circumferential direction and is probably elliptical in shape with the major axis lying in the circumferential direction. By applying the technique of Baker et al. [55], which is a double integration of the instantaneous velocity distribution with a joint Gaussian probability distribution, it was found that the vortex would be smeared out to the extent that it would barely be observable. However, the measured tangential velocity distribution is easily identified as a Rankine type vortex, and therefore one can conclude that the vortex structure

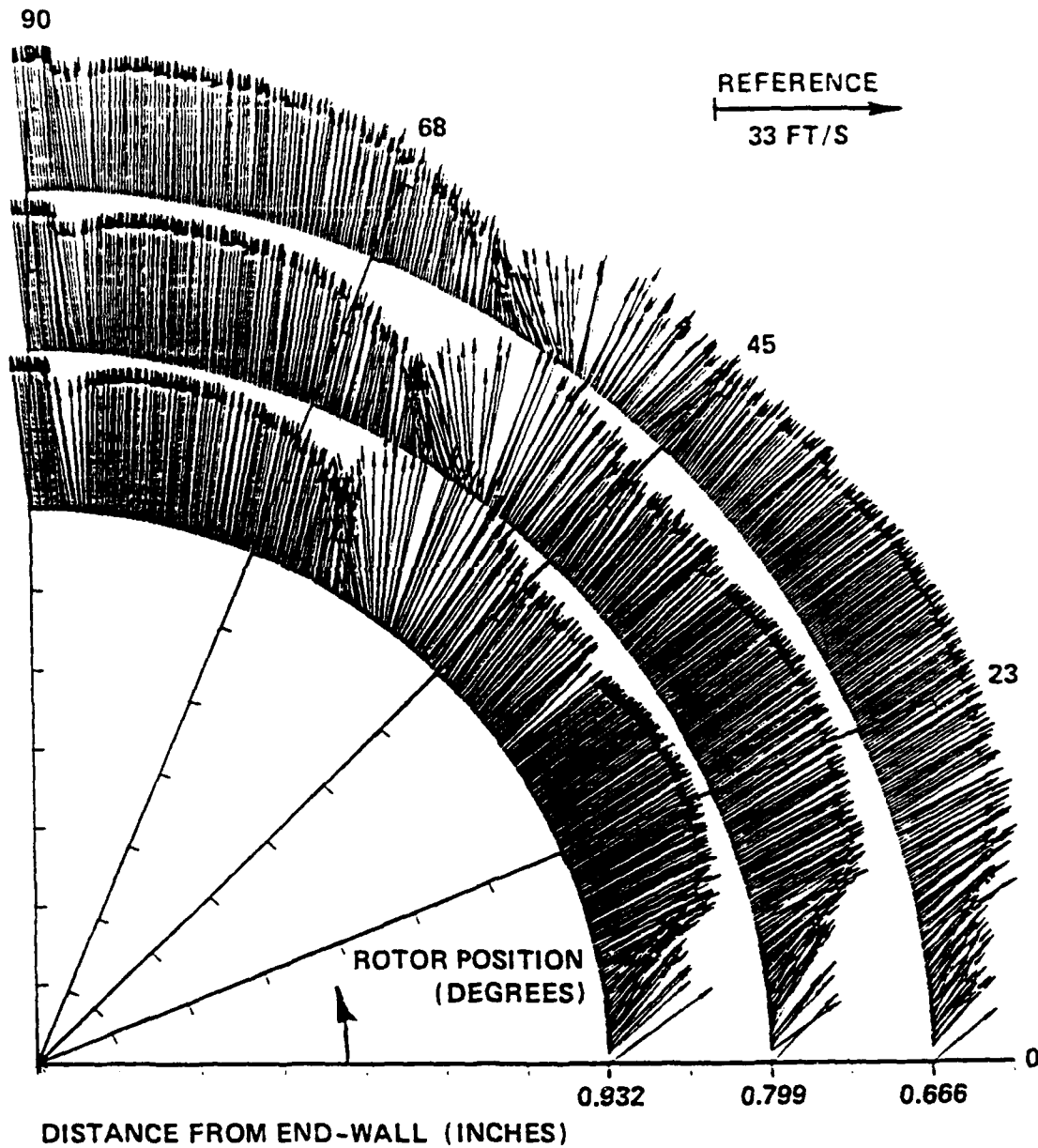


Figure 4.24. Sample Laser Velocimetry Survey of End-wall Vortex

(cont. on next page)

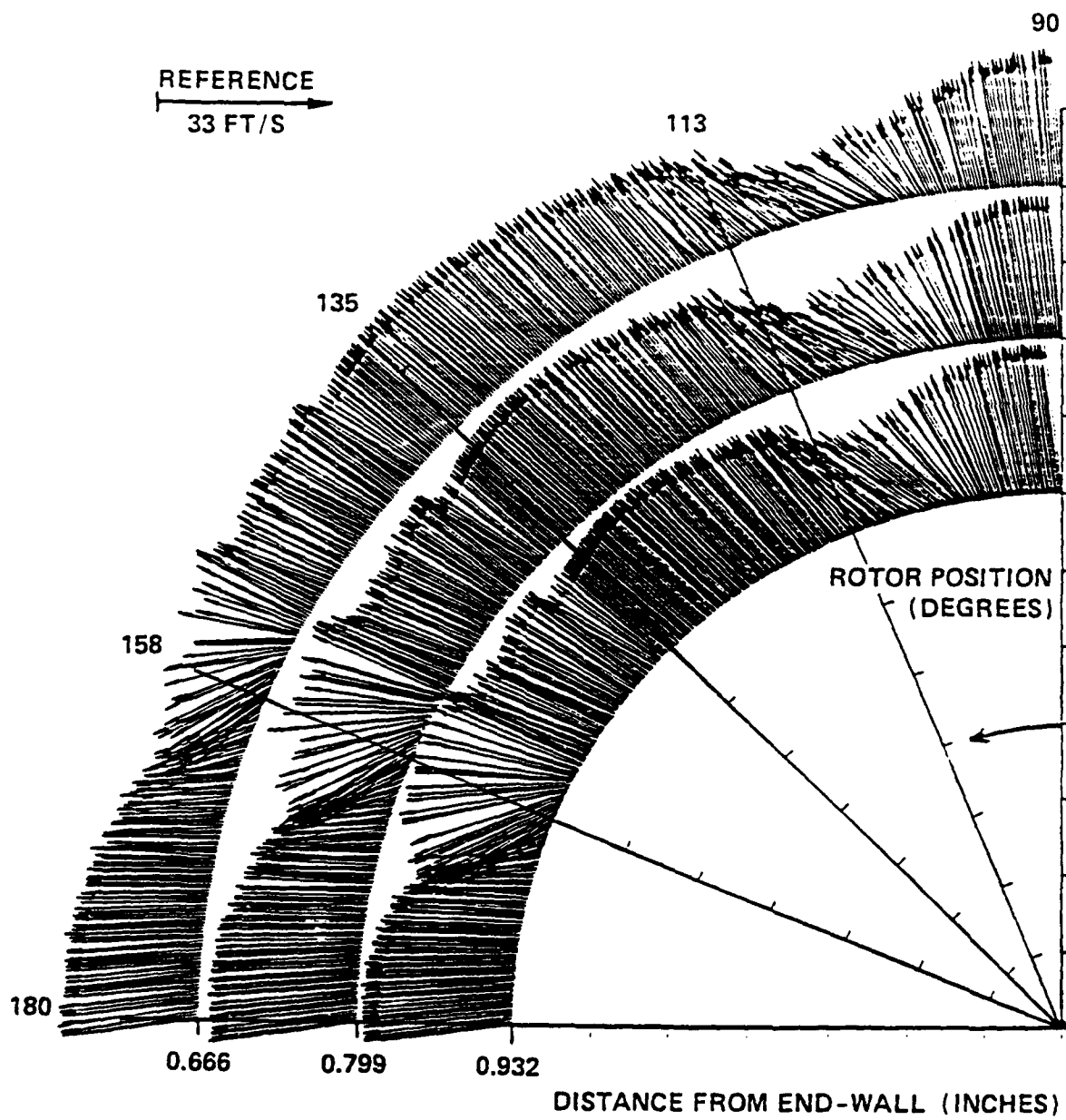


Figure 4.24 (cont.)

(cont. on next page)

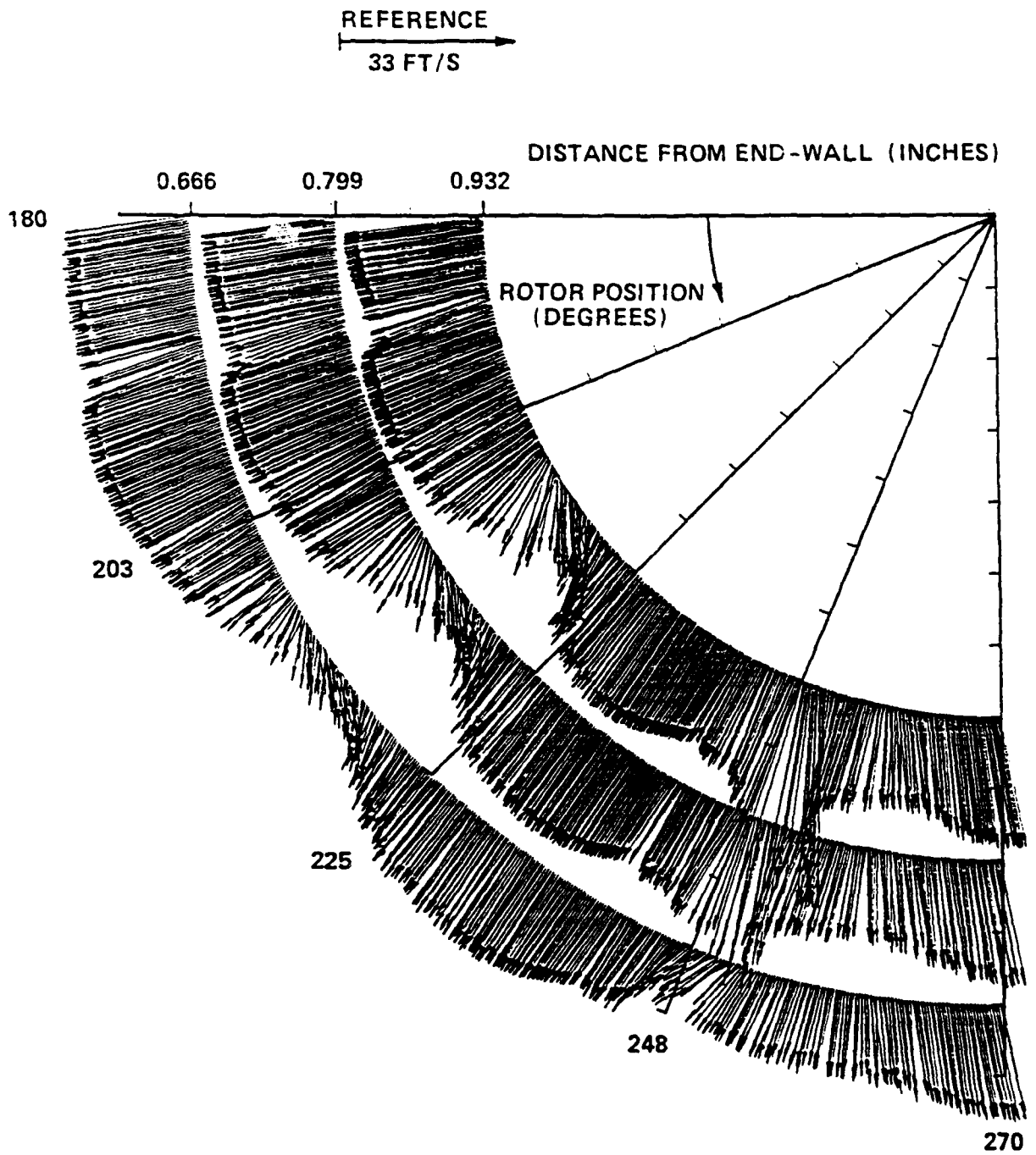


Figure 4.24 (cont.)

(cont. on next page)

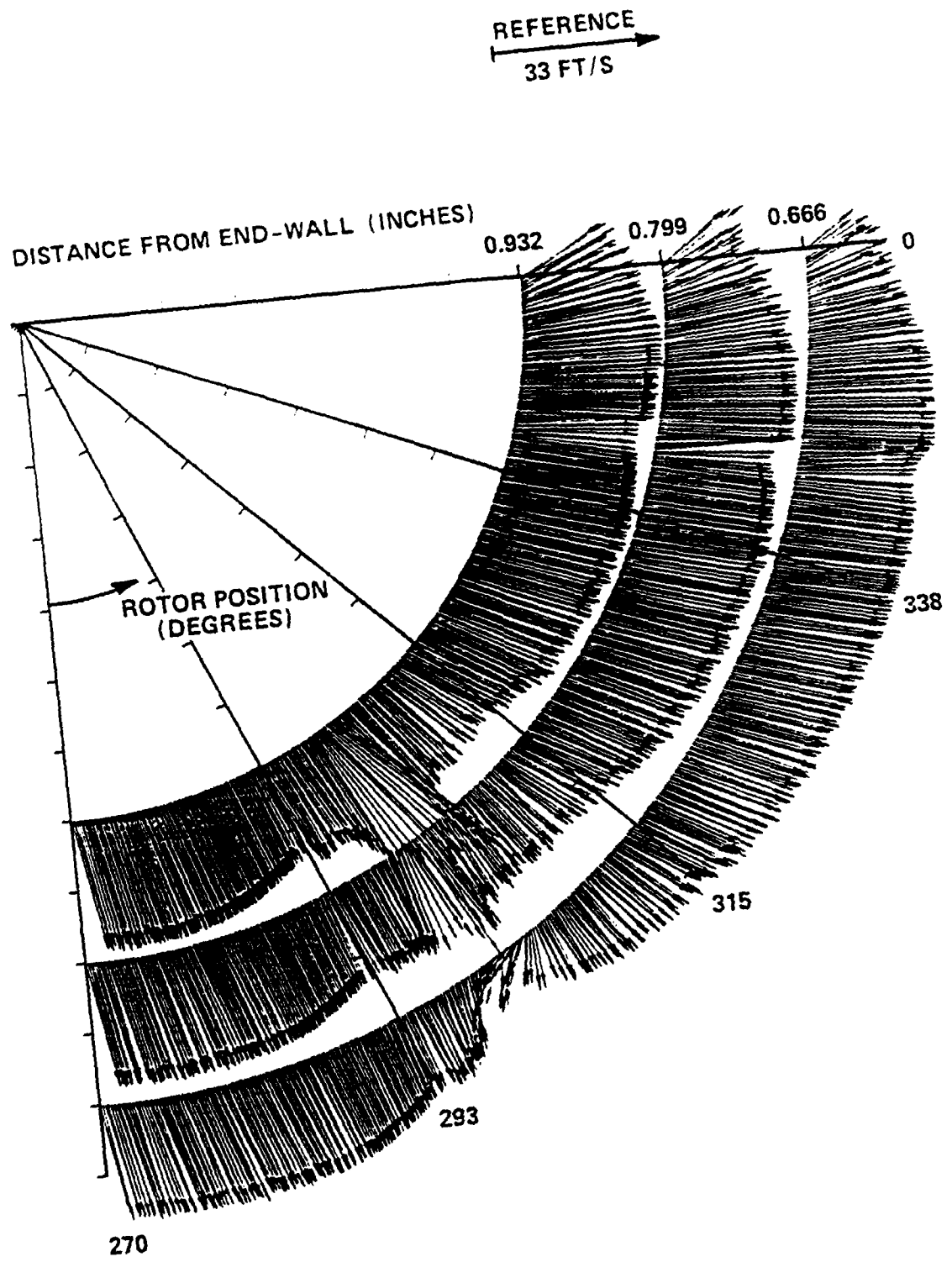


Figure 4.24 (cont.)

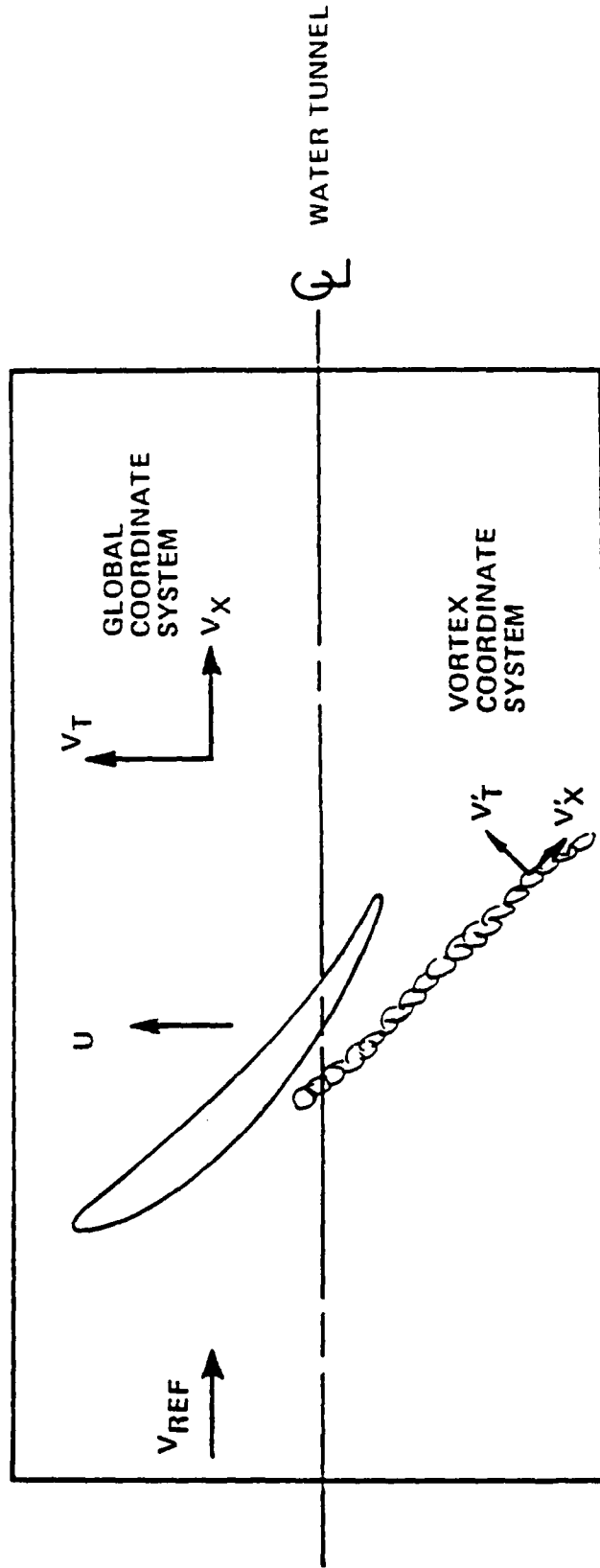


Figure 4.25. Relationship of Global and Vortex Coordinate System

obtained in this manner is not significantly altered by the vortex wandering.

A sample axial and tangential velocity distribution is given in Figure 4.26. The velocity distribution resembles a Rankine vortex; a region of solid body rotation is surrounded by an irrotational, free vortex region. The core radius is defined as one-half of the distance between the maximum tangential velocities. Ideally, the vortex core defines the solid body rotation portion of the vortex and the region of maximum circulation. The tangential velocity distributions were collapsed to a single curve, Figure 4.27. The tangential velocity values were normalized by the maximum value. The vortex is asymmetric with the maximum velocity on the side adjacent to the end-wall. The leakage jet is responsible for the asymmetry. Eventually symmetry is reached as the vortex moves downstream.

The LV surveys taken at the location 2.75 inches downstream of the rotor were used for this analysis. In addition to the vortex core size, the circulation of each of the vortices was calculated. Table 4.3 is a tabulation of the parameters describing the end-wall vortex from each of the blades. The surveys were taken with the rotor operating at a flow coefficient of 1.33 and with an axial velocity of 36 ft/s. The measurements given in Table 4.3 will be discussed at length in Chapter 5.

#### 4.6 Flow Visualization Results

The oil-paint flow visualization technique was used to observe the flow over the rotor tips as a function of the tip clearance. The

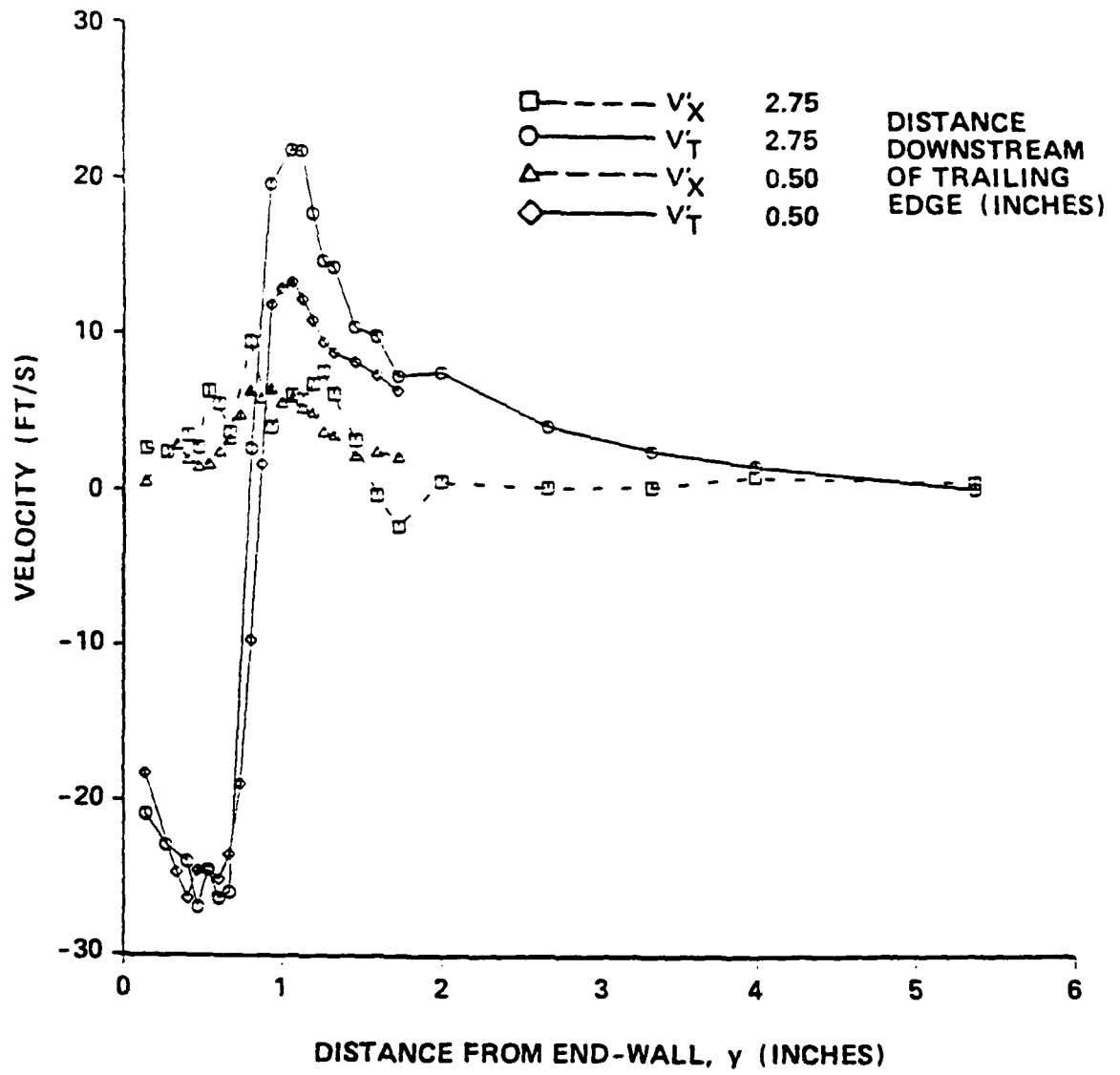


Figure 4.26. Sample Axial and Tangential Velocity Distribution for End-wall Vortex

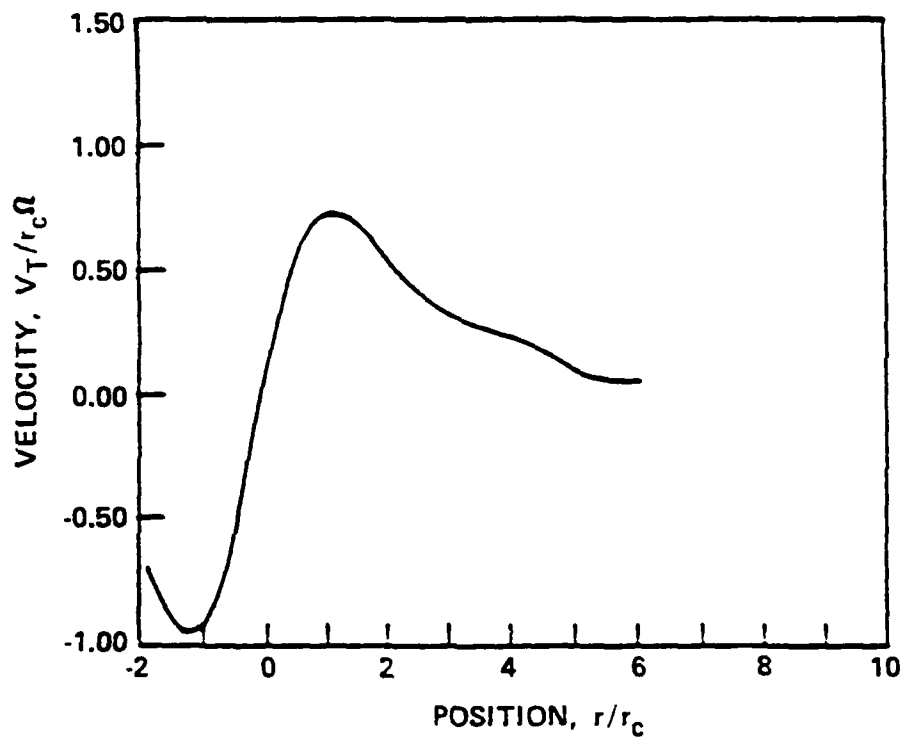


Figure 4.27. Correlation of End-wall Vortex Velocity Distributions

TABLE 4.3

End-wall Vortex Parameters from LV Measurements

<u>Blade</u>	<u>Core radius</u> (in)	<u>Maximum circulation</u> (ft <sup>2</sup> /s)	<u>Tip clearance</u> (in)(dimensionless)	
1	0.78	4.17	0.086	0.099
2	0.38	5.01	0.286	0.329
4	0.31	7.29	0.476	0.547
5	0.23	6.87	0.470	0.540
7	0.56	7.59	0.243	0.279

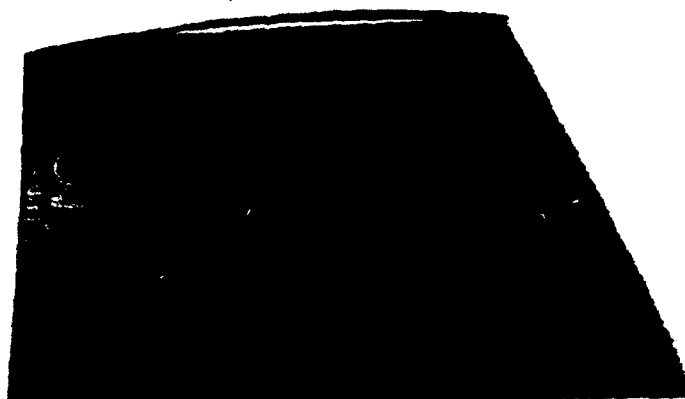
flow visualization test was completed at a flow coefficient of 1.33 and an axial velocity of 36 ft/s. Photographs of the blade pressure surface, suction surface, and tip surface are illustrated for tip clearances of 0.108, 0.286, and 0.476 inches in Figures 4.28, 4.29, and 4.30.

A spanwise accumulation of oil-paint near the leading edge is indicative of boundary layer transition. Figure 4.28a illustrates the pressure surface of rotor blade number three operating at a tip clearance of 0.108 inches. Transition is observed at approximately 5-percent chord. The location of the transition moves away from the leading edge as the incidence angle is decreased. The incidence angle decreases with increasing tip clearance as illustrated in Figure 4.13. Figure 4.29a illustrates the pressure surface of rotor blade number two operating at a tip clearance of 0.286 inches. Observe that the location of transition has moved to approximately 10 percent of the chord from the trailing edge. The pressure surface for blade four which has the largest tip clearance, Figure 4.30, shows indications of transition even further from the leading edge.

The pressure side streak pattern illustrates the extent of the pressure side boundary layer fluid which passes into the tip clearance. The dividing streakline, which connects a point on the leading edge to the trailing edge tip, is much further from the tip in Figure 4.30. The distance of the dividing streakline from the tip varies as the tip clearance.

On the suction side of each of the blades, Figures 4.28b, 4.29b, and 4.30b, separation is observed near the trailing edge. Blade

(a)



(b)



(c)

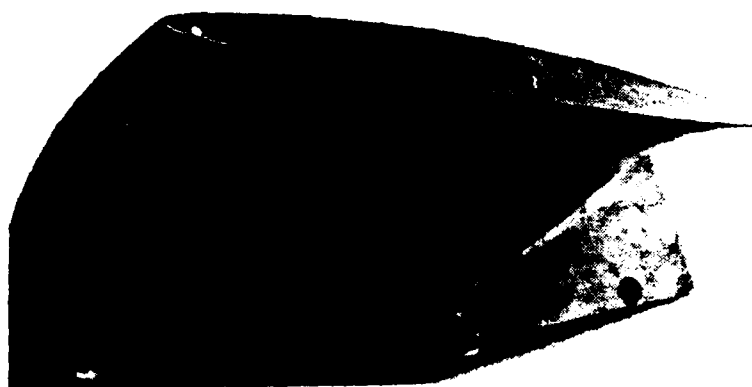
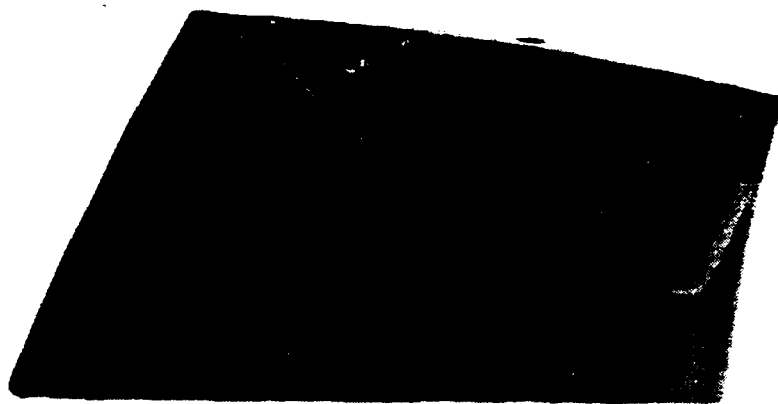


Figure 4.28. Flow Visualization Photograph of Rotor Blade with Dimensionless Clearance of 0.124

(a)



(b)



(c)



Figure 4.29. Flow Visualization Photograph of Rotor Blade with Dimensionless Clearance of 0.329

(a)



(b)



(c)

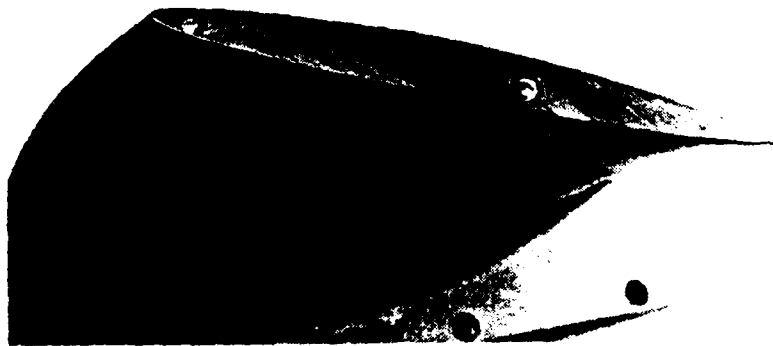


Figure 4.30. Flow Visualization Photograph of Rotor Blade with Dimensionless Clearance of 0.547

number three has been oil-painted on the entire span; it is obvious that the root of the blade is operating at an off-design condition for this blade section. The separated region on this blade is quite extensive. In Figures 4.29b and 4.30b, a vortex can be seen at the trailing edge formed from the separated fluid. The axis of the vortex lies parallel to the trailing edge and migrates radially outward along the span. The end-wall vortex can also be observed lying parallel to the tip on the blades operating at the larger tip clearances -- Figure 4.29b and Figure 4.30b. The end-wall vortex on blade number three, which has the smallest gap, is not observed in the streak pattern. From the video cassette recordings of the cavitation tests, the leakage flow crossed the blade tip and wrapped up away from the suction side of the blade, near mid-passage. At this location, the vortex was unable to affect the streak pattern on the suction side. For increasing tip clearance, the vortex was found to wrap up closer to the blade, and in the case of the largest tip clearance tested on blade four, the vortex was adjacent to the suction surface of the blade.

From a comparison of the tip surfaces of each of the blades, Figures 4.28c, 4.29c, and 4.30c, one can immediately postulate the relative tip clearance sizes. For the smaller tip clearances, the streakline angle with the chord is much larger than for the larger tip clearances. Overall the flow on the tip of the blades is well behaved and no separation is observed. The intersection of the tip surface and pressure surface is well rounded for this purpose.

Rains [27] related the tip lift coefficient with the angle between the leakage flow vector and the chord in his inviscid, perturbation analysis. In the subject investigation, the streaklines from the flow visualization photographs give an approximation of the angle of the leakage flow vector with the chordline. Using these angles, a tip lift coefficient was determined from Rains' inviscid theory. A comparison of these calculated values of the tip lift coefficient is illustrated in Figure 4.31. The experimental measurements yield a value of lift coefficient which is higher than the calculated value for all tip clearances. The lift was measured on the top 10 percent of the blade span; thus, the actual value of the lift on the tip section is less. The experimental lift coefficient variation with tip clearance appears to be predicted by the inviscid analysis of Rains; however, there appears to be a discrepancy in magnitude.

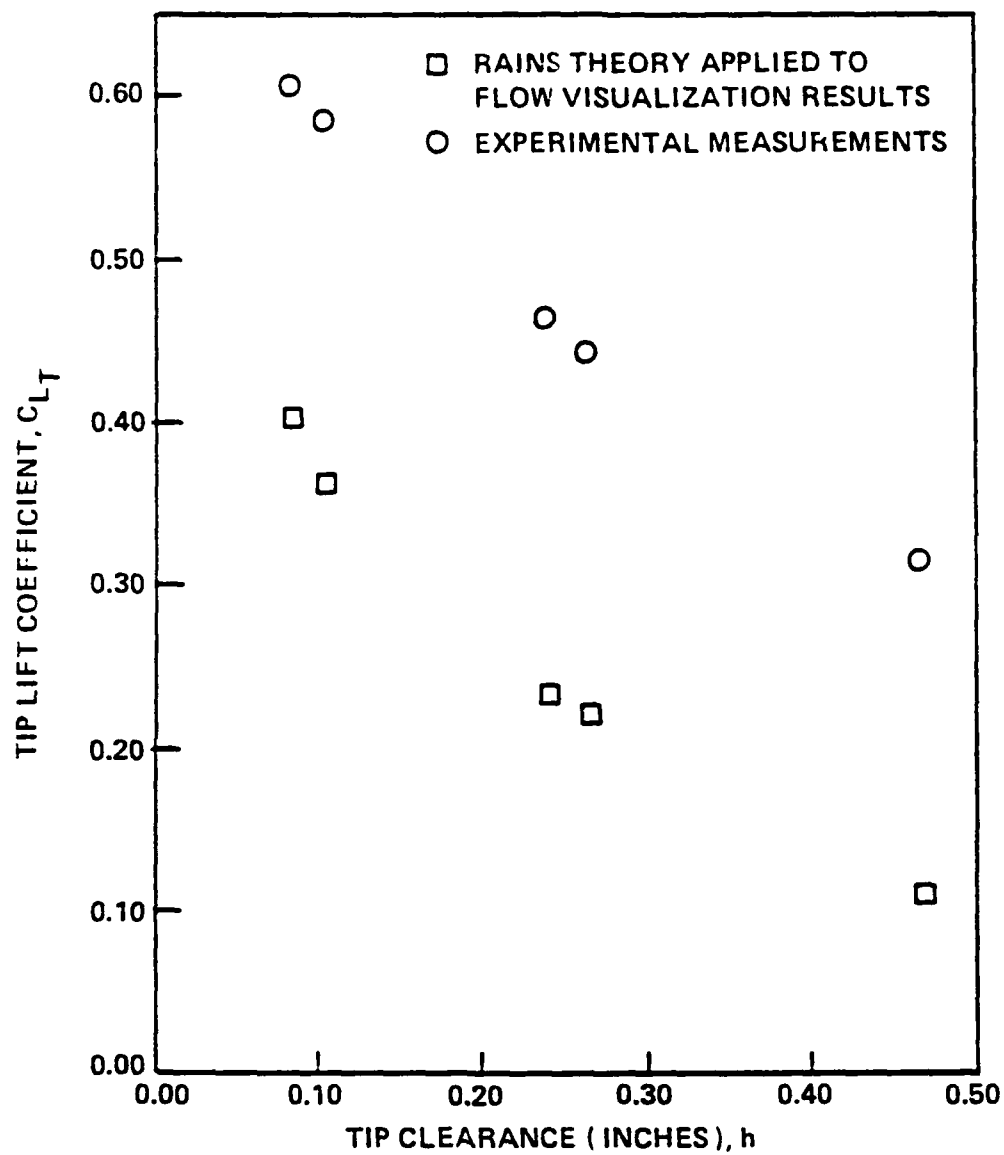


Figure 4.31. Comparison of Rains' [27] Theoretical Tip Lift Coefficient with the Subject Data

Chapter 5  
MODEL DEVELOPMENT

5.1 Analysis

Classical cavitation theory, which ignores bubble dynamic effects, states that cavitation will occur when the local pressure is equal to the vapor pressure and, hence, one has

$$\sigma = -C_{P_{\min}} \quad (5.1)$$

Observations from the data and the literature show that the cavitation number is a function of flow and geometrical parameters: tip clearance, rotational speed, and the end-wall boundary layer. Also, vortex cavitation scaling laws indicate a pressure field dependence upon viscous effects in terms of the Reynolds number raised to a fractional power. The tip clearance and wall boundary layer influence the incidence angle and hence the loading on the tip section of the rotor blade.

In Section 4.5.2 it was noted that the laser velocimeter surveys of the leakage vortex showed a tangential distribution resembling a Rankine vortex. The expression for the minimum pressure coefficient in a Rankine vortex serves as a starting point for this analysis:

$$C_{P_{\min}} = -2 \left[ \frac{\Gamma}{2\pi r_c U} \right]^2 \quad (5.2)$$

Sub-models are required for the circulation and core size.

### 5.1.1 Shed Lift Sub-model

The circulation in the tip wall vortex consists of vorticity shed from the blade tip. The other secondary and scraping vortices have been shown to be an order of magnitude less than the shed vorticity. The vorticity shed from the blade tip represents the reduction in tip lift caused by the presence of the end-wall. The circulation about the tip is given by

$$\Gamma_{\text{tip}} = C_{L_{\text{tip}}} w_1 \frac{c}{2} \frac{U^2}{w_1^2} \quad (5.3)$$

The squared ratio of the tip speed and relative velocity was chosen because the measured values of the tip lift coefficient were normalized by the tip speed instead of the inlet relative velocity,  $w_1$ . The tip speed was used during data acquisition because it is more accurately measured than the inlet velocity. The freestream inlet velocity at the tip in Equation 5.3 depends upon the boundary layer thickness and the tip clearance. The tip lift coefficient depends upon the flow coefficient and the tip clearance.

As the tip clearance is increased, a larger amount of the circulation retained on the tip for smaller clearances, is shed into the end-wall vortex. In contrast, for a zero clearance condition, no leakage flow exists, and thus the maximum amount of circulation is retained on the tip. This relationship can be expressed as

$$\Gamma_o = \Gamma_{\text{tip}} + \Gamma_{\text{tv}} \quad (5.4)$$

Inherent in Equation 5.4, is the assumption that other vorticities generated and shed in the tip region are negligible. In Section

4.2.1, the relationship of the tip lift and the tip clearance was established. Using Equations 2.2, 5.3, and 5.4 above, the end-wall vortex circulation can be expressed as

$$\Gamma_{tv} = C_{L_o} W_1 \frac{c}{2} \frac{U}{W_1}^2 [1 - \exp(-14h/c)] \quad (5.5)$$

A plot of Equation 5.5 with the LV data of Table 4.3, Figure 5.1, illustrates that the circulation in the end-wall vortices is larger than that predicted by the tip lift measurements. Apparently, another source of circulation exists which is shed into the end-wall vortex. One possibility, as observed from the flow visualization results in Section 4.6, is the vortex formed from fluid separating from the suction side and migrating radially up the blade span. The scraping vortex on the pressure side of the blade could be suspect, but this is unlikely since the additional circulation is observed for larger tip clearances where the scraping vortex would be minimal if at all present. In view of the this, the equation for the end-wall vortex circulation is modified to include the additional circulation:

$$\Gamma_{tv} = C_{L_o} W_1 \frac{c}{2} \frac{U}{W_1}^2 [1 - \exp(-14h/c)] + \Gamma_{sec} \quad (5.6)$$

A constant level of circulation was added to the circulation shed from the tip. The second term of Equation 5.6 may depend on the gradient of the circulation along the blade span integrated over a characteristic length. The circulation shed from the blade tip comprises only a portion of the circulation shed in the end-wall vortex. The dotted line of Figure 5.1 represents Equation 5.6.

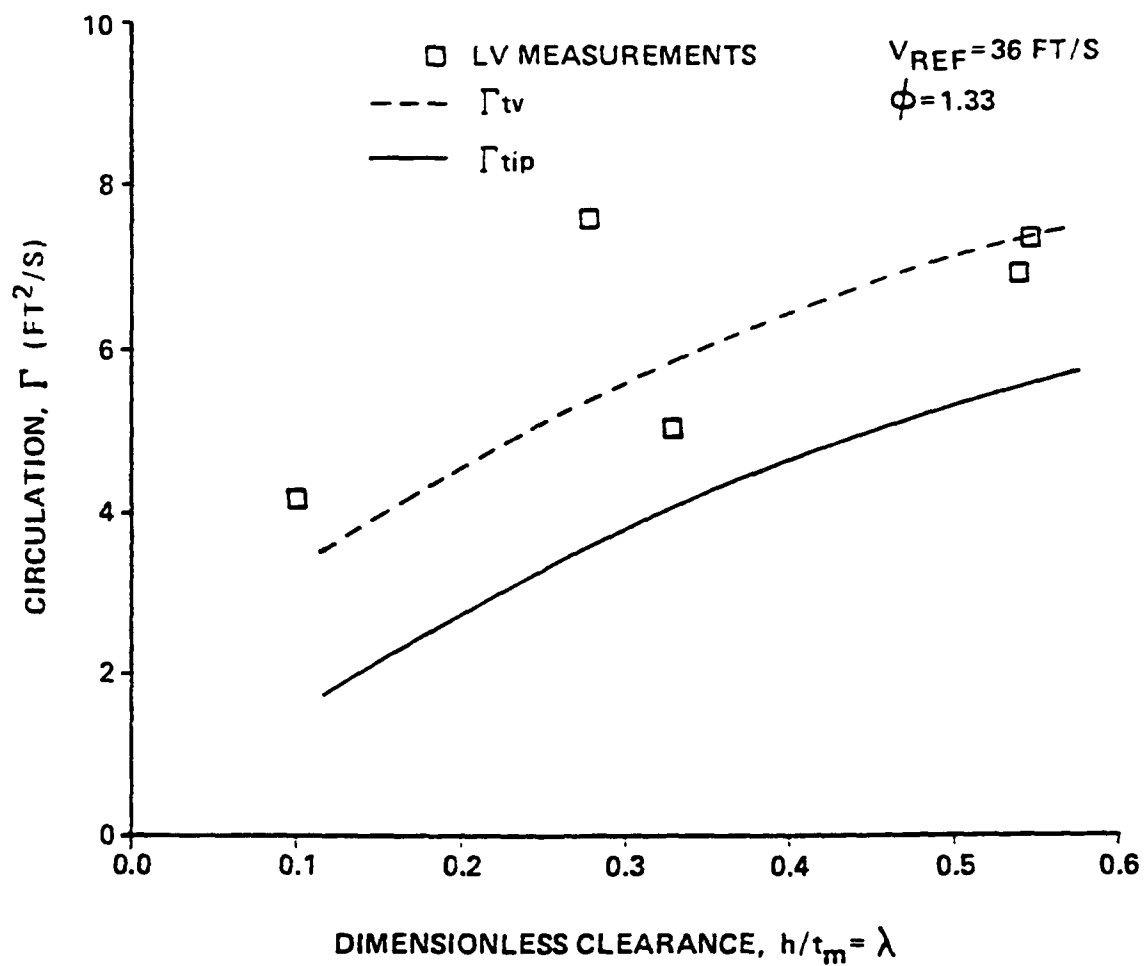


Figure 5.1. Shed Circulation versus Dimensionless Clearance for Subject Data with Sub-model Predictions

Inoue et al. [41] determined the leakage circulation over the blade circulation in their axial compressor and compared this to the predictions of Lakshminarayana [34]. The present measurements are plotted with Inoue's results in Figure 5.2. The subject measurements compare very well with Inoue's results. The fact that the circulation ratio plotted in Figure 5.2 reaches a value near one at a tip clearance to chord ratio of 0.04 also indicates a source of leakage vorticity other than the vorticity shed from the blade tip. The subject measurements appear to follow the same trend.

#### 5.1.2 Vortex Core Radius Sub-model

Equation 5.2 of the previous section also requires that a relationship be established between the end-wall vortex core size and the geometrical and flow parameters of the pump. Specifically, the vortex core size was shown to depend upon the tip lift coefficient, the tip clearance, the location of minimum pressure, and thus the geometry of the blade tip. Borrowing from Rains [27] and using Lakshminarayana's assumption that the sheet radius and core radius are equal, Shuba [1] expressed the end-wall vortex core radius as

$$r_c = 0.14 h \left(\frac{h}{c}\right)^{-0.85} \left(C_{L_{tip}}\right)^{0.425} \left(\frac{\xi}{c}\right)^{0.85} \quad (5.7)$$

However, Shuba provided no experimental verification of Equation 5.7 in his investigation.

Figure 5.3 illustrates the end-wall vortex core radius as a function of the dimensionless tip clearance. The data were recorded with the rotor operating at a flow coefficient of 1.33 and an axial

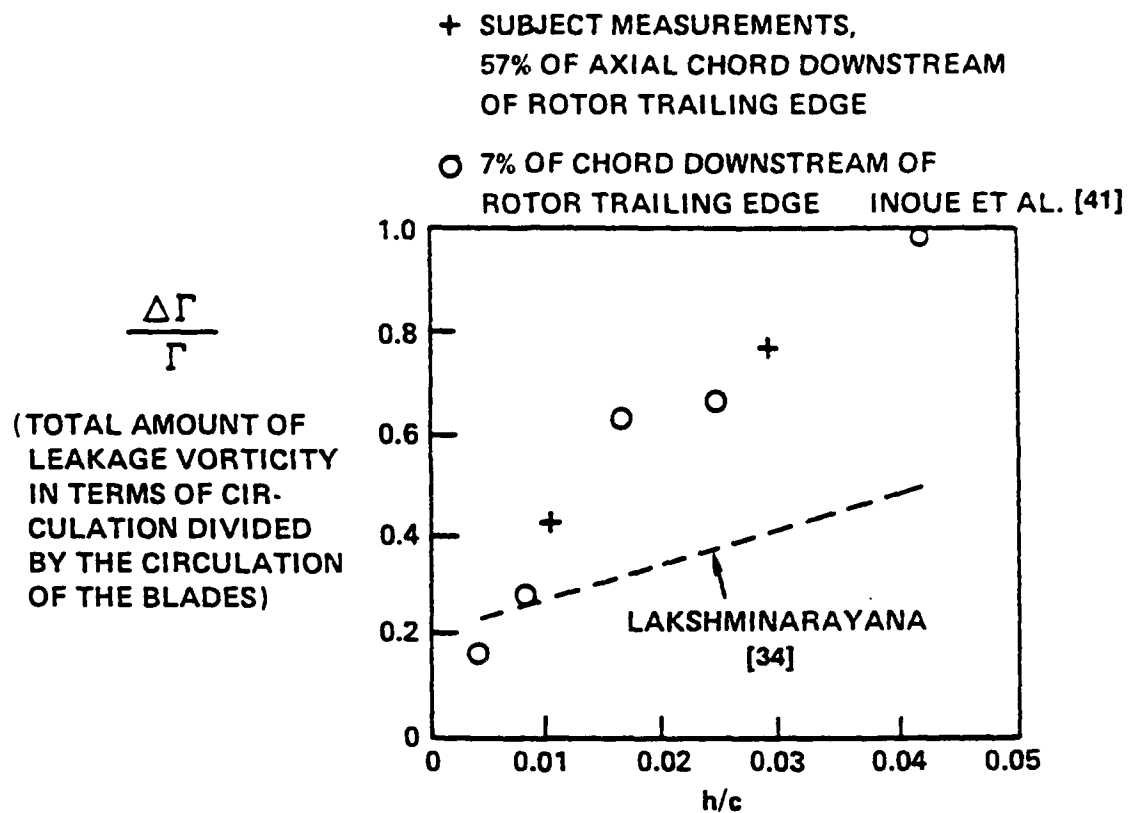


Figure 5.2. Leakage Vorticity versus Tip Clearance to Chord Ratio for Inoue et al. [41], Lakshminarayana [34], and Subject Data, ref. Inoue et al. [41]

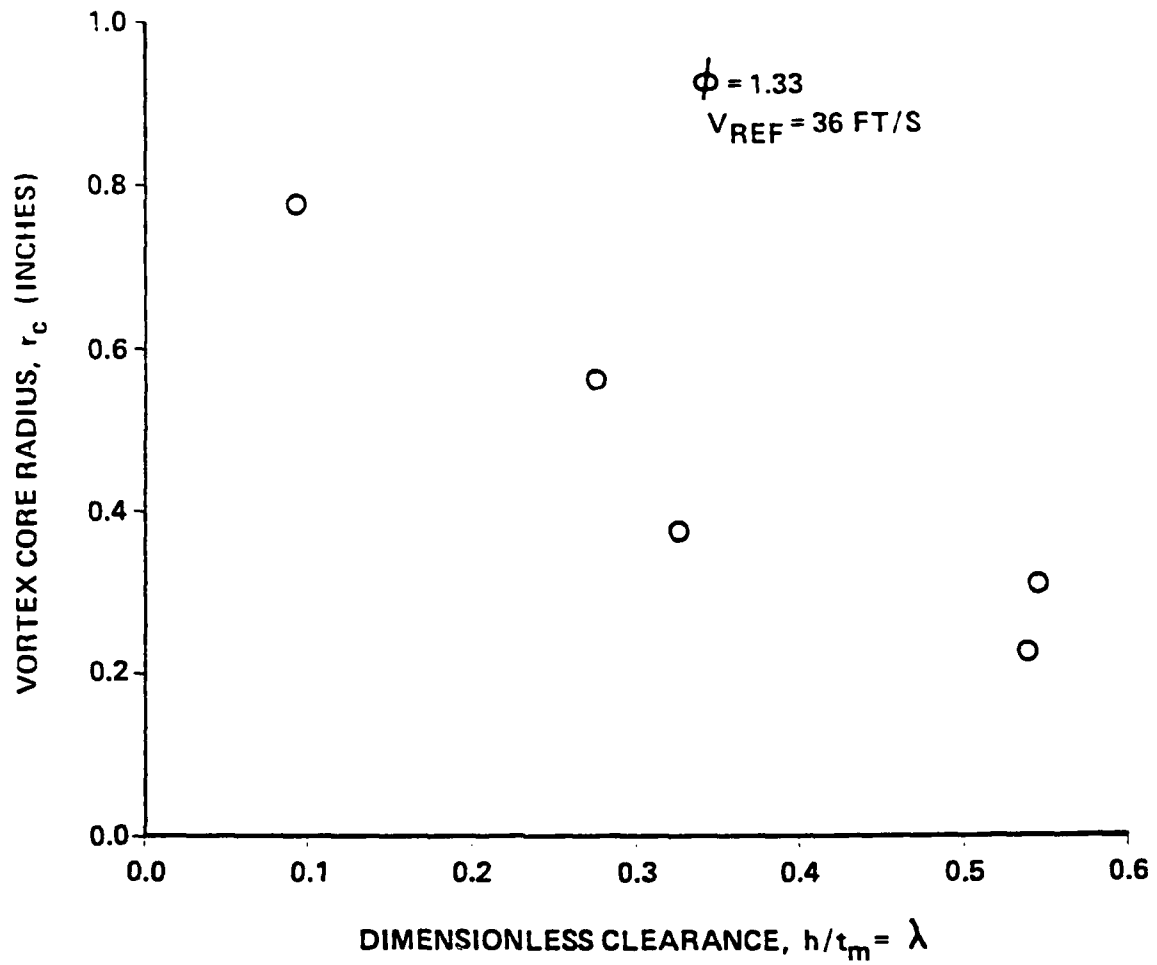


Figure 5.3. Vortex Core Radius versus Dimensionless Clearance for Subject Data

velocity of 36 ft/s. The vortex core size was found to decline with increasing tip clearance, contrary to Equation 5.7.

The video tape recordings of the cavitation tests were examined to provide insight into this phenomenon. The interaction of the vortex generated on the rotor blade suction side and the end-wall vortex appeared to be responsible for the increase in core size at smaller tip clearances. The two vortices wrapped up together at the blade trailing edge, upstream of both LV measurement stations. The vortex generated on the suction side appears to have a substantial influence on the core size of the end-wall vortex for smaller clearances. For smaller tip clearances, recall that the upstream end of the tip vortex formed near the leading edge of the blade. Thus the two vortices originated approximately a blade chord apart and combined into a large diameter structure. For the larger size tip clearances, the two vortices originate near the same location at the trailing edge of the blade, and the end-wall vortex does not appear to change drastically in structure. From Figure 5.2, it is clear that the circulation attributed to sources other than the blade tip constitutes a larger percentage of the total shed circulation for small tip clearances.

Equation 5.7 shows that the vortex core size depends on the shed lift coefficient raised to the 0.425 power. However, when Equation 5.7 is applied to the subject rotor, the vortex core radii are approximately one half of the value measured with the laser velocimeter at a tip clearance of 0.476 inches. Using Equation 4.5

which expresses the tip lift coefficient as a function of tip clearance, one can express the vortex core radius as:

$$r_c = r_{c_{h \rightarrow \infty}} [1 - \exp(-6h/t_m)] \quad (5.8)$$

For the present investigation, the tip vortex core radius for a very large tip clearance can be taken as 0.31 from the laser velocimeter measurements of Figure 5.3. At this condition, the end-wall vortex forms near the trailing edge tip on the suction side and appears to be negligibly affected by the second vortex forming at the trailing edge on the suction side.

In a general sense,  $r_{c_{h \rightarrow \infty}}$  is the core radius of the vortex which would form if the pump rotor was acting as an open propeller. This core radius is obviously a function of the lift coefficient of the blade and the tip geometry. At the present, the database is insufficient to determine a relationship for  $r_{c_{h \rightarrow \infty}}$ . However, one could postulate that the end-wall vortex core size at the open propeller condition is weakly dependent upon tip lift coefficient and strongly dependent upon tip geometry. Based on the measured cavitation indices of Figure 4.1, changes in the operating flow coefficient do not substantially effect the cavitation index. This indicates the weak dependency on lift coefficient as mentioned above. For a first approximation, it seems reasonable to assume a percent of blade chord for  $r_{c_{h \rightarrow \infty}}$ . For the present data, and the theoretical core radius relationship of Shuba [1], 4 to 6 percent of chord is a reasonable estimate.

McCormick [45] and Gearhart and Ross [46] stated the dependency of the cavitation index upon the Reynolds number in scaling model

vortex cavitation data. McCormick noted the dependency of the vortex core radius on the pressure side boundary layer. The equation for a flat plate turbulent boundary layer shows that the boundary layer thickness is inversely proportional to the Reynolds number raised to the one seventh power. Recall that in Equation 5.2 the core radius is squared; the cavitation number depends on Reynolds number to the 0.29 power which is very close to the values of Gearhart and Ross. Incorporating this Reynolds number relation into Equation 5.8 yields

$$r_c = r_{c_{h \rightarrow \infty}}' [1 - \exp(-6h/t_m)] \left( \frac{Re_c}{Re_c'} \right)^{-1/7}, \quad (5.9)$$

where the prime indicates the reference value from which a value of the vortex core radius,  $r_c$ , is to be scaled.

### 5.1.3 End-wall Vortex Correlation Model

A correlation model of end-wall vortex cavitation can be formed by substituting Equations 5.6 and 5.9 into Equation 5.2 to form

$$\sigma = .2 \left[ \frac{C_{L_o} W_1 \frac{c}{2} \left( \frac{U}{W_1} \right)^2 [1 - \exp(-14h/c)] + \Gamma_{sec}}{2\pi r_{c_{h \rightarrow \infty}}' [1 - \exp(-6h/t_m)] U} \right]^2 \left( \frac{Re_c}{Re_c'} \right)^{2/7}. \quad (5.10)$$

Equation 5.10 contains all of the known parameters which correlate with the cavitation index. The section lift coefficient enters through the model for the shed lift. The tip clearance is a variable in the expressions for the shed lift and the vortex core size. The Reynolds number dependency of scaling relationships enters through the core radius, since this parameter is related to the pressure side boundary layer. The geometry of the blade enters through the chord

length, tip thickness, and through the open propeller vortex core radius,  $r_{c_{h \rightarrow \infty}}$ . The characteristics of the inflow to the tip region enter through the relative velocity. The remaining task is to verify the correlation model through the data of the present investigation and from other researchers.

## 5.2 Application of the Model

### 5.2.1 Present Data from the High Reynolds Number Pump

The present experimental data present an easy application of the correlation model of Section 5.1 since the experiment was designed for the specific purpose of formulating and verifying such a theory. On the contrary, other investigations of end-wall vortex cavitation do not always contain the appropriate parameters needed for the model.

The vortex core radius is plotted in Figure 5.4 for the three test velocities, 26, 31, and 36 ft/s using Equation 5.9. This relation was used for all flow coefficients tested by invoking the earlier assumption of a weak dependency of  $r_{c_{h \rightarrow \infty}}$  on the flow coefficient.

Equation 5.6 provides the circulation of the end-wall vortex for various operating conditions. The lift coefficient  $C_{L_0}$  was measured as a function of flow coefficient as mentioned in Section 4.2.1. In the instance of a design calculation, presumably the lift coefficient would be known over a range of off-design conditions. Since the end-wall vortices were surveyed with the laser velocimeter, the total circulation is known, and one can calculate the additional circulation required in Equation 5.6.

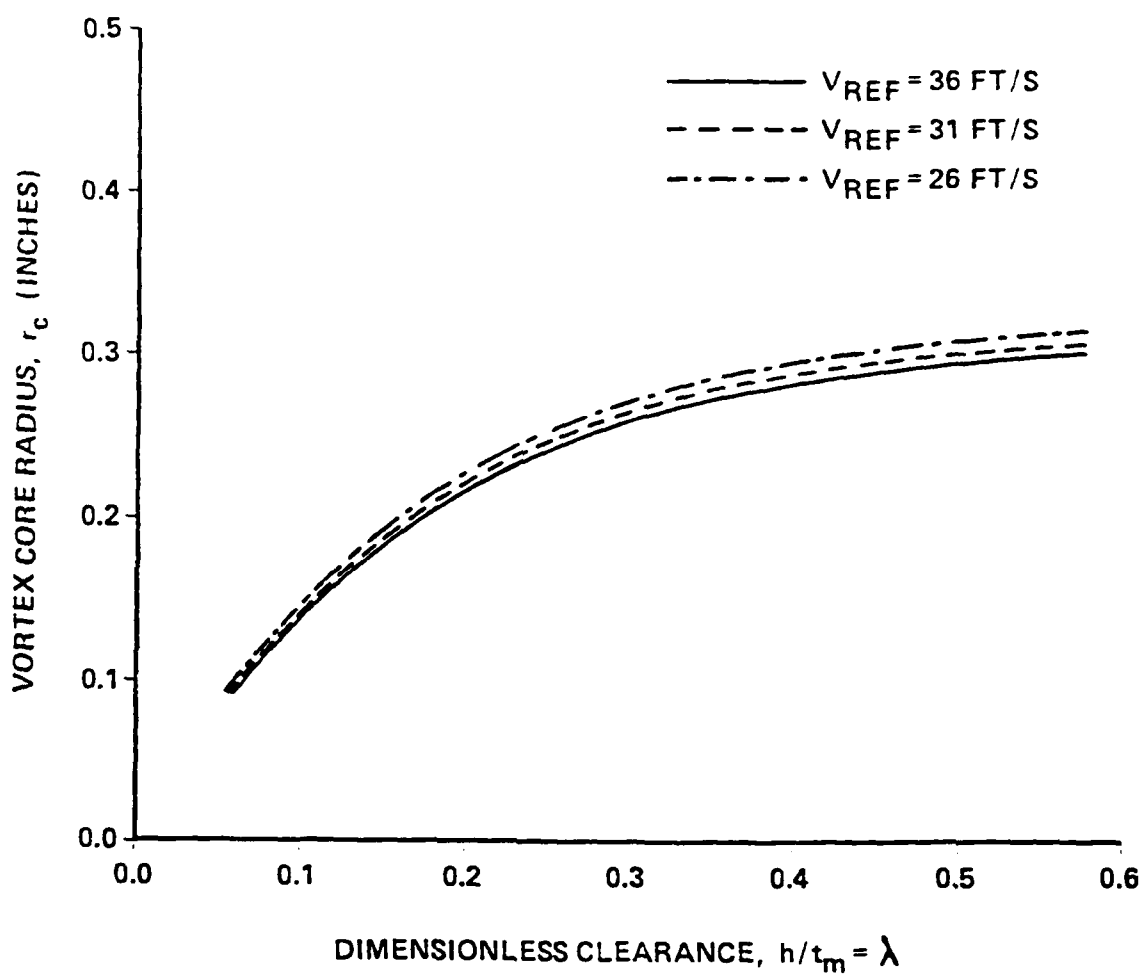


Figure 5.4. Theoretical Vortex Core Radius versus Dimensionless Clearance for Axial Velocities of 26, 31, and 36 ft/s for Subject Data

The results of applying the correlation model to the High Reynolds Number Pump are illustrated in Figure 5.5 for the three flow coefficient ranges tested. The model does predict the existence of an optimum clearance near  $\lambda = 0.2$ . Previous investigators [1,27,34,43,46] have noticed minima near  $\lambda = 0.15$ . At small clearances the curves for all three flow coefficient turn upward, whereas for the data, no consistent trend is observed. The cavitation index increases, remains nearly constant, or decreases depending on the flow coefficient. This trend was repeatable as shown in Figure 4.1 for all three blades tested and at all three velocities. Based on these results, it would appear to be a flow field related phenomenon rather than a surface condition characteristic of a particular blade. An explanation of this characteristic is not forthcoming, since the slight change in flow coefficient does not change the incidence angle significantly as illustrated in Figure 4.13.

Figure 5.6 illustrates the correlation model results with the recorded cavitation indices for the rotor operating at a flow coefficient of 1.33 for three axial velocities. The turbulent boundary layer power law relation appears satisfactory for Reynolds number scaling, even over the small range of velocities tested. Based on Figures 5.5 and 5.6, the correlation model appears useful for the High Reynolds Number Pump.

#### 5.2.2 Data from Other Investigators

A greater test of the usefulness of the end-wall vortex model lies in its ability to correlate data from investigations other than

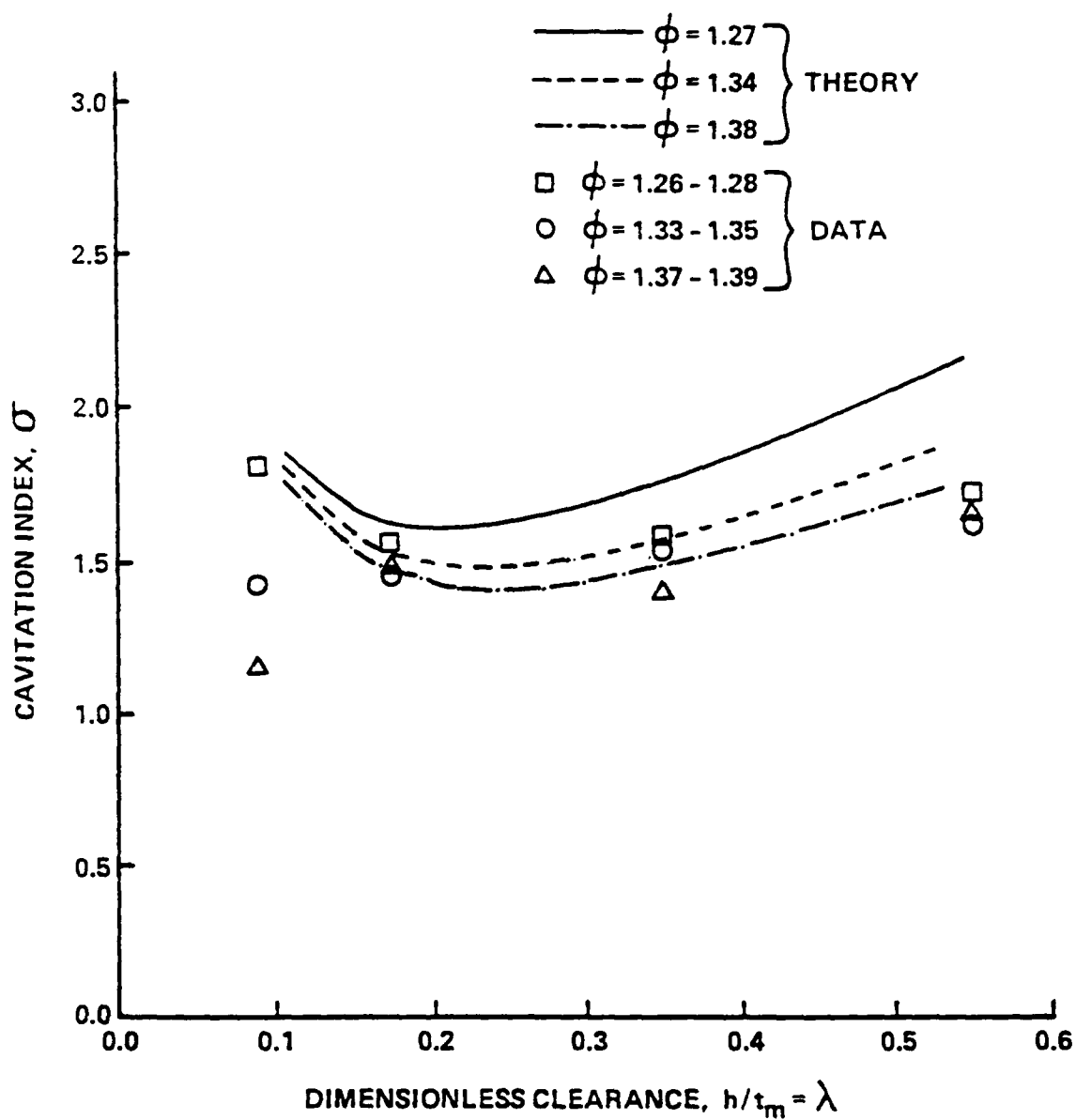


Figure 5.5. Theoretical and Measured Cavitation Indices for Three Flow Coefficients at 36 ft/s for the Subject Data

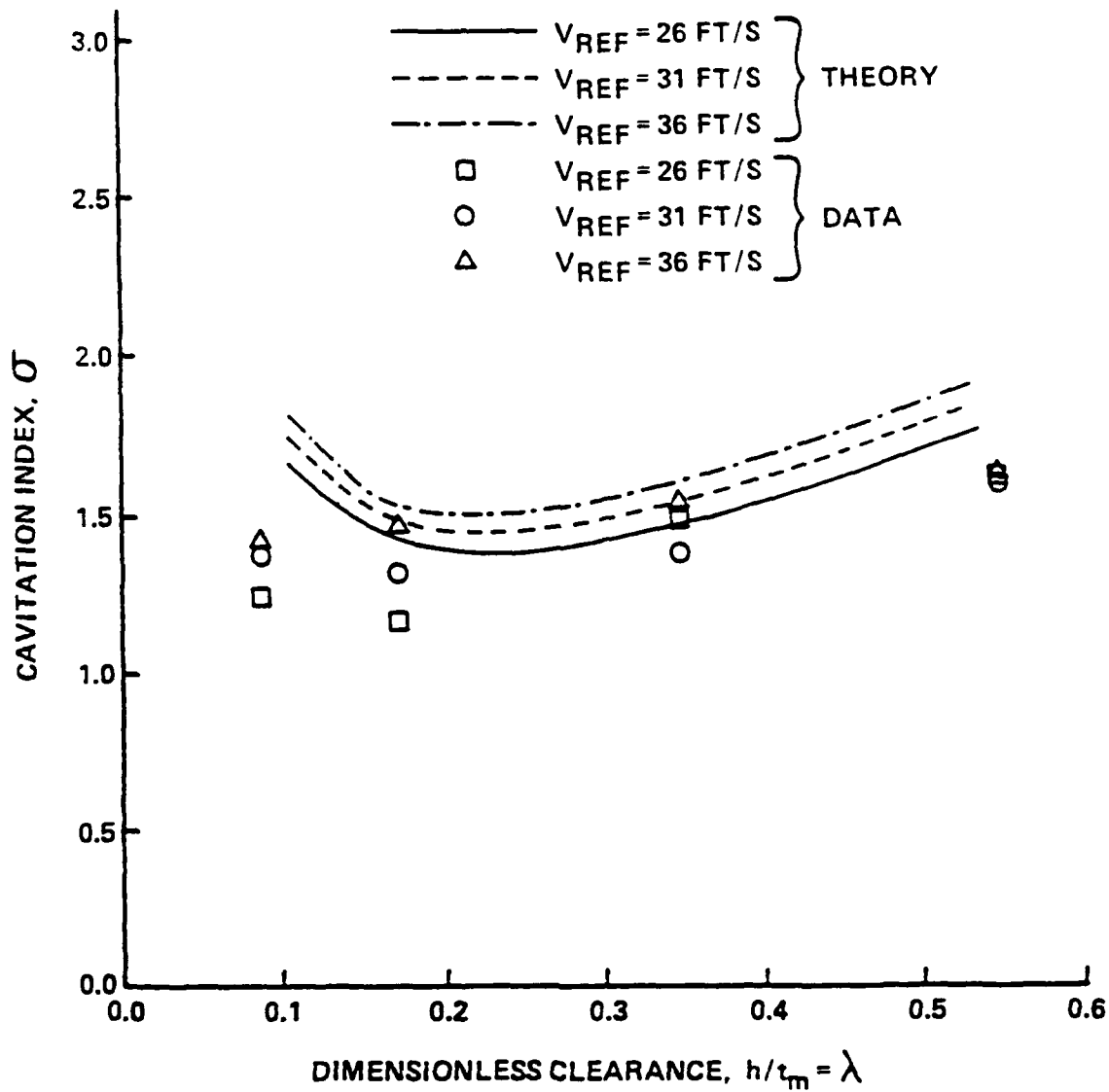


Figure 5.6. Theoretical and Measured Cavitation Indices for Velocities of 26, 31, and 36 ft/s Representing  $Re_c$  of  $1.6 \times 10^6$ ,  $1.9 \times 10^6$ , and  $2.2 \times 10^6$  Respectively, at a Flow Coefficient of 1.33 for the Subject Data

that from which it was derived. The data of Shuba [1] is useful to this end. Neither measurements of tip lift nor vortex core size were conducted. However, reasonable results are obtained by using 5 percent of the tip chord length as an estimate for the vortex core size at the open propeller condition and an estimate for the tip lift coefficient  $C_{L_0}$ .

The functions for the vortex core radius and the shed circulation are given in Figures 5.7 and 5.8. The relation of Figure 5.7 is derived from Equation 5.8 with the estimate for  $r_{c_{h \rightarrow \infty}}$  as mentioned above. Similar to the HIREP data, additional circulation must be shed from the rotor blade for the pump used by Shuba. For small clearances, the end-wall vortex circulation is nearly twice the circulation attributed to that shed from the tip alone.

Using the above relations for the end-wall vortex core radius and the shed circulation, cavitation indices, based on the mean axial velocity, were predicted for Shuba's rotor operating at a flow coefficient,  $V_x/U$ , of 0.877 and 836 RPM. The results are illustrated in Figure 5.9. Excellent agreement is observed, particularly at values of tip clearances where normal operation would occur.

The correlation model of end-wall vortex cavitation can also be applied to the experimental investigation of Rains [27]. A relationship given by Rains was used to calculate a tip lift coefficient. The vortex core size  $r_{c_{h \rightarrow \infty}}$  was estimated using a value equal to 6 percent of the tip chord length. The relationships for the vortex core size and the shed circulation are given in Figures 5.10 and 5.11. As noted in the subject investigation and Shuba's

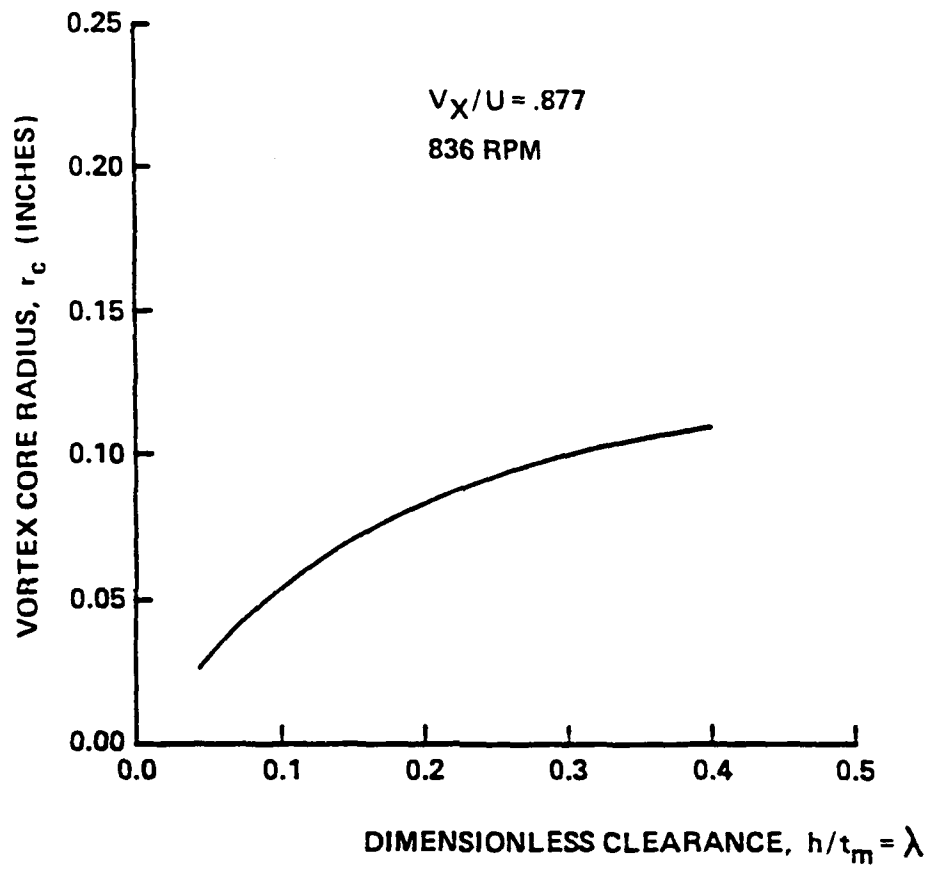


Figure 5.7. Sub-model Prediction of Vortex Core Radius versus Dimensionless Clearance for Shuba's [1] Data

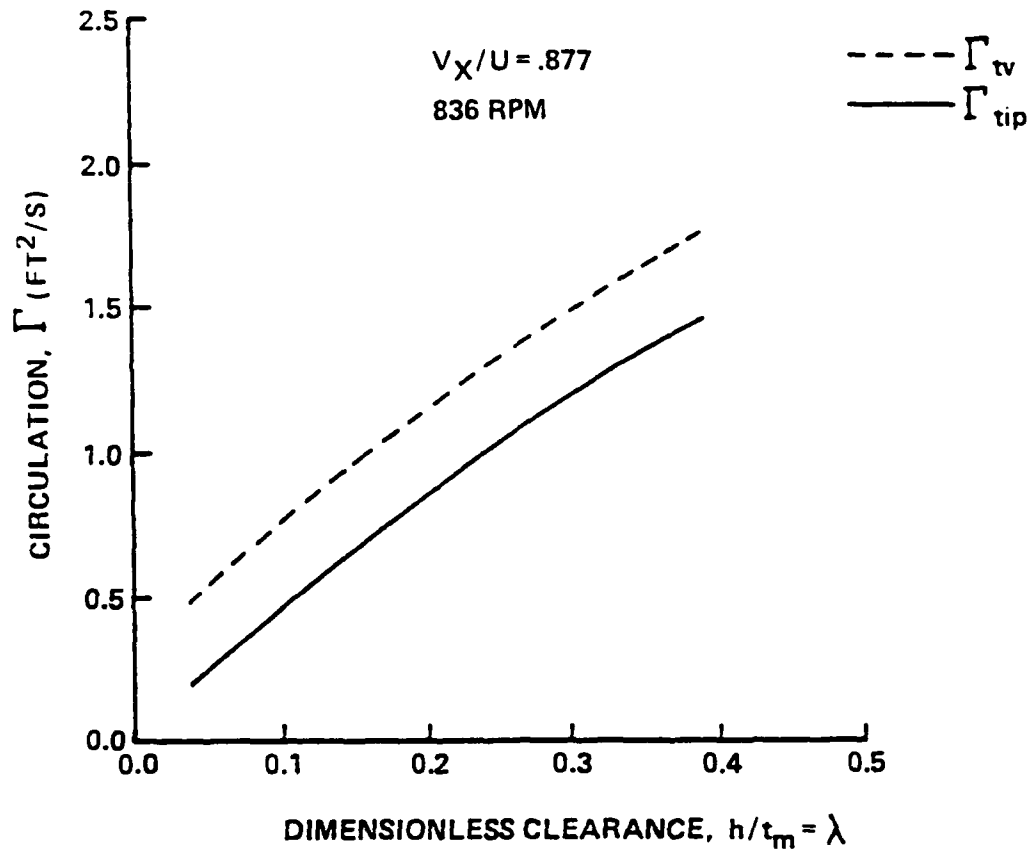


Figure 5.8. Sub-model Prediction of Shed Circulation versus Dimensionless Clearance for Shuba's [1] Data

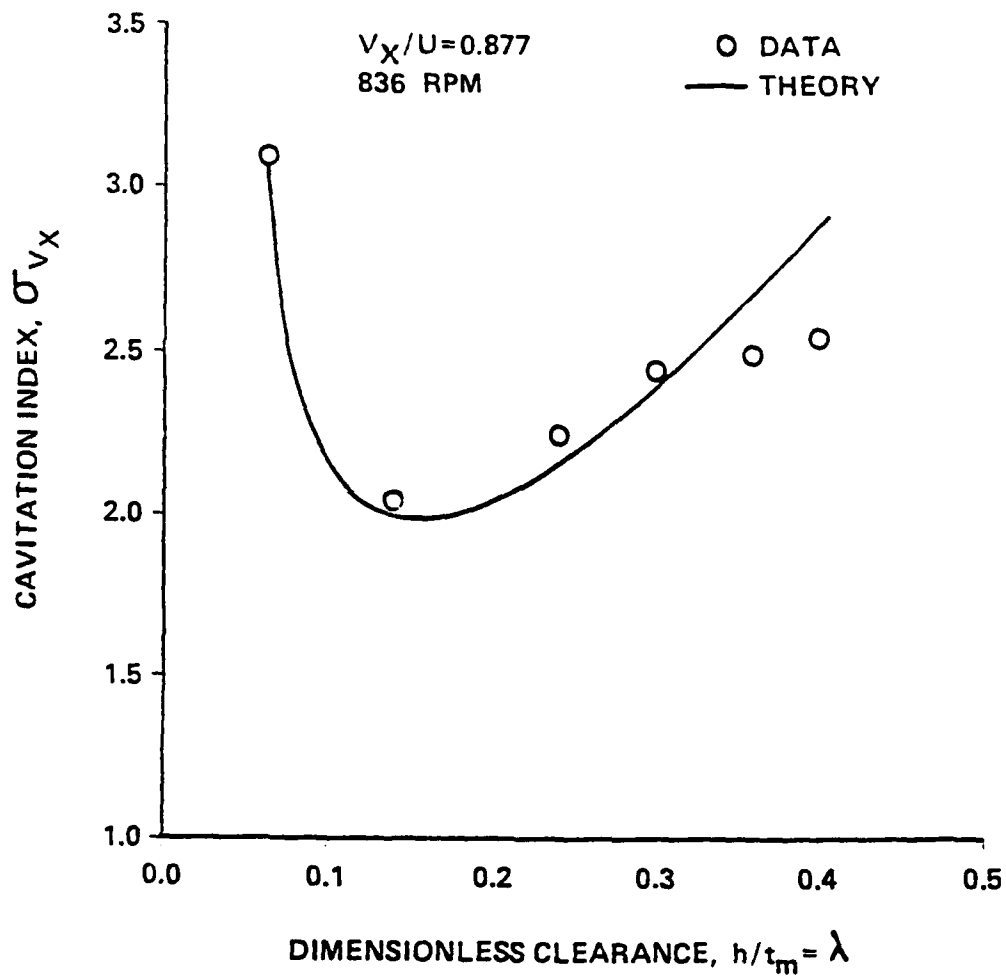


Figure 5.9. Theoretical and Measured Cavitation Indices for  $V_x/U = 0.877$ , 836 RPM, and  $Re_c = 1.1 \times 10^6$  for Shuba's [1] Data

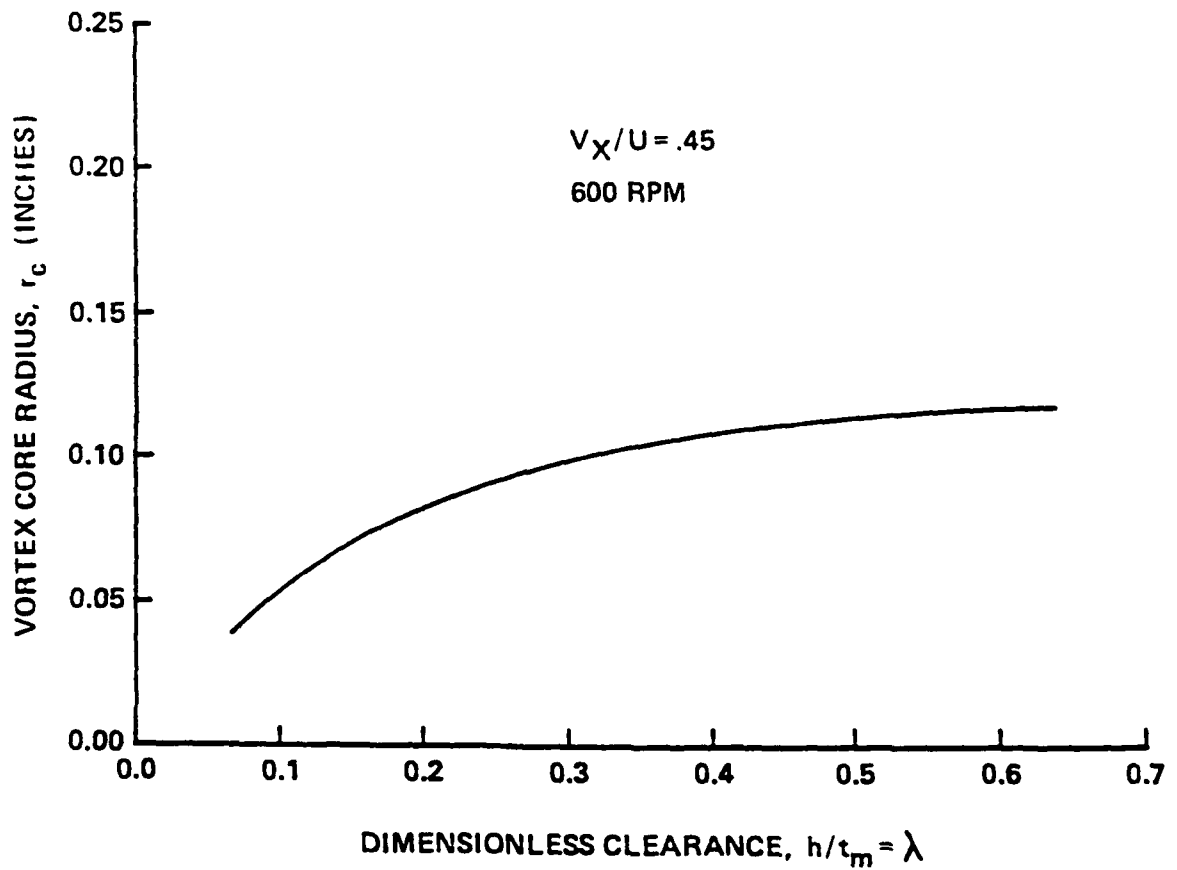


Figure 5.10. Sub-model Prediction of Vortex Core Radius versus Dimensionless Clearance for Rains' [27] Data

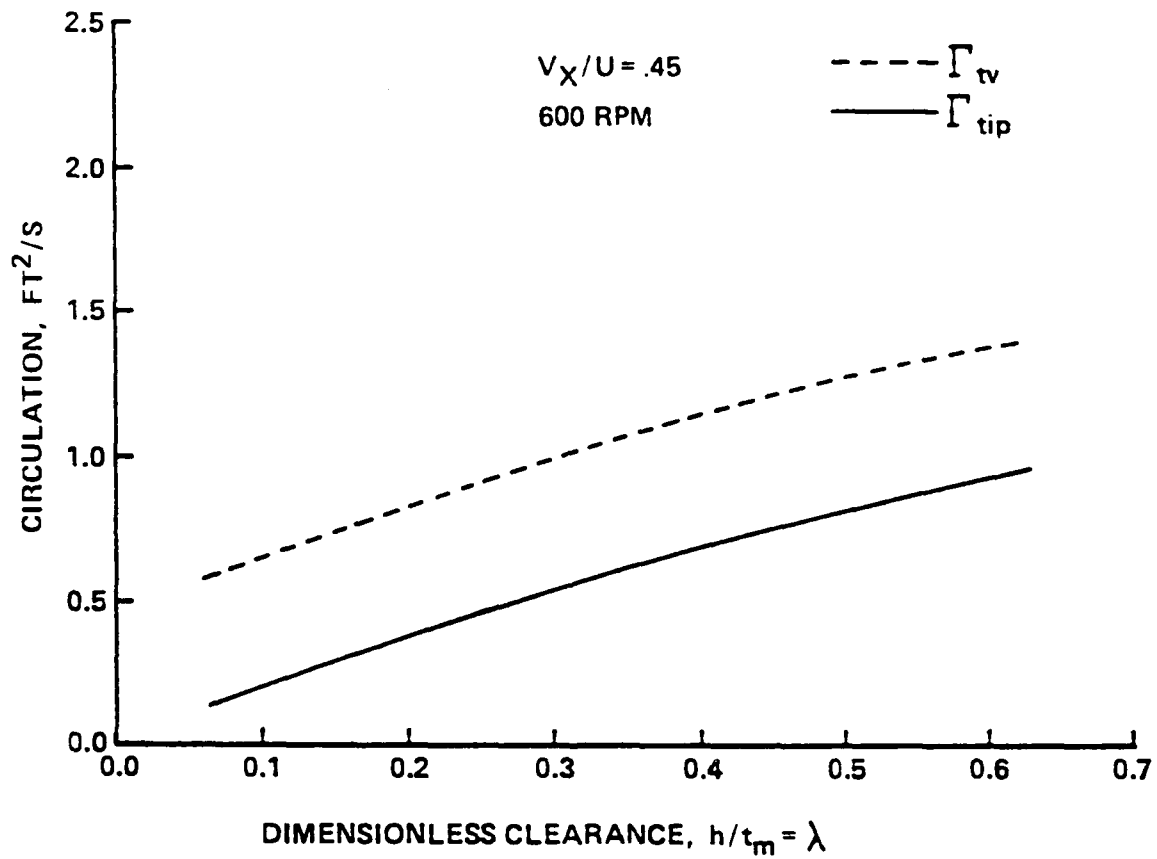


Figure 5.11. Sub-model Prediction of Shed Circulation versus Dimensionless Clearance for Rains' [27] Data

study, the end-wall vortex circulation is the sum of the circulation shed from the tip and additional circulation shed from the blade trailing edge. The cavitation indices, based on the velocity relative to the blade, were calculated at the design flow coefficient,  $V_x/U$ , of 0.45 and with a rotational speed of 600 RPM. A comparison of the measured, inception data is given in Figure 5.12; again, good agreement is observed. The air content levels were not recorded in Rains' investigation.

Mitchell's data [43] was used as a final application of the correlation given in Equation 5.10. Howell's cascade correlation [56] was used to predict a tip lift coefficient for the circular arc blades. As before, the vortex core radius was estimated as 5 percent of the tip chord length. The vortex core radius and the shed circulation relationships are given in Figures 5.13 and 5.14. The calculated cavitation indices, based on the mean axial velocity, are compared with experimental values in Figure 5.15; reasonable agreement is observed. The air content level was not a variable in Mitchell's investigation.

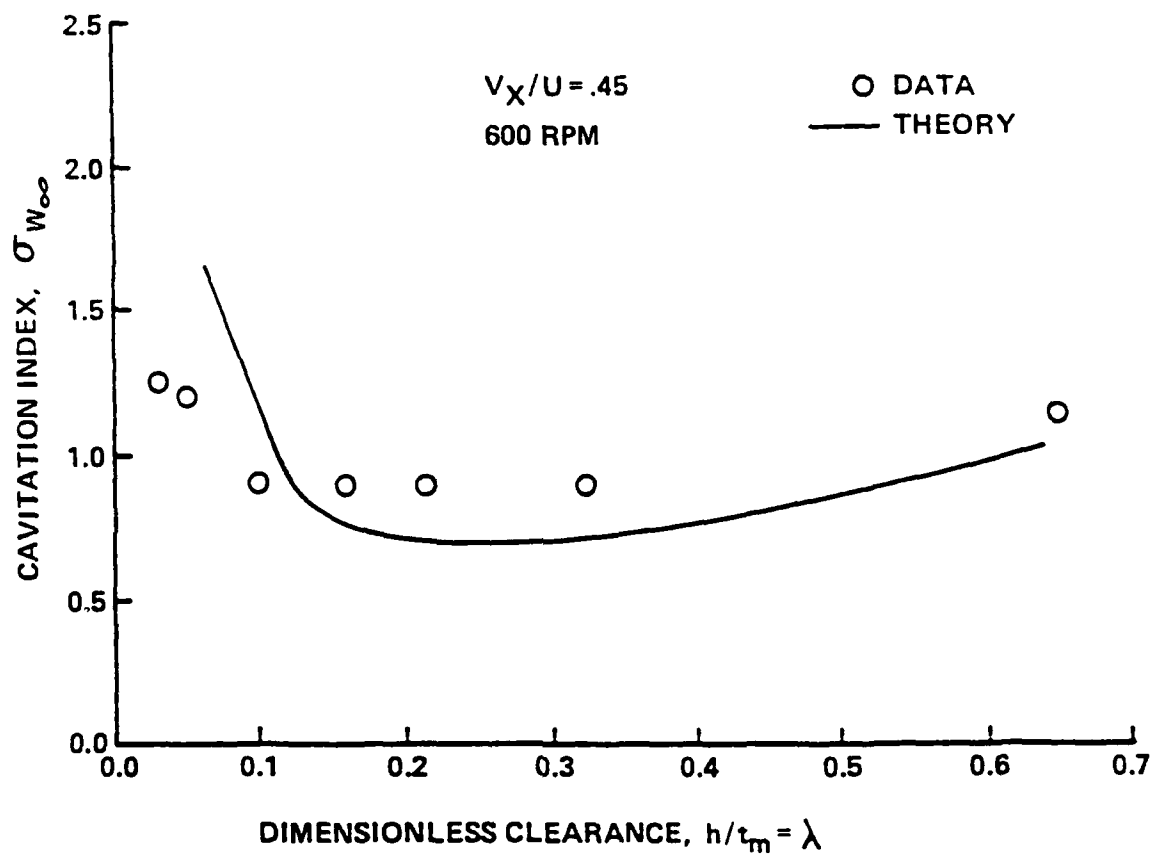


Figure 5.12. Theoretical and Measured Cavitation Indices for  $V_X/U = 0.45$ , 600 RPM, and  $Re_c = 5.8 \times 10^6$  for Rains' [27] Data

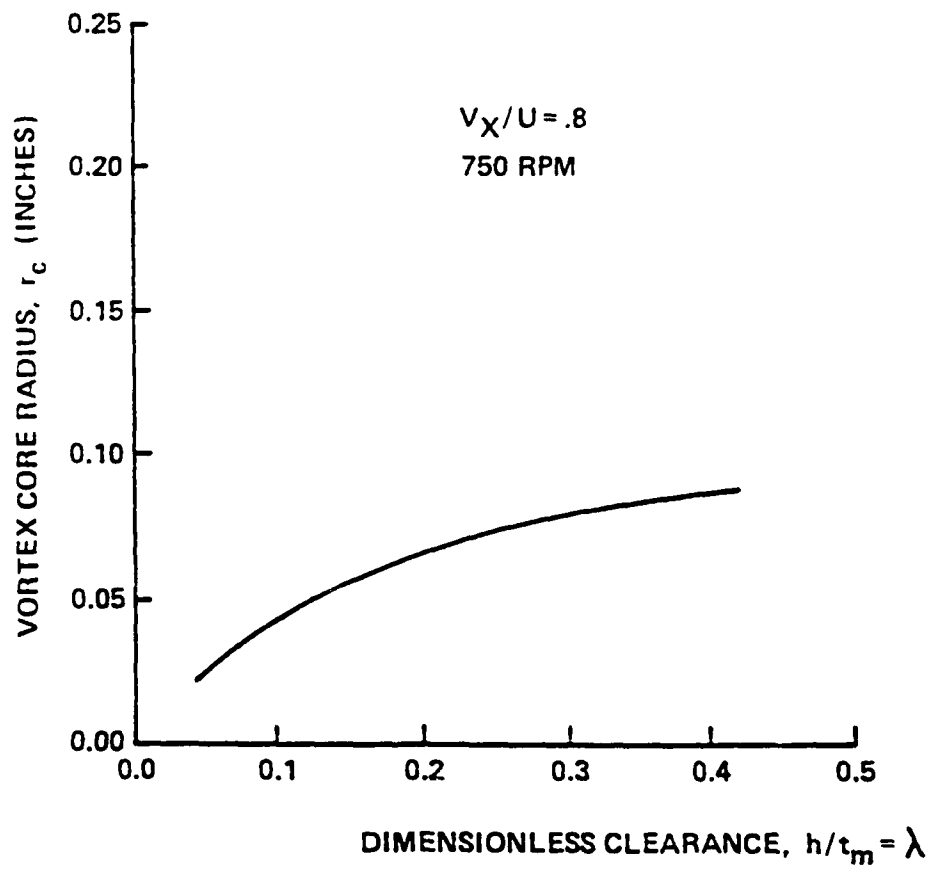


Figure 5.13. Sub-model Prediction of Vortex Core Radius versus Dimensionless Clearance for Mitchell's [43] Data

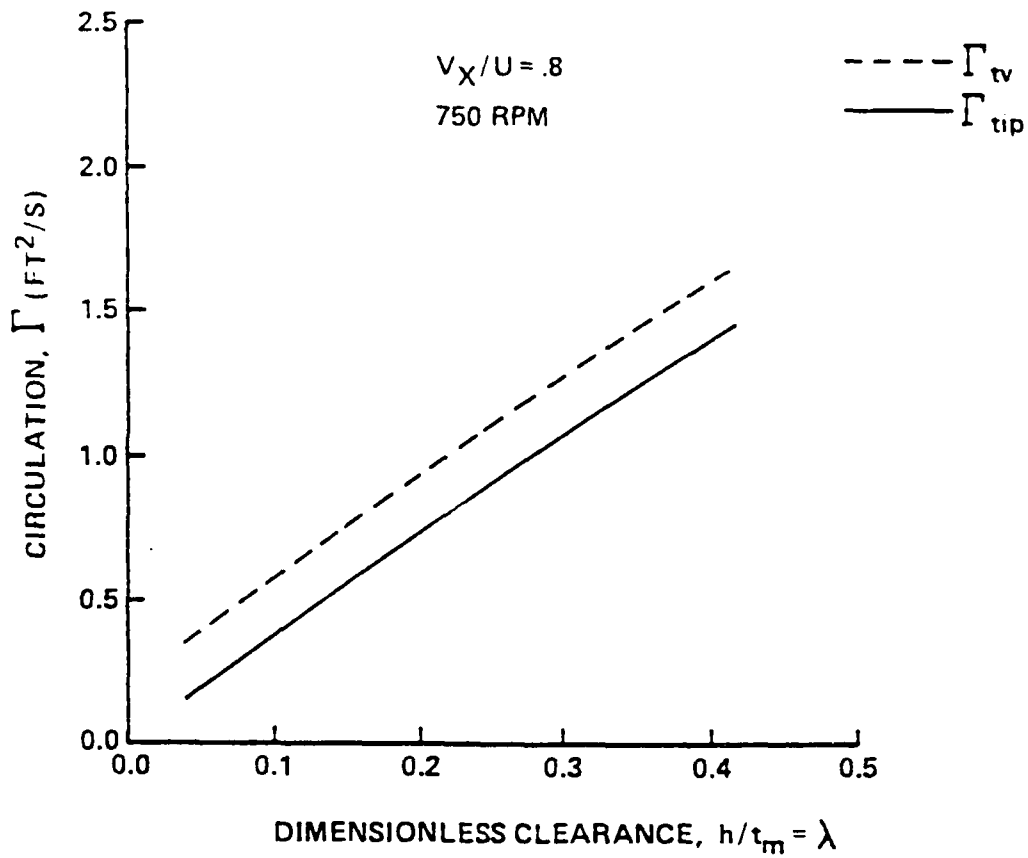


Figure 5.14. Sub-model Prediction of Shed Circulation versus Dimensionless Clearance for Mitchell's [43] Data

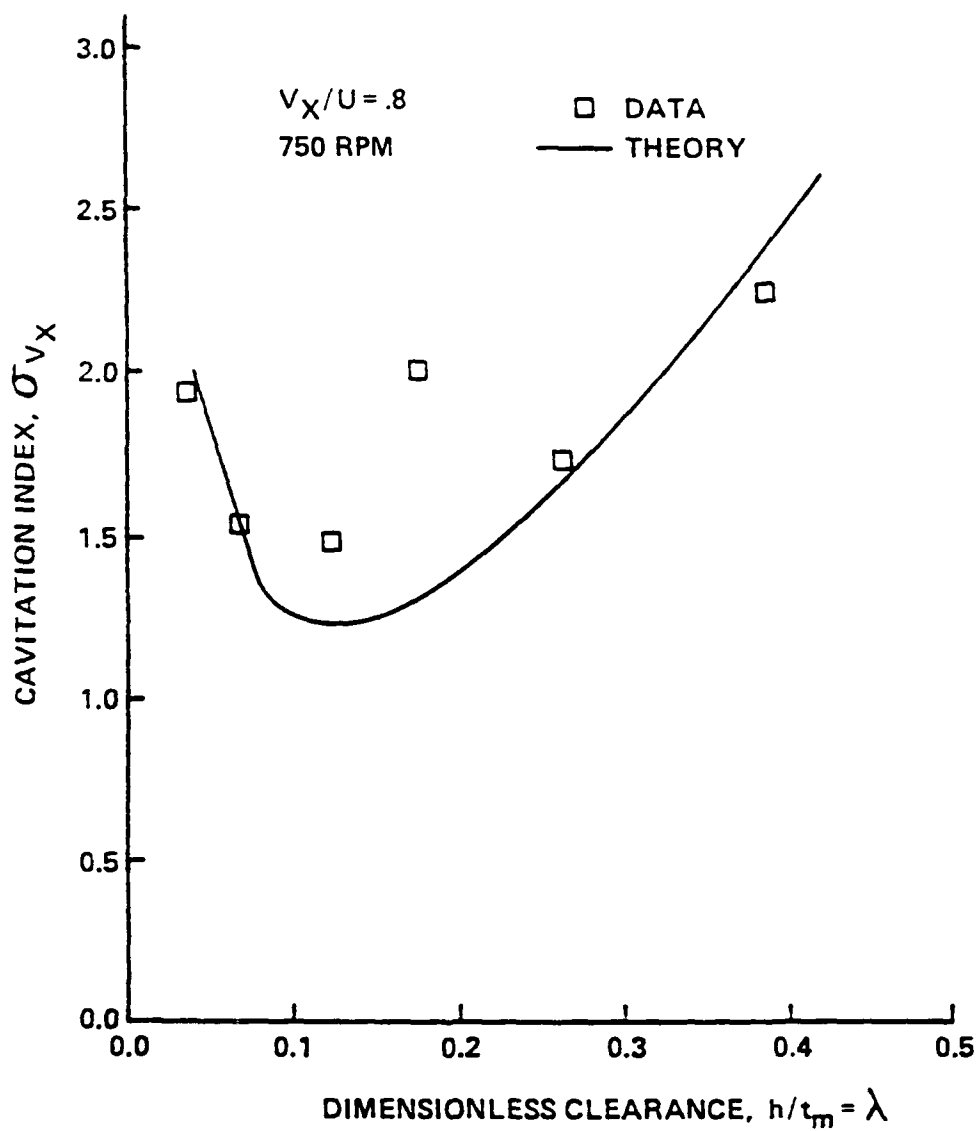


Figure 5.15. Theoretical and Measured Cavitation Indices for  $V_X/U = 0.8$ , 750 RPM, and  $Re_c = 9.2 \times 10^5$  for Mitchell's [43] Data

## Chapter 6

## CONCLUSIONS

6.1 Conclusions from the Experimental Program

The High Reynolds Number Pump Facility has provided opportunities for many unique measurements inside the turbomachinery flow field, some of which have never been before attempted. During this investigation, measurements of blade tip static pressure, velocity, dynamic tip clearance, blade forces, shaft torque, and tunnel pressure have been completed. The two-component LV system was used to measure the tip flow field. Several instrumentation developments and conclusions from the experimental program are noteworthy.

1. The low angular speed of the rotor necessitated the development of a viewing system which saved and stored successive images for easy viewing. The system performed excellently, and since cavitation tests were recorded, post-test analysis was facilitated.

2. A successful interfacing of the conditioned shaft encoder signal with the dynamic gap measuring system allowed tip clearance measurements during the operation of the pump. Results showed that the tip clearance did not change from its static values, which is reasonable considering the low angular speed of the rotor.

3. One-half inch diameter five-hole probes were used successfully in radial traverses at the inlet and exit of the pump stage. The extra support was needed since the probes were cantilevered over six inches.

4. The shear beam technique of measuring forces is particularly applicable to turbomachinery since minimal deflections are inherent,

and the compact design lends itself to convenient waterproofing. This method was used successfully to measure both blade and tip forces.

5. The ribbon cables often used in computer connections provide a compact method of connecting instrumentation. However, one must be aware of contamination noise, since the parallel conductors become antennae for stray signals as they rotate. The HIREP facility will continue to provide an invaluable tool for fluid dynamicists.

## 6.2 Conclusions from the Correlation Model

The application of the end-wall vortex cavitation inception model to the data of this investigation as well as other studies has verified its usefulness. The dependence of the tip lift upon the tip clearance has been measured experimentally and was seen to agree with the empirical relationship of Lewis and Yeung [35]. Laser velocimeter measurements were used together with visual observations of the cavitating tip flow field to develop a relation for the end-wall vortex core size as a function of the tip clearance.

The end-wall vortex was complicated by the interaction of other secondary flows at the suction side trailing edge. In particular, the flow visualization photographs revealed a separation zone on the suction side of the rotor blade which appeared to migrate to the tip. At small tip clearances, this secondary flow has a substantial influence on the end-wall vortex, both in size and strength. At small tip clearances, the end-wall vortex is formed near the leading edge of the blade tip. The two vortices originate far from each other and are not fully wrapped up at the laser velocimeter measurement stations,

0.5 and 2.75 inches downstream of the rotor trailing edge. At these measurement stations, the core appears much larger than the gap and the core sizes at larger clearances. However, the location of desinent cavitation of the vortex was at least a chord length downstream, where the vortex is more compact. Since the vortex core at a large tip clearance has minimal interference from the other vortex forming on the suction side, it was used as the maximum value, indicative of the unbounded blade condition.

The application of the correlation model to data from other investigations also indicated an additional source of circulation in the end-wall vortex other than the circulation shed from the blade tip. The physics of this additional circulation is not well understood at this time. Obviously, the application of the correlation model is limited because of this parameter of the model which is not well defined. A reasonable estimate can be made by observing the ratio  $\Gamma_{tv}/\Gamma_{sec}$  for the investigations discussed above.

### 6.3 Recommendations for Further Research

The vortex core radius should be measured for various flow coefficients to determine the influence of this parameter on the vortex size. The present measurements were taken only at the design operating point. Measurements of core size are difficult, even with the advantages of the laser velocimeter. The vortex appears to wander in the circumferential direction; research in this regard would be useful in determining the instantaneous core size. Also, it would be useful to measure the core size for rotor tips of various geometries.

The approach to the present investigation assumed that the circulation contained in the end-wall vortex was represented by circulation shed from the blade tip, and other sources of circulation in the end-wall vortex were negligible. However, upon examination of the LV surveys, the end-wall vortex contained substantially more circulation than that shed from the tip. The shed circulation was calculated based on the correlation of Lewis and Yeung [35] which was experimentally verified in the present investigation. The additional circulation  $\Gamma_{\text{sec}}$  was added in the present investigation based on the LV measurements. An integration of the gradient of the circulation over a correlating length may account for  $\Gamma_{\text{sec}}$ . The problem of quantifying the additional circulation in the end-wall vortex is obviously coupled with the core radius measurement problem. The tip-vortex and the secondary vortex interact near the trailing edge as illustrated in Figure 6.1. Since this source of circulation appears to be a principal contributor to the end-wall vortex, particularly at small clearances of normal turbomachinery operation, it is prudent that additional research be done to examine the nature of this phenomenon.

The sensitivity of the cavitation index to flow coefficient changes at small tip clearances is interesting and worthy of additional research. A matrix of static pressure transducers on the tip suction surface near the leading edge would provide insight on the manner in which the flow passes through the tip clearance near the leading edge. Perhaps a large suction peak is generated.



Figure 6.1. Cavitation of Interacting Vortices near the Tip Trailing  
Edge on the Suction Side

## REFERENCES

1. Shuba, B. H., "An Investigation of Tip-wall Vortex Cavitation in an Axial-flow Pump," Master's Thesis, The Pennsylvania State University, Dept. of Aerospace Engineering, 1983.
2. Gearhart, W. S., "Tip Clearance Cavitation in Shrouded Underwater Propulsors," AIAA J. Aircraft, Vol. 3, No. 2, March-April 1966.
3. Reeder, J. A., "Tip Clearance Problems in Axial Compressors (A Survey of Available Literature)," Union Carbide Corporation, January 4, 1969.
4. Peacock, R. E., "Blade Tip Gap Effects in Turbomachines, A Review," Naval Post-Graduate School Report NPS 67-81-016, 1981.
5. Wisler, D. C., "Aerodynamic Effects of Tip Clearance, Shrouds, Leakage Flow, Casing Treatment, and Trenching in Compressor Design," Tip Clearance Effects in Axial Turbomachines, Von Karman Institute and The Pennsylvania State University Lecture Course, Vol. I, April 1986.
6. AGARD Conference Proceedings No. 237, "Seal Technology in Gas Turbine Engines," April 1978.
7. Koch, C. C., "Stalling Pressure Rise Capability of Axial-flow Compressor Stages," ASME Paper No. 81-GT-3, March 1981.
8. Koch, C. C. and L. H. Smith, Jr., "Loss Sources and Magnitudes in Axial-flow Compressors," ASME Paper No. 75-WA/GT-6, December 1975.
9. Hunter, I. H. and N. A. Cumpsty, "Casing Wall Boundary Layer Development Through an Isolated Rotor," ASME Paper No. 82-GT-18, 1982.
10. Bailey, E. E. and C. H. Volt, "Some Observations of Effects of Porous Casings on Operating Range of a Single Axial-flow Compressor Rotor," NASA TM X-2120, October 1970.
11. Osborne, W. M., G. W. Lewis, Jr., and L. J. Heidelberg, "Effects of Several Porous Casing Treatments on Stall Limit and on Overall Performance of an Axial-flow Compressor Rotor," NASA TN D6537, November 1971.
12. Moore, R. D., G. Kovich, and R. J. Blade, "Effect of Casing Treatment on Overall and Blade-element Performance of a Compressor Rotor," NASA TN D-6538, November 1971.
13. Bailey, E. E., "Effects of Grooved Casing Treatment on the Flow Range Capability of a Single-state Axial-flow Compressor," NASA TN X-2459, January 1972.

14. Boyce, M. P., R. N. Schiller, and A. R. Desai, "Study of Casing Treatment Effects in Axial-flow Compressors, ASME Paper 74-GT-89, April 1974.
15. Prince, Jr., D. C., D. C. Wisler, and D. E. Hilvers, "Study of Casing Treatment Stall Margin Improvement Phenomena," ASME Paper 75-GT-160, 1975.
16. Fabri, J. and J. Reboux, "Effect of Outer Casing Treatment on Stall Margin of a Supersonic Rotating Cascade, ASME Paper 75-GT-95, 1975.
17. Takata, H. and Y. Tsakuda, "Study on the Mechanism of Stall Margin Improvement of casing Treatment," ASME Paper 75-GT-13, March 1975.
18. Robideau, B. A. and J. Nuler, "Blade Tip Seal for an Axial-flow Rotary Machine," U. S. Patent No. 4,328,170, December 9, 1980.
19. Roberts, F., "Blade Tip Shroud for a Compression Stage of a Gas Turbine Engine," U. S. Patent 4,239,452, December 16, 1980.
20. Booth, T. C., and P. R. Dodge, and H. K. Hepworth, "Rotor-tip Leakage Part I -- Basic Methodology," ASME Transactions 81-GT-71, 1981.
21. Wadia, A. R. and T. C. Booth, "Rotor-tip Leakage: Part II -- Design Optimization Through Viscous Analysis and Experiment," ASME Paper 81-GT-72, 1972.
22. Wadia, A. R., "Numerical Solution of Two- and Three-dimensional Rotor Tip Leakage Models," AIAA Journal, Vol. 23, No. 7, July 1985.
23. Owen, J. M., "Rotating Disks and Enclosures, XIV ICHMT Symposium on Heat Transfer in Rotating Machinery, D. E. Metzger and N. H. Afgan, Eds., Hemisphere Publishing Corporation and Springer Verlag, 1984.
24. Hennecke, D. K., "Active and Passive Tip Clearance Control," Von Karman Institute and The Pennsylvania State University Lecture Course, Tip Clearance Effects in Axial Turbomachines, Vol. II, 1986.
25. Hennecke, D. K., "Thermal Analysis of a High-Pressure Compressor Rotor of an Aero-engine-venting as a Means for Life Improvement," Warme-und. Stoffubertragung 18, 227-230, 1984.
26. Wu, C. H. and W. Wu, "Analysis of Tip Clearance Flow in Turbomachines," Polytechnic Institute of Brooklyn, Gas Turbine Laboratory, Dept. of Mechanical Engineering, July 1954.

27. Rains, D. A. "Tip Clearance Flows in Axial Flow Compressors and Pumps," Hydromechanics and Mechanical Engineering Laboratories, California Institute of Technology, 1954.
28. Vavra, M. H., Aero-thermodynamics and Flow in Turbomachines, John Wiley & Sons, New York, 1960.
29. Dean, R. C., "The Influence of Tip Clearance on Boundary Layer Flow in a Rectilinear Cascade," Gas Turbine Laboratory, Massachusetts Institute of Technology, December 1964.
30. Dean, R. C., "Secondary Flow in Axial Compressors," Sc. D. Thesis, Gas Turbine Laboratory, Massachusetts Institute of Technology, 1954.
31. Jefferson, B. A. and R. C. Turner, "Some Shrouding and Tip Clearance Effects in Axial Flow Compressors," International Ship Builder Progress, Vol. 5, No. 42, pp. 78-101, February 1958.
32. Lakshminarayana, B. and J. H. Horlock, "Tip Clearance Flow and Losses for an Isolated Compressor Blade," British A. R. C. Report and Memorandum 3316, 1962.
33. Lakshminarayana, B. and J. H. Horlock, "Leakage and Secondary Flows in Compressor Cascades," Dept. of Mechanical Engineering, The University of Liverpool, Reports and Memoranda No. 3483, March 1967.
34. Lakshminarayana, B., "Methods of Predicting the Tip Clearance Effects in Axial Flow Turbomachinery," ASME Transactions, J. Basic Engineering, September 1970.
35. Lewis, R. I. and E. H. C. Yeung, "Vortex Shedding Mechanisms in Relation to Tip Clearance Flows and Losses in Axial Fans," Newcastle University, London, Her Majesty's Stationery Office, May 1977.
36. Lakshminarayana, B., M. Pouagare, and R. Davino, "Three-dimensional Flow Field in the Tip Region of a Compressor Rotor Passage -- Part I: Mean Velocity Profiles and Annulus Wall Boundary Layer," ASME Paper 82-GT-234, 1982.
37. Lakshminarayana, B., M. Pouagare, and R. Davino, "Three-dimensional Flow Field in the Tip Region of a Compressor Rotor Passage -- Part II: Turbulence Properties," ASME Paper 82-GT-234, 1982.
38. Pandya, A. and B. Lakshminarayana, "Investigation of the Tip Clearance Flow Inside and at the Exit of a Compressor Rotor Passage -- Part I: Mean Velocity Field, J. of Engineering for Power, Vol. 105, January 1983.

39. Pandya, A. and B. Lakshminarayana, "Investigation of the Tip Clearance Flow Inside and at the Exit of a Compressor Rotor Passage -- Part II: Turbulence Properties," J. of Engineering for Power, Vol. 105, January 1983.
40. Lakshminarayana, B., N. Siteram, and J. Zhang, "End-wall and Profile Losses in a Low-speed Axial Flow Compressor Rotor," ASME 85-GT-174, March, 1985.
41. Inoue, M., M. Kuromaru, and M. Fukuhara, "Behavior of Tip Leakage Flow Behind an Axial Compressor Flow," ASME Paper 85-GT-62, 1985.
42. Lakshminarayana, B. and K. N. S. Murthy, "Laser Doppler Velocimeter Measurement of Annulus Wall Boundary Layer Development in a Compressor Rotor," ASME J. of Turbomachinery, Vol. 110, pp. 377-385.
43. Mitchell, A. B., "An Experimental Investigation of Cavitation Inception in the Rotor Blade Tip Region of an Axial Flow Pump," Admiralty Research Laboratory, ARL/R1/G/HY/11/2, August 1958.
44. Shalnev, K. K., "Cavitation in Turbomachines," Water Power, January 1958.
45. McCormick, B. W. "On Cavitation Produced by a Vortex Trailing from a Lifting Surface," ASME Transactions, J. Basic Engineering, September 1962.
46. Gearhart, W. S., and J. R. Ross, "Tip Leakage Effects," Applied Research Laboratory, TM 83-20, 28 February 1983.
47. Billet, M. L., and J. W. Holl, "Scale Effects on Various Types of Cavitation," J. Fluids Engineering, September 1981.
48. Okamoto, H., K. Okata, Y. Saito, T. Takahei, "Cavitation Study of Ducted Propellers on Large Ships," The Society of Naval Architects and Marine Engineers, 1975.
49. Narita, H., Y. Kunitake, H. Yagi, M. Oosterveld, and M. Hoekstra, "Model and Full Scale Ducted Propeller Cavitation Observations on a 280,000 dwt. Tanker," Journal of Society of Naval Architects of Japan, Vol. 136, December 1974.
50. McBride, M. W., "Engineering Design Methods for Axial and Mixed Flow Hydraulic Machinery," ASME Small Hydro Power Machinery 1982, pp. 73-80.
51. Lehman, A. F., "The Garfield Thomas Water Tunnel," Ordnance Research Laboratory Report No. NOrd16597-56, September 30, 1959.

52. Farrell, K. J., M. W. McBride, and M. L. Billet, "High Reynolds Number Pump Facility for Cavitation Research," ASME International Symposium on Cavitation Research Facilities and Techniques -- 1987, pp. 61-68.
53. Holl, J. W., "An Effect of Air Content on the Occurrence of Cavitation," J. Basic Engineering, December, 1960, pp. 941-946.
54. Giesing, J. P., "Extension of the Douglas Neumann Program to Problems of Lifting, Infinite Cascades," U.S. Department of Commerce, Report No. LB31653, AD605207, revised July 2, 1964.
55. Baker, G. R., S. J. Barker, K. K. Bofah, and P. G. Saffman, "Laser Anemometer Measurements of Trailing Vortices in Water," J. Fluid Mechanics (1974), Vol. 65, Part 2, pp. 325-336.
56. Howell, A. R., "The Present Basis of Axial Flow Compressor Design: Part I - Cascade Theory and Performance," Aeronautical Research Council, R and M 2093, 1942.

Blade Number	2	5	6	2	5
$\lambda$	0.089	0.078	0.086	0.089	0.078
Flow Coefficient	1.38	1.38	1.38	1.38	1.38
$V_{ref}$ (ft/s)	26.	26.	26.	31.	31.
RPM	187.	186.	186.	225.	225.
Temperature (F)	86.1	86.2	86.2	86.3	86.4
$\sigma$	1.08	1.26	1.12	1.16	1.28
$-C_{Pmin}$	0.99	1.17	1.03	1.10	1.22
Air Content(ppm)	5.9	5.9	5.9	5.9	5.9
Blade Number	6	2	5	6	2
$\lambda$	0.086	0.089	0.078	0.086	0.176
Flow Coefficient	1.38	1.38	1.38	1.38	1.38
$V_{ref}$ (ft.sec.)	31.	36.	36.	36.	26.
RPM	225.	264.	263.	264.	187.
Temperature (F)	86.4	86.6	86.7	86.8	81.4
$\sigma$	1.10	1.20	1.32	1.21	1.54
$-C_{Pmin}$	1.04	1.15	1.27	1.16	1.50
Air Content(ppm)	5.9	5.9	5.9	5.9	2.9
Blade Number	5	6	2	5	6
$\lambda$	0.164	0.177	0.176	0.164	0.177
Flow Coefficient	1.39	1.39	1.39	1.39	1.39
$V_{ref}$ (ft/s)	26.	26.	31.	31.	31.
RPM	187.	186.	224.	223.	222.
Temperature (F)	81.4	81.5	81.6	81.6	81.7
$\sigma$	1.40	1.30	1.34	1.47	1.35
$-C_{Pmin}$	1.35	1.26	1.31	1.44	1.32
Air Content(ppm)	2.9	2.9	2.9	2.9	2.9
Blade Number	2	5	6	2	5
$\lambda$	0.176	0.164	0.177	0.352	0.343
Flow Coefficient	1.38	1.38	1.38	1.38	1.38
$V_{ref}$ (ft/s)	36.	36.	36.	26.	26.
RPM	261.	260.	260.	188.	187.
Temperature (F)	81.9	82.	82.1	84.6	84.61
$\sigma$	1.50	1.63	1.42	1.52	1.90
$-C_{Pmin}$	1.48	1.61	1.40	1.39	1.77
Air Content(ppm)	2.9	2.9	2.9	8.7	8.7
Blade Number	6	2	5	6	2
$\lambda$	0.348	0.352	0.343	0.348	0.352
Flow Coefficient	1.38	1.38	1.38	1.38	1.38
$V_{ref}$ (ft/s)	26.	31.	31.	31.	36.
RPM	188.	224.	223.	224.	262.
Temperature (F)	84.7	84.8	84.9	84.9	85.3
$\sigma$	1.62	1.57	1.83	1.54	1.47
$-C_{Pmin}$	1.49	1.48	1.73	1.45	1.40
Air Content(ppm)	8.7	8.7	8.7	8.7	8.7

Blade Number	5	6	2	5	6
$\lambda$	0.343	0.348	0.552	0.560	0.546
Flow Coefficient	1.38	1.38	1.37	1.37	1.37
$V_{ref}$ (ft/s)	36.	36.	26.	26.	26.
RPM	263.	263.	189.	188.	187.
Temperature (F)	85.4	85.5	82.5	82.5	82.6
$\sigma$	1.86	1.63	1.78	1.45	1.40
$-C_{pmin}$	1.79	1.56	1.69	1.35	1.31
Air Content(ppm)	8.7	8.7	6.3	6.3	6.3
Blade Number	2	5	6	2	5
$\lambda$	0.552	0.560	0.546	0.552	0.569
Flow Coefficient	1.37	1.37	1.37	1.37	1.37
$V_{ref}$ (ft/s)	31.	31.	31.	36.	36.
RPM	226.	226.	226.	263.	263.
Temperature (F)	82.6	82.7	82.8	82.9	83.0
$\sigma$	1.64	1.34	1.30	1.70	1.34
$-C_{pmin}$	1.57	1.27	1.23	1.65	1.29
Air Content(ppm)	6.3	6.3	6.3	6.3	6.3
Blade Number	6	2	5	6	2
$\lambda$	0.546	0.089	0.078	0.086	0.089
Flow Coefficient	1.37	1.33	1.33	1.33	1.33
$V_{ref}$ (ft/s)	36.	26.	26.	26.	31.
RPM	263.	196.	196.	196.	236.
Temperature (F)	83.1	84.4	84.4	84.5	84.7
$\sigma$	1.48	1.32	1.50	1.44	1.43
$-C_{pmin}$	1.43	1.24	1.42	1.36	1.37
Air Content(ppm)	6.3	5.9	5.9	5.9	5.9
Blade Number	5	6	2	5	6
$\lambda$	0.078	0.086	0.089	0.078	0.086
Flow Coefficient	1.33	1.33	1.33	1.33	1.33
$V_{ref}$ (ft/s)	31.	31.	36.	36.	36.
RPM	236.	237.	275.	275.	276.
Temperature (F)	84.8	84.8	85.0	85.3	85.5
$\sigma$	1.56	1.50	1.46	1.68	1.67
$-C_{pmin}$	1.50	1.44	1.42	1.64	1.63
Air Content(ppm)	5.9	5.9	5.9	5.9	5.9
Blade Number	2	5	6	2	5
$\lambda$	0.176	0.164	0.177	0.176	0.164
Flow Coefficient	1.35	1.35	1.35	1.35	1.35
$V_{ref}$ (ft/s)	26.	26.	26.	31.	31.
RPM	194.	195.	194.	230.	230.
Temperature (F)	78.2	78.2	78.4	78.4	78.5
$\sigma$	1.20	1.35	1.31	1.34	1.49
$-C_{pmin}$	1.16	1.31	1.27	1.31	1.46
Air Content(ppm)	2.9	2.9	2.9	2.9	2.9

Blade Number	6	2	5	6	2
$\lambda$	0.177	0.176	0.164	0.177	0.352
Flow Coefficient	1.35	1.35	1.35	1.35	1.33
$V_{ref}$ (ft/s)	31.	36.	36.	36.	26.
RPM	229.	272.	273.	272.	196.
Temperature (F)	78.6	78.8	78.9	79.1	83.0
$\sigma$	1.40	1.48	1.54	1.51	1.60
$-C_{pmin}$	1.37	1.46	1.52	1.49	1.48
Air Content(ppm)	2.9	2.9	2.9	2.9	8.7

Blade Number	5	6	2	5	6
$\lambda$	0.343	0.348	0.352	0.343	0.348
Flow Coefficient	1.33	1.33	1.33	1.33	1.33
$V_{ref}$ (ft/s)	26.	26.	31.	31.	31.
RPM	195.	195.	235.	234.	235.
Temperature (F)	83.0	83.1	83.5	83.6	83.7
$\sigma$	1.94	1.61	1.45	1.94	1.72
$-C_{pmin}$	1.82	1.49	1.37	1.85	1.64
Air Content(ppm)	8.7	8.7	8.7	8.7	8.7

Blade Number	2	5	6	2	5
$\lambda$	0.352	0.343	0.348	0.552	0.560
Flow Coefficient	1.33	1.33	1.33	1.33	1.33
$V_{ref}$ (ft/s)	36.	36.	36.	26.	26.
RPM	273.	272.	273.	196.	197.
Temperature (F)	84.2	84.3	84.4	81.2	81.2
$\sigma$	1.59	1.86	1.86	1.70	1.38
$-C_{pmin}$	1.53	1.80	1.80	1.61	1.29
Air Content(ppm)	8.7	8.7	8.7	6.3	6.3

Blade Number	6	2	5	6	2
$\lambda$	0.546	0.552	0.560	0.546	0.552
Flow Coefficient	1.33	1.33	1.33	1.33	1.33
$V_{ref}$ (ft/s)	26.	31.	31.	31.	36.
RPM	196.	237.	236.	237.	276.
Temperature (F)	81.2	81.4	81.5	81.5	81.7
$\sigma$	1.60	1.65	1.40	1.43	1.68
$-C_{pmin}$	1.51	1.59	1.34	1.37	1.62
Air Content(ppm)	6.3	6.3	6.3	5.3	5.3

Blade Number	5	6	2	5	6
$\lambda$	0.556	0.546	0.089	0.078	0.086
Flow Coefficient	1.33	1.33	1.28	1.28	1.28
$V_{ref}$ (ft/s)	36.	36.	26.	26.	26.
RPM	275.	275.	204.	204.	205.
Temperature (F)	81.8	81.9	82.4	82.5	82.5
$\sigma$	1.38	1.58	1.70	2.42	1.94
$-C_{pmin}$	1.34	1.54	1.62	2.34	1.87
Air Content(ppm)	6.3	6.3	5.9	5.9	5.9

Blade Number	2	5	6	2	5
$\lambda$	0.089	0.078	0.086	0.089	0.078
Flow Coefficient	1.28	1.28	1.28	1.28	1.28
$V_{ref}(ft/s)$	31.	31.	31.	36.	36.
RPM	244.	245.	245.	289.	286.
Temperature (F)	82.8	82.7	82.7	83.5	84.2
$\sigma$	1.80	2.26	2.02	1.85	2.23
$-C_{pmin}$	1.75	2.21	1.97	1.81	2.19
Air Content(ppm)	5.9	5.9	5.9	5.9	5.9
Blade Number	6	2	5	6	2
$\lambda$	0.086	0.175	0.164	0.177	0.175
Flow Coefficient	1.28	1.28	1.28	1.28	1.28
$V_{ref}(ft/s)$	36.	26.	26.	26.	31.
RPM	286.	202.	202.	202.	245.
Temperature (F)	84.3	79.3	79.4	79.4	79.6
$\sigma$	2.22	1.50	1.48	1.64	1.49
$-C_{pmin}$	2.18	1.46	1.44	1.60	1.46
Air Content(ppm)	5.9	2.9	2.9	2.9	2.9
Blade Number	5	6	2	5	6
$\lambda$	0.164	0.177	0.175	0.164	0.177
Flow Coefficient	1.28	1.28	1.28	1.28	1.28
$V_{ref}(ft/s)$	31.	31.	36.	36.	36.
RPM	246.	245.	287.	287.	287.
Temperature (F)	79.7	79.8	80.3	80.5	80.6
$\sigma$	1.54	1.62	1.58	1.78	1.67
$-C_{pmin}$	1.51	1.59	1.56	1.76	1.65
Air Content(ppm)	2.9	2.9	2.9	2.9	2.9
Blade Number	2	5	6	2	5
$\lambda$	0.352	0.343	0.348	0.352	0.343
Flow Coefficient	1.28	1.28	1.28	1.28	1.28
$V_{ref}(ft/s)$	26.	26.	26.	31.	31.
RPM	203.	206.	206.	244.	245.
Temperature (F)	83.4	83.4	83.6	83.7	83.8
$\sigma$	1.87	2.03	1.90	1.77	1.99
$-C_{pmin}$	1.75	1.92	1.79	1.69	1.91
Air Content(ppm)	8.7	8.7	8.7	8.7	8.7
Blade Number	6	2	5	6	2
$\lambda$	0.348	0.352	0.343	0.348	0.552
Flow Coefficient	1.28	1.28	1.28	1.28	1.26
$V_{ref}(ft/s)$	31.	36.	36.	36.	26.
RPM	243.	289.	289.	289.	207.
Temperature (F)	84.0	82.2	82.3	87.6	80.1
$\sigma$	2.03	1.64	1.90	2.07	1.74
$-C_{pmin}$	1.95	1.58	1.84	2.01	1.66
Air Content(ppm)	8.7	8.7	8.7	8.7	6.3

Blade Number	5	6	2	5	6
$\lambda$	0.560	0.546	0.552	0.560	0.546
Flow Coefficient	1.26	1.26	1.26	1.26	1.26
$V_{ref}(ft/s)$	26.	26.	31.	31.	31.
RPM	206.	207.	247.	247.	246.
Temperature (F)	80.1	80.2	80.3	80.4	80.5
$\sigma$	1.64	1.78	1.97	1.59	1.74
$-C_{pmin}$	1.56	1.70	1.92	1.54	1.69
Air Content(ppm)	6.3	6.3	6.3	6.3	6.3

Blade Number	2	5	6
$\lambda$	0.552	0.560	0.546
Flow Coefficient	1.26	1.26	1.26
$V_{ref}(ft/s)$	36.	36.	36.
RPM	292.	290.	292.
Temperature (F)	80.7	80.9	81.0
$\sigma$	1.76	1.61	1.76
$-C_{pmin}$	1.72	1.57	1.72
Air Content(ppm)	6.3	6.3	6.3